LA-UR-24-29668

Approved for public release; distribution is unlimited.

Title:	Uranium Mononitride (UN) Handbook
Author(s):	Miller, Zachary Aaron; Levinsky, Alex; Craven, Galen Thomas; Mehta, Vedant Kiritkumar; Fratoni, Massimiliano; White, Joshua Taylor; Andersson, Anders David Ragnar; Kosmidou, Maria; Terricabras, Adrien Jose Emile
Intended for:	Report
Issued:	2024-09-09

Uranium Mononitride (UN) Handbook

Z. Miller[1,4], A. Levinsky[1], G. T. Craven[2], V. Mehta[1], M. Fratoni[4], J. White[3], D. Andersson[3], M. Kosmidou[3], A. Terricabras[3]

[1]*Nuclear Engineering & Non-Proliferation Division, Los Alamos National Laboratory, USA*

P.O. Box 1663, Los Alamos, NM 87545

[2]*Theoretical Division, Los Alamos National Laboratory, USA*

P.O. Box 1663, Los Alamos, NM 87545

[3]*Material Science and Technology Division, Los Alamos National Laboratory, USA*

P.O. Box 1663, Los Alamos, NM 87545

[4]*Department of Nuclear Engineering, University of California, Berkeley, USA*

SUMMARY

Uranium Mononitride (UN) is being reexamined as a high temperature advanced nuclear fuel in many reactor applications due to its high thermal conductivity, high melting point, and high fissionable uranium density, among other desirable properties [1, 2]. A thorough review of the experimental data for the material and irradiation properties has been collected and is presented in this handbook. As an outcome of this review, in many cases, it is apparent that additional experimental verification must be conducted to verify the available data and to verify the suggested empirical correlations.

Experimental data for Young's modulus (E), Poisson's ratio (v), shear modulus (G), bulk modulus (K), coefficient of thermal expansion (α), thermal conductivity (k), and self diffusion of Nitrogen and Uranium have been collected and the following empirical correlations were developed as a result of this work. T is temperature in K, D is percent of theoretical density, P is fractional percent porosity:

$$\boldsymbol{E}\ [\mathrm{GPa}] = 2.479x10^{-4}\ (D)^{3.013}[1.0728 - 2.4269 \times 10^{-4}T]$$

$$\boldsymbol{v} = 7.575x10^{-4}(D)^{1.286}[0.9949 + 5.3524 \times 10^{-6}T + 3.9272 \times 10^{-8}T^2]$$

$$\boldsymbol{G}\ [\mathrm{GPa}] = 2.173 \times 10^{-5}(D)^{3.353}[1.0702 - 2.3401 \times 10^{-4}T]$$

$$\boldsymbol{K}\ [\mathrm{GPa}] = 4.425 \times 10^{-8}(D)^{4.841}[1.0536 - 1.7869 \times 10^{-4}T]$$

$$\boldsymbol{\alpha}\ \left[\frac{1}{\mathrm{K}}\right] = 2.089x10^{-6}(T)^{0.209}$$

$$\boldsymbol{k}\ \left[\frac{\mathrm{W}}{\mathrm{m\ K}}\right] = 2.123\exp(-2.14P)\ (T)^{0.338}$$

$$\boldsymbol{D_N}\ \left[\frac{\mathrm{m^2}}{\mathrm{s}}\right] = 1.255 \times 10^{-65}\ (T)^{15.294}$$

$$\boldsymbol{D_U}\ \left[\frac{\mathrm{m^2}}{\mathrm{s}}\right] = 1.604 \times 10^{-106}\ (T)^{26.264}$$

The following empirical correlations for creep rate ($\dot{\varepsilon}$), porosity factor ($f(p)$), and specific heat capacity (C_p) are well established in literature and are presented below. T is temperature in K and P is fractional percent porosity:

$$\dot{\boldsymbol{\varepsilon}}\left[\frac{1}{\mathrm{s}}\right] = 2.054 \times 10^{-3}\sigma^{4.5}\exp\left(-\frac{39369.5}{T}\right)$$

$$\boldsymbol{f}(\mathrm{p}) = \frac{0.987}{(1-P)^{27.6}}\exp(-8.65P)$$

$$\boldsymbol{C_p}\left[\frac{\mathrm{J}}{\mathrm{mol\ K}}\right] = 51.14\left(\frac{365.7}{T}\right)^2\frac{\exp\left(\frac{365.7}{T}\right)}{[\exp\left(\frac{365.7}{T}\right)-1]^2} + 9.941 \times 10^{-3}(T)$$

CONTENTS

SUMMARY 2
CONTENTS 3
FIGURES 4
TABLES 6
ACRONYMS 8
1. INTRODUCTION 10
2. UNIRRADIATED FUEL PROPERTIES 11
2.1. MECHANICAL PROPERTIES 11
2.1.1. YOUNG'S MODULUS 16
2.1.2. POISSON'S RATIO 17
2.1.3. SHEAR MODULUS 19
2.1.4. BULK MODULUS 21
2.1.5. CREEP 23
2.1.6. COEFFICIENT OF THERMAL EXPANSION 25
2.1.7. URANIUM AND NITROGEN SELF-DIFFUSIVITY 27
2.2. THERMAL PROPERTIES 31
2.2.1. THERMAL CONDUCTIVITY 31
2.2.2. SPECIFIC HEAT CAPACITY 38
3. EXAMINING FUEL UNDER IRRADIATION 40
3.1. FISSION PRODUCTS 41
3.2. FUEL SWELLING 43
3.3. SUMMARY OF UN IRRADIATION PROGRAMS 47
3.3.1. BR-10 47
3.3.2. SNAP-50 55
3.3.3. ADVANCED SPACE POWER NUCLEAR REACTOR CONCEPT (NASA) 70
3.3.4. SP-100 83
3.3.5. BATTELLE RESEARCH REACTOR 88
3.3.6. LAWRENCE RADIATION LABORATORY 100
4. ACKNOWLEDGEMENTS 107
REFERENCES 108

FIGURES

Figure 1.1: NaCl crystal structure of Uranium Mononitride.
Figure 1.2: Fluoride crystal structure of Uranium Dioxide.
Figure 2.1: General stress-strain curve for an elastic-plastic material during tensile test.
Figure 2.2: Idealized stress-strain curves for different material classes.
Figure 2.3: Computational data for Elastic Properties of UN versus temperature [22]. Young's modulus (E), shear modulus (G), bulk modulus (K), and Poisson's ratio (v). Temperature dependent correlations shown in dashed lines.
Figure 2.4: Experimental data for Young's modulus of UN versus porosity at room temperature [10-18]. ± 2σ is shown in plot with experimental data within ≤ 28% of trendline.
Figure 2.5: Experimental data for Poisson's ratio for UN versus porosity at room temperature [11, 12, 16-18]. ± 2σ is shown in plot with experimental data within ≤ 21% of trendline.
Figure 2.6: Experimental data for shear modulus of UN versus porosity [11, 12, 15-18]. ± 2σ is shown with experimental data within ≤ 15% of trendline.
Figure 2.7: Experimental data for bulk modulus of UN versus porosity at room temperature [11, 12, 16, 17]. ± 2σ is shown in plot with experimental data within ≤ 27% of trendline.
Figure 2.8: Typical creep curve of strain versus time at constant stress.
Figure 2.9: Experimental data for thermal expansion versus temperature [15, 16, 19, 21]. ± 2σ is shown in plot with experimental data within ≤ 13% of trendline.
Figure 2.10. Experimental data for nitrogen self-diffusion versus temperature [19, 28, 29]. ± 2σ is shown in plot with experimental data within ≤ 32% of trendline.
Figure 2.11. Experimental data for nitrogen self-diffusion versus temperature [34]. ± 2σ is shown in plot with experimental data within ≤ 65% of trendline.
Figure 2.12: Comparison of thermal conductivity for UN and UO2 [40].
Figure 2.13: Experimental data for thermal conductivity of UN versus temperature for various porosities [41].
Figure 2.14: Experimental data for thermal conductivity versus temperature for UN at experimental porosities [14, 15, 22, 36, 37, 41-46].
Figure 2.15: Experimental data for thermal conductivity versus temperature for UN corrected to 100% TD [14, 15, 22, 36, 37, 41-46]. ± 2σ is shown in plot with experimental data within ≤ 39 % of trendline.
Figure 2.16: Experimental data for heat capacity versus porosity [15, 22, 37, 42, 49-54]. ± 2σ is shown in plot with experimental data within ≤ 14% of trendline.
Figure 3.1: Comparison of UN fission gas release experimental data versus burnup for individual fuel pellets [19, 56-64].
Figure 3.2: Comparison of total UN volumetric fuel swelling experimental data versus burnup for individual pellets [19, 56-64, 69-74].
Figure 3.3: Comparison of total UN volumetric fuel swelling experimental data versus burnup with respect to temperature and power density for individual pellets [19, 56-64, 69-74].
Figure 3.4: Volumetric swelling versus burnup for driver and experimental fuel assemblies [58, 59].
Figure 3.5: Swelling rate per 1 %FIMA burnup for various UN fuel temperatures [59].
Figure 3.6: Fission gas release as a percentage of total gas plenum volume versus burnup [58, 59].

Figure 3.7: Volumetric fuel swelling versus burnup for SNAP-50 testing performed at CANEL [19, 63].
Figure 3.8: Diameter increase versus burnup for SNAP-50 testing performed at CANEL [19, 63].
Figure 3.9: Fission gas release versus burnup for SNAP-50 testing performed at CANEL [19, 63].
Figure 3.10: Diametral fuel swelling versus burnup for SNAP-50 testing performed at ORNL [64].
Figure 3.11: Volumetric fuel swelling versus burnup for SNAP-50 performed at ORNL [64].
Figure 3.12: Fission gas release versus burnup for SNAP-50 performed at ORNL [64].
Figure 3.13: Fission gas release versus fuel swelling for CANEL and ORNL [64].
Figure 3.14: Volumetric fuel swelling versus burnup for NASA testing performed at PBRF [56, 60, 61, 72].
Figure 3.15: Fission gas release versus burnup for NASA testing performed at PBRF [56, 60, 61].
Figure 3.16. Comparison of the volumetric fuel swelling versus burnup for HT-BRR-3 and 4 [71].
Figure 3.17. Comparison of the volumetric fuel swelling versus burnup for HT-BRR-4 and 6 [71].
Figure 3.18. Volumetric swelling versus for test samples of the HT-BRR-10 test series [69].
Figure 3.19. UN volumetric swelling versus burnup for all Battelle testing series [69-71].
Figure 3.20. Volumetric swelling versus burnup for LRL-1 test specimens [73, 74].
Figure 3.21. Volumetric swelling versus burnup for LRL-2 test specimens. Letters in the legend correspond to irradiation sample identification [70].

TABLES

Table I: Fabrication data for UN fuel pellets used in thermal conductivity comparison.
Table II: Material composition for UN fuel pellets used in thermal conductivity analysis.
Table III. BR-10 reactor and fuel pin characteristics [74].
Table IV: Conditions of Irradiation of SA with UN [58, 59, 74].
Table V. BR-10 fuel pin chemical composition and specifications [59].
Table VI. BR-10 fuel swelling data for individual fuel pellets (Burnup [%FIMA], Fuel Swelling [%]) [58, 59].
Table VII. BR-10 fission gas data for individual fuel pellets (Burnup [%FIMA] Fission Gas Release [%]) [58, 59].
Table VIII. SNAP-50 Reference Design Parameters [64].
Table IX. Capsule and UN fuel data for high power density irradiation tests conducted at CANEL [19, 63].
Table X. Capsule and UN fuel data for low power density irradiation tests conducted at CANEL [19, 63].
Table XI. UN irradiation data for high power density irradiation tests conducted at CANEL [19, 63].
Table XII. UN irradiation data for low power density irradiation tests conducted at CANEL [19, 63].
Table XIII. Capsule and UN fuel data for irradiation tests conducted at ORNL [64].
Table XIV. UN irradiation data for irradiation tests conducted at ORNL [64].
Table XV. Capsule and UN fuel data for irradiation tests conducted at Plum Brook [85].
Table XVI. UN irradiation data for irradiation tests conducted at Plum Brook [85].
Table XVII. Capsule and UN fuel data for irradiation tests conducted at Plum Brook [61].
Table XVIII. UN irradiation data for irradiation tests conducted at Plum Brook [61].
Table XIX. Capsule and UN fuel data for irradiation tests conducted at Plum Brook [60].
Table XX. UN irradiation data for irradiation tests conducted at Plum Brook [60].
Table XXI. Capsule and UN fuel data for irradiation tests conducted at ORNL [56, 62].
Table XXII. UN irradiation data for irradiation tests conducted at ORNL [56, 62].
Table XXIII. Capsule and UN fuel data for irradiation tests conducted at Plum Brook [72].
Table XXIV. UN irradiation data for irradiation tests conducted at Plum Brook [72].
Table XXV. SP-100 testing breakdown [91].
Table XXVI. Comparison of key testing and fuel pin parameters [57].
Table XXVII. Capsule and UN fuel data for irradiation tests conducted for the SP-1 testing program [57].
Table XXVIII. UN irradiation data for irradiation tests conducted SP-1 testing program [57].
Table XXIX. HT-BRR-10 fuel specimen characteristics [69].
Table XXX. Capsule and UN fuel data for irradiation tests conducted during the Battelle testing program [69-71].
Table XXXI. UN irradiation data for high temperature irradiation tests conducted for the Battelle testing program [69-71].
Table XXXII. Microstructure for LRL-1 capsule specimens [92, 93].
Table XXXIII. Microstructure for LRL-2 capsule specimens [70].

Table XXXIV. Capsule and UN fuel data for irradiation tests conducted during the LRL testing program [70].
Table XXXV. UN irradiation data for high temperature irradiation tests conducted for the LRL testing program [70].

ACRONYMS

AEC	Atomic Energy Commission
AIMD	Ab Initio Molecular Dynamics
AF	Air Force
AFM	Antiferromagnetic
APR	Advanced Power Reactor
ANL	Argonne National Laboratory
ANP	Aircraft Nuclear Propulsion
BMI	Battelle Memorial Institute
BRR	Battelle Research Reactor
BR-10	Bystry Reactor-10
BU	Burnup
CANEL	Connecticut Advanced Nuclear Engine Lab
CTE	Coefficient of Thermal Expansion
DFMT	Dynamical Mean-Field Theory
DOE	Department of Energy
DOD	Department of Defense
FCC	Face-Centered Cubic
FCMI	Fuel-Cladding Mechanical Interaction
FIMA	Fissions per Initial Metal Atom
FFTF	Fast Flux Test Facility
FM	Ferromagnetic
IPPE	Institute for Physics and Power Engineering
LANL	Los Alamos National Laboratory
LDA	Local Density Approximation
LRL	Lawrence Radiation Laboratory
MD	Molecular Dynamics
MTR	Materials Testing Reactor
NaCl	Sodium Chloride
NASA	National Aeronautics and Space Administration
PBRF	Plum Brook Research Facility
PIE	Pos Irradiation Examination
Pa	Pascal
ORNL	Oak Ridge National Laboratory
SA	Subassembly
SNAP-50	Systems for Nuclear Auxiliary Power 50
TD	Theoretical Density
UC	Uranium Carbide
UO_2	Uranium Dioxide
UN_2	Uranium Dinitride

UN	Uranium Mononitride
U_2N_3	Uranium Sesquinnitride
Vol	Volume

1. Introduction

Uranium Nitride (UN) is a ceramic nuclear fuel comprised of a combination of the following family of ceramic materials: Uranium Mononitride (UN), Uranium Sesquinnitride (U_2N_3) and Uranium Dinitride (UN_2). During the fabrication process of UN, all three ceramic materials will be present with the majority being uranium mononitride. UN crystallizes in a lattice of NaCl type, which is a face-centered cubic (*fcc*) (Figure 1.1) crystal [3-5]. If the lattice constant and theoretical mass of the crystal structure is known, the theoretical density may be calculated utilizing the following equation:

$$theoretical\ density\ \left[\frac{\mathrm{g}}{\mathrm{cm}^3}\right] = \frac{mass_{cell}}{volume_{cell}} \quad (1)$$

At room temperature (≈300 K), a UN unit cell has a mass of 1.6741×10^{-21} g with a lattice constant of 4.899 ± 0.001 Å [3] yielding a unit cell volume of 116.93x10^{-24} cm^3 116.93×10^{-24} cm^3. Utilizing equation 1 above, the theoretical density (TD) of UN at room temperature is 14.317 $\frac{g}{cm^3}$.

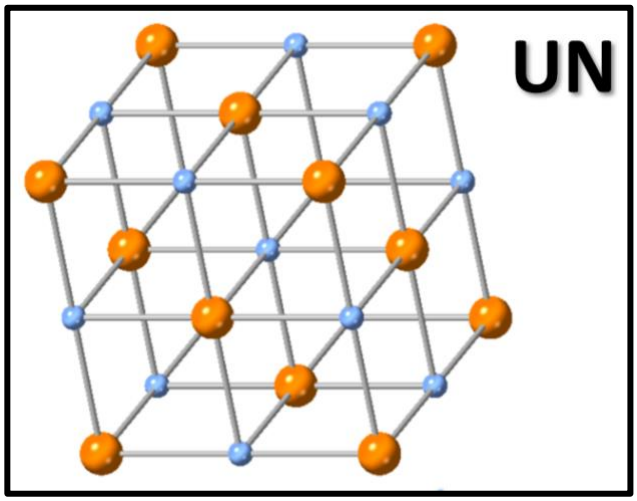

Figure 1.1: NaCl crystal structure of Uranium Mononitride.

Comparing UN to other nuclear fuels, such as Uranium Dioxide (UO_2), both fuels have cubic structure however UN has a rock salt (NaCl) crystal structure as seen in Figure 1.1 and UO_2 has a fluorite crystal structure as shown in Figure 1.2. What makes UN standout above other fuel types, in particular UO_2, is its high thermal conductivity (≈20.8 W/m-K at 1000 K), heavy metal (fissionable) density (13.5 g/cm^3 for UN versus 9.7 g/cm^3 for UO_2 [2]) and high melting temperature (3120 ± 30 K with over-pressure of 0.25 MPa N_2) [1]. Due to these properties, UN is becoming more accepted for its use in micro-reactors and other high temperature reactor systems.

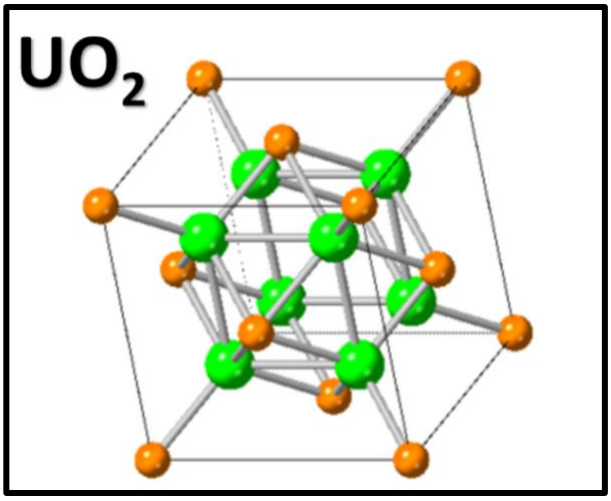

Figure 1.2: Fluoride crystal structure of Uranium Dioxide.

2. Unirradiated Fuel Properties

Knowing and understanding the material properties of a nuclear fuel provides the foundation for reactor design and safety analysis calculations. More specifically, the temperature dependency of these properties is vital to the accuracy of these designs and calculations. Additionally, porosity (i.e. percent from theoretical density) will directly impact these properties. A review of the available literature for the mechanical and thermal properties of UN is discussed below.

2.1. Mechanical Properties

Nuclear reactors operate under extreme conditions, such as high temperatures and irradiation fields, subjecting the fuel to conditions in which mechanical properties must be fully understood. By understanding these properties, various analyses can be conducted, such as determining the safe operations under both normal and accident conditions or fuel performance evaluation. As the fission process continues throughout the lifetime of the reactor, the fuel will begin to change due to the nature of the reactor fission process. Understanding how these changes effect the properties and geometric changes to the fuel will directly impact the safety analysis of the reactor. The discussion below will focus on the beginning of life, unirradiated fuel properties while irradiated fuel properties will be further examined in section three.

During reactor operations, when power increases for example, fuel pellets are subject to a high radial temperature gradient. The centerline temperature will be higher compared to the surface, causing this region to expand more compared to the surrounding volume. The uneven volumetric expansion develops thermal stresses and strains to form within the fuel pellet. If these induced thermal strains are large enough, the fuel pellet may permanently change shape (plastic deformation) and potentially undergo fracture (cracking).

To better understand the process in which a fuel pellet will exhibit these deformations and fractures, the elasticity and plasticity of the material must be known. Thermal gradient induces complex stress fields throughout the fuel element which to first order originates from the thermal expansion. These stresses can be either compressive or tensile. **The compressive fracture strength of a ceramic is typically ten to fifteen times greater than the tensile fracture strength therefore more effort is put forward understanding the tensile behavior of materials** [6, 7]. Figure 2.1 shows a general tensile stress-strain (σ-ε) curve for a material indicating specific regions of interest.

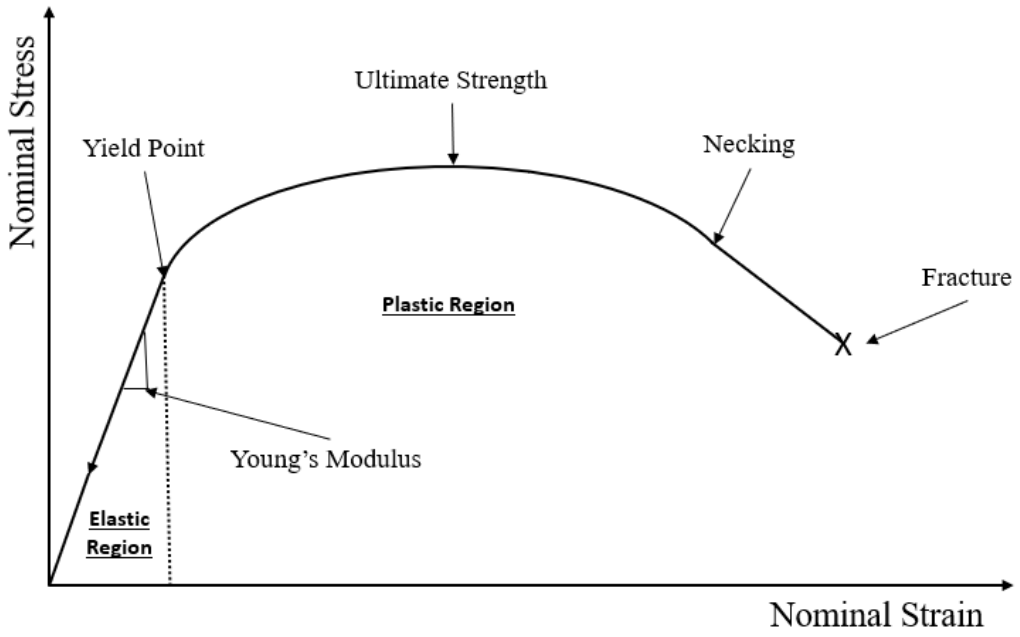

Figure 2.1: General stress-strain curve for an elastic-plastic material during tensile test.

When a material undergoes a tensile stress, from the initiation up to failure, it will undergo a series of changes best described by Figure 2.1. The first point of interest is indicated by the yield point. For any tensile stress, up to the yield point, the material will undergo elastic strains. When the load is removed, the elastic strain is recovered completely, and the material returns to its original shape (i.e. no permanent or plastic deformation). Once the stress reaches and surpasses the yield point, the material will begin to experience plastic strains. When the load is removed, the material will exhibit a certain level of plastic deformation, depending on the amount of tensile load applied. If the load continues, the material will reach a maximum point indicated by the ultimate strength, commonly referred to as the tensile strength. This is the maximum amount of stress a material can sustain while in tension before significant deformation exists. As the load continues, the material will begin to exhibit significant elongation known as necking, to the point of failure. This point signifies the fracture strength of a material.

Figure 2.2 is a general description of the tensile stress-strain curve for a more ductile material such as a metal. The stress-strain curves will have different shapes for different materials as seen in Figure 2.2. Material I is typical for many ceramics, Material II is typical for many metals, and Material III is typical for many elastomers. At typically microreactor operating temperatures (≈1000 K), UN is a ceramic material that will exhibit a curve like Material I. Ceramics are often tested in bending to develop a stress-strain curve. During this process, the material doesn't undergo a reduction in area (i.e. necking) and therefore it does not reach an ultimate strength. Instead, it passes through the elastic region, to the yield strength up to failure [6].

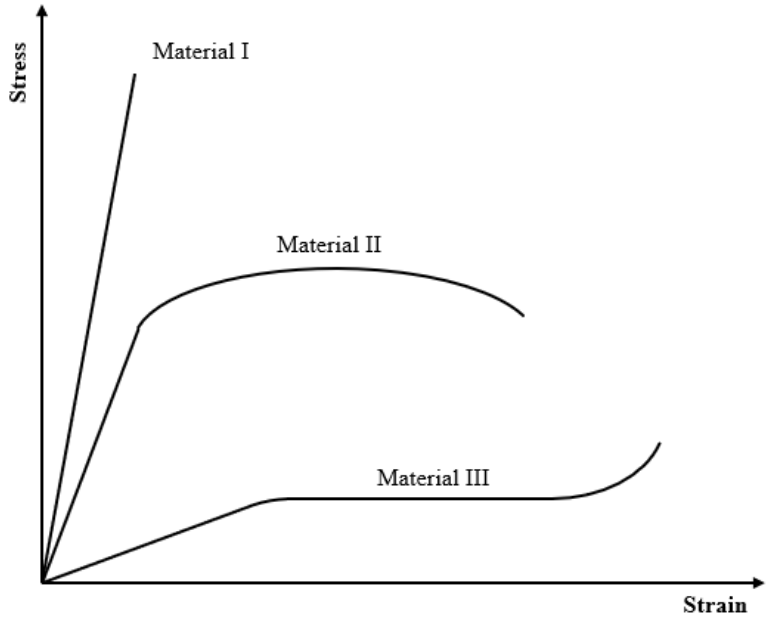

Figure 2.2: Idealized stress-strain curves for different material classes.

As previously stated, when a fuel pellet is subject to a radial temperature gradient, it will experience a maximum tensile stress on its surface. The maximum tensile stress is approximated by equation 2, assuming a constant power, thermal expansion coefficient and thermal conductivity [8]:

$$\sigma_{\theta,max} = \frac{E\ \alpha}{2(1-\nu)}(T_c - T_s) \tag{2}$$

where α is the coefficient of thermal expansion, E is Young's modulus, ν is Poisson's ratio and T is the fuel center-line temperature (T_C) or surface temperature (T_S).

The above equation indicates that the higher the temperature gradient, the higher the thermal tensile stress. If these tensile stresses reach the fracture strength, cracks in the fuel pellet will begin to form. Cracking may cause a degradation of the fuel material and thermomechanical properties. Cracks may also release any built-up fission products within the fuel pellet.

In the following sections, a compilation of experimental data for the mechanical properties of UN is presented. Data for elastic properties was collected using two different methods: dynamic resonant frequency method and ultrasonic echo-pulse method [9]. These two methods directly measure Young's modulus (E) and Shear modulus (G). The remaining elastic property is Poisson's ratio (ν). These three material properties are isotropically dependent and are related by equation 3.

$$G = \frac{E}{2(1+\nu)} \tag{3}$$

Thus, if one modulus is known the other can be approximated. Additionally, if both modulus variables are known experimentally, the Poisson's ratio may be found. Each elastic modulus property will be described in further detail below.

Data for elastic modulus has been collected by nine independent investigators: Honda and Kikuchi [10], Padel and deNovion [11], Whaley et al. [12], Hall [13], Muta et al. [14], Speidel and Keller [15], Taylor and McMurtry [16], Guinan and Cline [17], Adachi et al. [18], and DeCrescente et al. [19]. Of these, the first three utilized the dynamic resonant frequency method while the remaining six utilized the ultrasonic pulse method. Honda and Kikuchi and Muta et al. collected Young's Modulus only. Adachi et al. collected the Poisson's ratio directly, while calculating Young's Modulus utilizing the indentation method. Additionally, Hayes et al. [20] conducted a correlation analysis which will be referenced throughout.

Data for the thermal expansion of UN has been collected by four independent investigators: Speidel and Keller [15], Taylor and McMurtry [16], Carlsen and Harms [21], and DeCrescente et al. [19]. All experimental values were acquired utilizing the dilatometer method. Taylor and McMurtry experiments were conducted under vacuum while the others were performed in air. Oxidation on UN was noted when conducted in air.

In addition to experimental data for the elastic properties of UN, Kocevski et al. [22] performed a computational study utilizing ab initio molecular dynamics (AIMD). The study investigated various elastic material properties with both antiferromagnetic (AFM) and ferromagnetic (FM) ordering with respect to temperature. Utilizing this method, temperature dependent elastic properties were developed at elevated temperatures and are shown in Figure 2.3 below. Due to the variation in the elastic properties at the room temperature (≈300 K), a normalized temperature dependence is required. Therefore, a normalized linear temperature dependence for the elastic moduli and a normalized polynomial fit for Poisson's ratio was computed. The temperature dependencies are shown in Figure 2.3 as dashed lines as well as in the following equations:

$$Young's\ Modulus\ (E) = [1.0728 - 2.4269 \times 10^{-4}T] \tag{4}$$

$$Poisson's\ Ratio\ (v) = [0.9949 + 5.3524 \times 10^{-6}T + 3.9272 \times 10^{-8}T^2] \tag{5}$$

$$Shear\ Modulus(G) = [1.0702 - 2.3401 \times 10^{-4}T] \quad (6)$$

$$Bulk\ Modulus\ (K) = [1.0536 - 1.7869 \times 10^{-4}T] \quad (7)$$

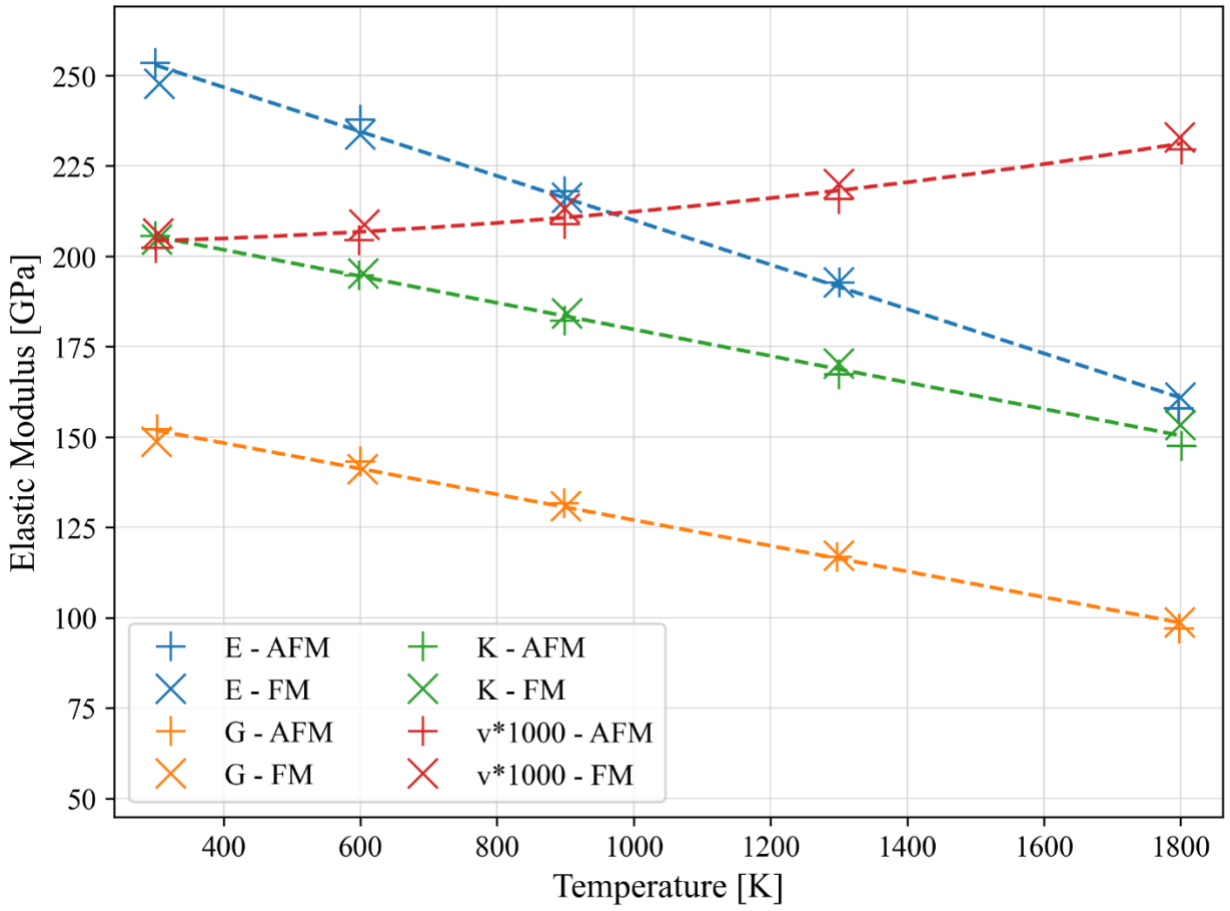

Figure 2.3: Computational data for Elastic Properties of UN versus temperature [22]. Young's modulus (*E*), shear modulus (*G*), bulk modulus (*K*), and Poisson's ratio (*v*). Temperature dependent correlations shown in dashed lines.

In the remaining sections, experimental data was collected from various sources. For each material property discussed, a best fit correlation was developed by using standard correlation curves and comparing the R^2 values. In each case, it was determined that a power-law fit achieve the lowest variance. Each correlation was checked by calculating the standard deviation for the respective data set utilizing the respective degrees of freedom for the curve, which for the power-law fit, the degrees of freedom is two. The residuals between the experimental data and the correlation curve were plotted and the distribution were analyzed as an additional verification. In each section below, two standard deviations are listed and plotted for visual representation along with the average and max difference between the experimental data and the correlation curve. To note, no theoretical data was included in the development of the correlation curves, rather the data is plotted to show a visual representation compared to experimental data.

2.1.1. Young's Modulus

Young's modulus (modulus of elasticity) is essential to understand the elastic behavior of a material. Young's modulus describes the materials ability to resist a uniaxial tensile or compressive stress without causing permanent deformation. In simpler terms, it describes the stiffness of a material. Tensile or compressive stress (σ) can be calculated by taking the ratio of the applied force (F) and area (A_0). The tensile (compressive) strain is calculated by taking the ratio of the total elongation (contraction) of the material ($\Delta l = l_i - l_0$) and initial length (l_0).

Young's modulus is the relationship between the stress and strain of a material under a given stress, which is indicated by the slope of the elastic region in Figure 2.1. Therefore, the steeper the slope, the higher the Young's modulus will be. This relationship is best described by Hooke's Law in equation 8 [7]:

$$\sigma = E\,\epsilon \tag{8}$$

where E is the Young's modulus, σ is stress (compressive or tensile) and ϵ is strain (compressive or tensile). A material with a high modulus will exhibit less elastic strain at a specified applied stress as compared to a material with a lower modulus. As temperature increases, atomic vibration within the crystal structure will increase, increasing the atomic distance within the crystal reducing the atomic force, overall reducing the Young's modulus.

Experimental data is plotted for UN Young's modulus with respect to porosity in Figure 2.4. All experimental data collected was on a UN sample at room temperature (300 K). Experimental data at elevated temperatures is not available in literature therefore the temperature relationship developed above will be utilized. It is seen that Young's modulus reduces as the sample's density moves further from the theoretical density. Using the linear dependence mentioned above, combined with a power-law fit form of the Young's modulus experimental data for UN a correlation was developed and is shown in equation 9. The resulting correlation for the Young's modulus of UN is valid for porosity ranging from 0% to 30% and temperatures ranging from 300 K to 1800 K. The correlation shown in Figure 2.4 is for a sample at room temperature:

$$E = 2.479x10^{-4}\,(D)^{3.013}[1.0728 - 2.4269 \times 10^{-4}T] \tag{9}$$

where E is the Young's modulus [GPa], D is the % of TD, and T is temperature in Kelvin. This trend is seen to fit with the experimental data shown in Figure 2.4. In addition to temperature and porosity, Young's modulus will be sensitive to various microstructural variables such as: pore shape and orientation, average grain size, porosity distribution, grain shape, grain orientation and impurity content.

The standard deviation between the experimental data and the correlation line was calculated and plotted in Figure 2.4. For Young's modulus, 28.1 GPa is equal to two standard deviations with all experimental data falling within 28% of the trend line with an average difference of 7%.

When analyzing the data spread with respect to theoretical density, UN samples with less than 20% porosity have all data points falling within 10% of the theoretical values.

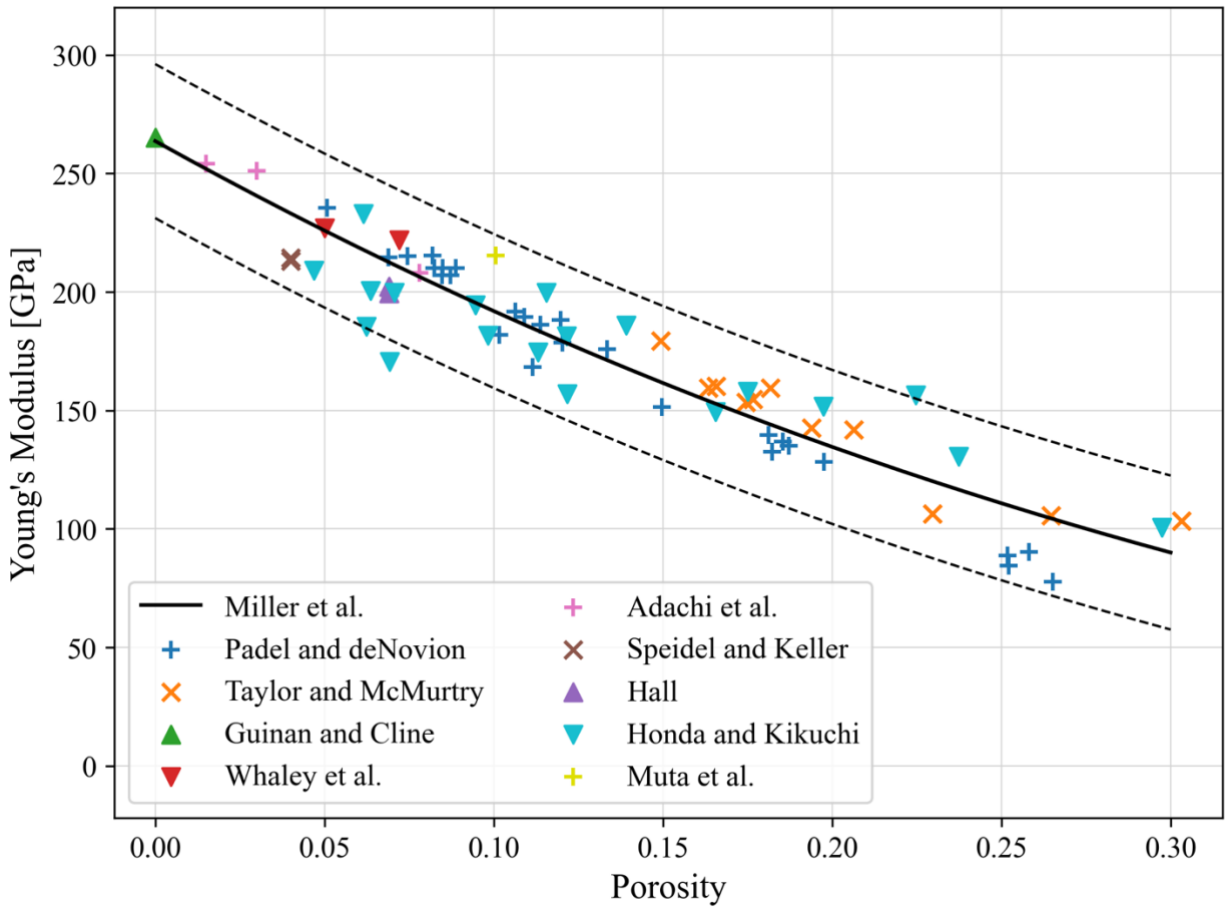

Figure 2.4: Experimental data for Young's modulus of UN versus porosity at room temperature[10-18]. ± 2σ is shown in plot with experimental data within ≤ 28% of trendline.

2.1.2. Poisson's Ratio

When a tensile force is applied to a material, there is an elongation in the direction of the applied force. Additionally, there is a contraction in the perpendicular direction. The elongation in the z-direction and the contraction in the x and y-direction causes a strain to exist. Strain in the x, y or z direction are determined by taking the ratio of the total elongation in their respective direction and the original length as seen by the following equation:

$$\epsilon = \frac{l_i - l_0}{l_0} = \frac{\Delta l}{l_0} \tag{10}$$

where ϵ is strain and l is the initial or original length of the specimen. Therefore, Poisson's ratio is defined as the ratio between lateral and axial strains:

$$v = -\frac{\epsilon_y}{\epsilon_z} \; OR \; -\frac{\epsilon_x}{\epsilon_z} \tag{11}$$

where v is Poisson's ratio, ϵ_x, ϵ_y and ϵ_z are the strains in the x, y and z-direction respectively. The negative sign is included to ensure Poisson's ratio is always positive. If Young's modulus and Shear modulus is known, Poisson's ratio may be determined utilizing equation 3.

Experimental data for UN's Poisson's ratio with respect to porosity is shown in Figure 2.5. All the experimental data was collected on a UN sample at room temperature. Like Young's modulus, experimental data at elevated temperatures is not available in literature therefore the temperature relationship developed above will be utilized. Observing Figure 2.5, it is seen that Poisson's ratio lowers as the sample's density moves further from the theoretical density. Using a power-law fit to the Poisson's ratio experimental data for UN combined with the temperature dependency above, a correlation was developed and is shown in equation 12. The resulting correlations for Poisson's ratio of UN is valid for porosity from 0% to 30% and temperatures ranging from 300 K to 1800 K.

$$v = 7.575x10^{-4}(D)^{1.286}[0.9949 + 5.3524 \times 10^{-6}T + 3.9272 \times 10^{-8}T^2] \tag{12}$$

where v is Poisson's ratio, D is percent of TD. This trend is shown in Figure 2.5. As with both moduli properties, Poisson's ratio will depend on the same microstructural variables: pore shape and orientation, average grain size, porosity distribution, grain shape, grain orientation and impurity content.

The standard deviation between experimental data and the correlation data was calculated and plotted in Figure 2.5. For Poisson's ratio, 0.029 is equal to two standard deviations with all experimental data falling within 21% of the trend line with an average of 5%. When analyzing the data spread with respect to theoretical density, UN samples with less than 20% porosity have all data points falling within 10% of the theoretical values.

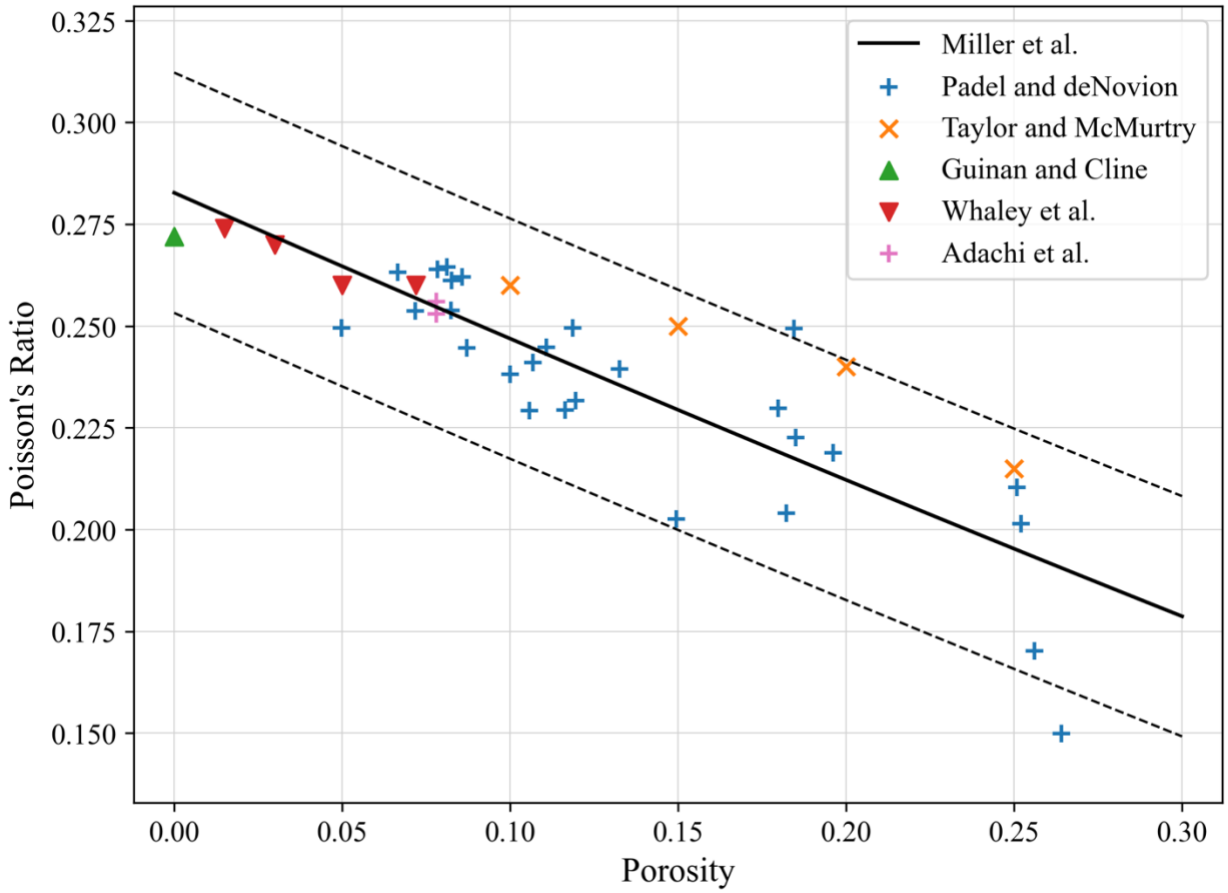

Figure 2.5: Experimental data for Poisson's ratio for UN versus porosity at room temperature [11, 12, 16-18]. ± 2σ is shown in plot with experimental data within ≤ 21% of trendline.

2.1.3. Shear Modulus

Shear modulus is another property essential to understanding the elastic behavior of a material. Shear modulus describes the materials ability to withstand a tangential force, without causing permanent deformation. Shear modulus is the measurement due to a shear stress rather than a tensile or compressive stress. In this figure, a transverse force (F) is applied to the top and bottom surface of the material. Shear strain (γ) is defined as the tangent of angle θ. Shear stress (τ) is the ratio of the applied force (F) to the area (A_0).

Like Young's modulus, Shear modulus can be found by taking the slope of the elastic region of a shear stress-strain curve. This is described by the following equation:

$$\tau = G\gamma \tag{13}$$

where τ is the shear stress, γ is the shear strain and G is the Shear modulus. According to experimental data, shear modulus is also greatly dependent on porosity.

Experimental data for UN's Shear modulus with respect to porosity is shown in Figure 2.6. All the experimental data was collected on a UN sample at room temperature. As with Young's modulus, experimental data at elevated temperatures is not available in literature therefore the temperature relationship developed above will be utilized. It is seen that shear modulus lowers as the UN density moves further from the theoretical density. Using a power-law fit form of the shear modulus experimental data for UN, a correlation was developed and is shown in equation 14. The resulting correlation for the shear modulus of UN is valid for porosity from 0% to 30% and temperatures ranging from 300 K to 1800 K. The correlation shown in Figure 2.6 is for a sample at room temperature (300 K).

$$G = 2.173x10^{-5}(D)^{3.353}[1.0702 - 2.3401 \times 10^{-4}T] \quad (14)$$

where G is the shear modulus [GPa], D is the percent of TD, and T is temperature [K]. This trend is seen to fit with the experimental data shown in Figure 2.6. As with Young's modulus, Shear modulus will depend on the same microstructural variables: pore shape and orientation, average grain size, porosity distribution, grain shape, grain orientation and impurity content.

The standard deviation between the experimental data and the correlation line was calculated and plotted in Figure 2.6. For shear modulus, 7.96 GPa is equal to two standard deviations with all experimental data falling within 15% of the trend line of theoretical values with an average of 5%. When analyzing the data spread with respect to theoretical density, UN samples with less than 20% porosity have all data points falling within 10% of the theoretical values except for the data by Taylor and McMurtry. Taylor and McMurtry data falls within 13%.

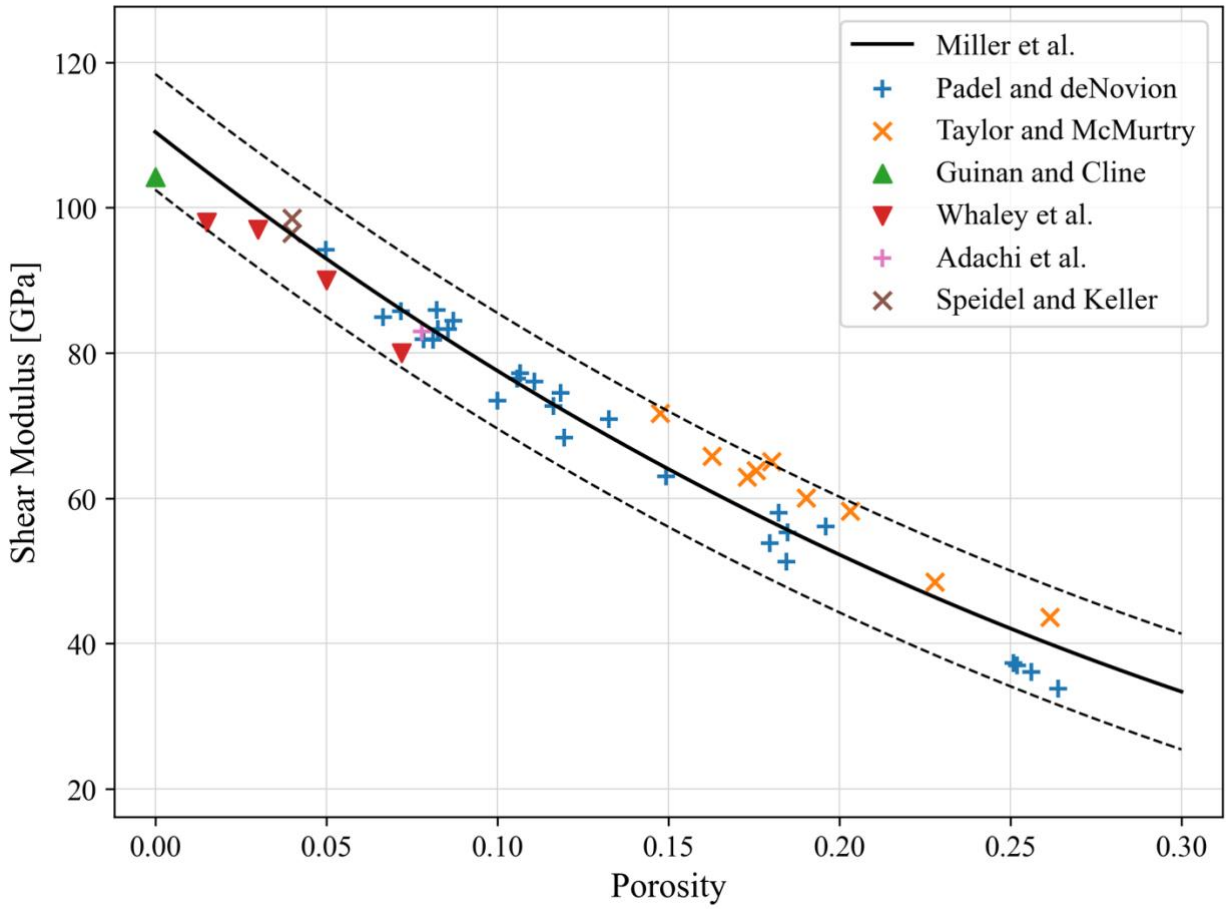

Figure 2.6: Experimental data for shear modulus of UN versus porosity [11, 12, 15-18]. ± 2σ is shown with experimental data within ≤ 15% of trendline.

2.1.4. Bulk Modulus

Bulk modulus describes the materials ability to withstand compression on all sides, sometimes referred to as incompressibility. It is the ratio of stress to strain for hydrostatic compression and is given by the following equation [7]:

$$K = -P\left(\frac{\Delta V}{V}\right) \tag{15}$$

where K is the bulk modulus, P is the applied pressure to the material, ΔV is the change in volume, and V is the original volume before compression. The negative sign indicates the reduction in volume due to the applied force. This equation describes the principle of Bulk modulus however it can be related to the other elastic properties of the material. Experimentally, Bulk modulus is not obtained directly, rather calculated based on two well-known relations between Young's modulus, shear modulus, and Poisson's ratio:

$$K = \frac{E}{3(1-2v)} \tag{16}$$

$$K = \frac{EG}{3(3G-E)} \tag{17}$$

where *K* is the bulk modulus, *E* is Young's modulus, *G* is shear modulus, and v is Poisson's ratio.

Experimental data for UN bulk modulus with respect to porosity is shown in Figure 2.7. All the experimental data was collected on a UN sample at room temperature. As with Young's modulus, experimental data at elevated temperatures is not available in literature therefore the temperature relationship developed above will be utilized. As stated above, all data presented below is calculated using equations 16 and 17. Using a power-law fit to the bulk modulus experimental data for UN, a correlation was developed and is shown in equation 18. The resulting correlation for the bulk modulus of UN is valid for porosity from 0% to 30% and temperatures ranging from 300 K to 1800 K. The correlation shown in Figure 2.7 is for a sample at room temperature (300 K).

$$K = 4.425 \times 10^{-8}(D)^{4.841}[1.0536 - 1.7869 \times 10^{-4}T] \tag{18}$$

where *K* is bulk modulus [GPa], *D* is the percent of TD, and *T* is temperature [K].

The standard deviation between the experimental data and the correlation line was calculated and plotted in Figure 2.7. For bulk modulus, 19.0 GPa is equal to two standard deviations with all experimental data falling within 27% of the trend line with an average 8%. When analyzing the data spread with respect to theoretical density, UN samples with less than 20% porosity have all data points falling within 10% of the theoretical values except for the data by Taylor and McMurtry. Taylor and McMurtry data falls within 15%.

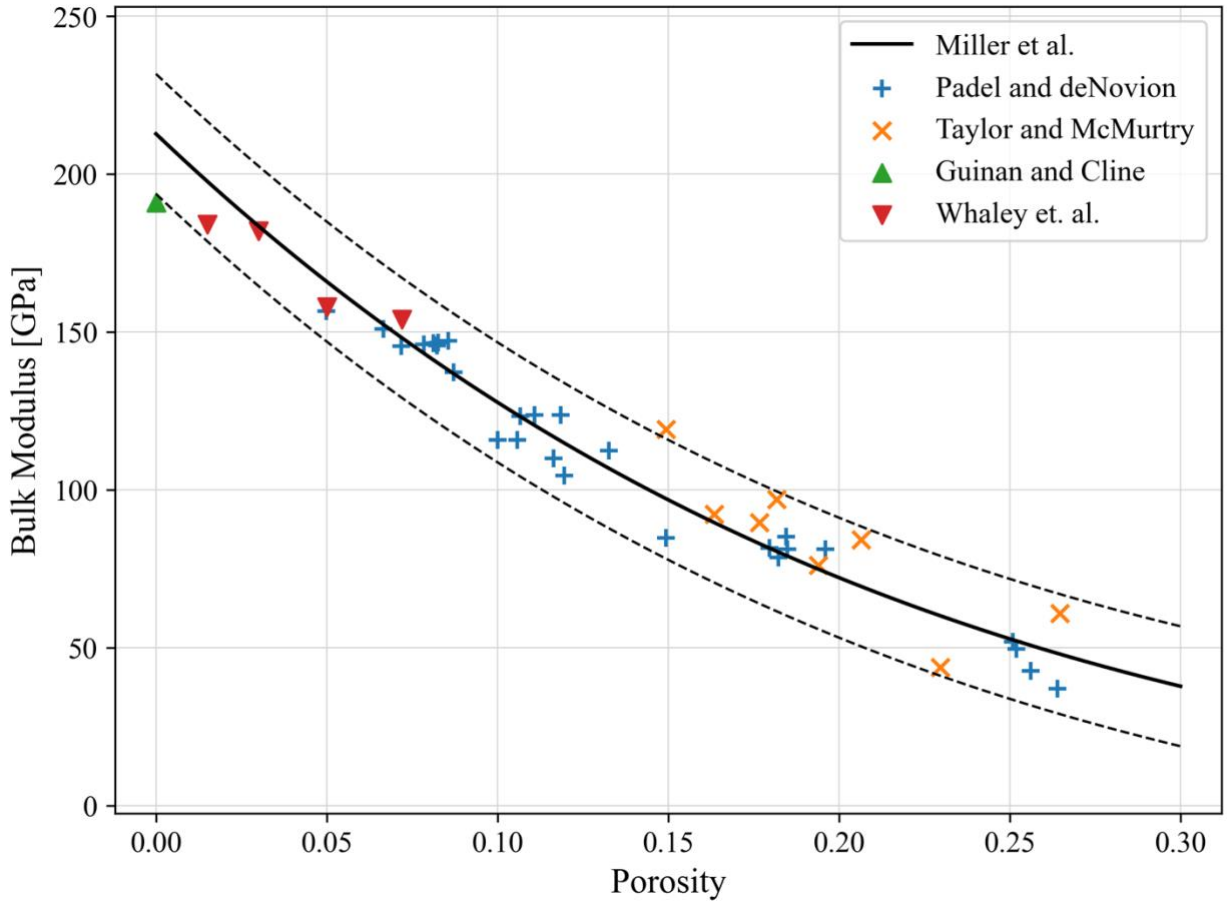

Figure 2.7: Experimental data for bulk modulus of UN versus porosity at room temperature [11, 12, 16, 17]. ± 2σ is shown in plot with experimental data within ≤ 27% of trendline.

2.1.5. Creep

Creep is the time dependent permanent deformation of a material when subjected to a constant stress or load as seen in Figure 2.8. With time, creep is separated into three stages: primary creep is high plastic deformation with a decreasing strain rate; secondary creep is where strain rate is relatively constant; tertiary creep is a rapid increase of strain rate typically leading to failure. For ceramics such as UN, this occurs when load is applied at elevated temperatures. Creep in ceramics become important for temperatures above approximately 50% of melting temperatures unlike UO_2 where it is approximately 40% [6, 8]. For UN, melting point is approximately 3120 K therefore creep rate is important around approximately 1560 K. Nuclear fuels are subject to a thermal gradient which induces a large thermal stress in the material. Thermal creep can cause permanent dimensional changes to the fuel. Revisiting Figure 2.1, the permanent deformation will shift the stress-strain curve, specifically the elastic region, to the right. When creep occurs, and the load is removed from the material, the material relaxation will not follow the original linear elastic region. An application of this is the permanent increase in radius of a fuel pellet, reducing the distance between the fuel and cladding surface. If the creep

rate is high enough, and the deformation is large enough, a fuel-cladding interaction may occur. While applications which utilize UN, may not operate at this elevated temperature, it is important to understand the mechanism.

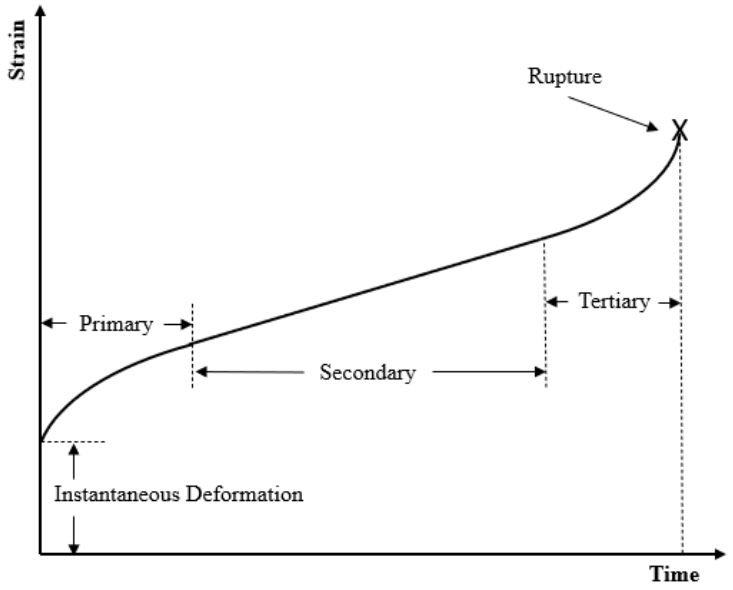

Figure 2.8: Typical creep curve of strain versus time at constant stress.

High temperature, steady-state creep rate is best described by the following equation [20]:

$$\dot{\varepsilon} = Ad^{-m}\sigma^{n}\exp\left(-\frac{Q}{RT}\right) \tag{19}$$

where A is an empirical constant, d is the grain size, m is the grain size exponent, σ is the applied load, n is the stress exponent, Q is the activation energy, R is the gas constant and T is temperature. A, m, n, and Q must be determined experimentally [20]. Due to the limited experimental data available and the various components effecting creep rate (i.e. stress, temperature, dislocation size), a figure of experimental data does not provide a beneficial visual representation and is therefore not provided. Instead, the analysis performed by Hayes et al. [20], is discussed.

Hayes et al. [20] performed an analysis and developed a correlation for temperatures ranging from 1770 K to 2083 K and stresses ranging from 20 MPa to 34 MPa. The UN creep data utilized was from the work of Fassler et al. [23], Vandervoort et al. [24], and Massaaki and Michio [25]. To determine the stress exponent, the slope of the log of creep and temperature was calculated for specified stresses for each experimental data set. The average of the stress exponent was 4.5, indicating that UN follows a dislocation climb mechanism at high temperatures which is indicated by a stress exponent ranging from 2.5 to 5.0 [26]. Concluding that UN creep is dominated by dislocation climb, creep rate is therefore independent on grain

size and grain size exponent is set to zero. Based on the creep rate variations between a hypo-stoichiometric, porous sample and a stoichiometric, theoretically dense sample, it was concluded that porosity has a significant impact on the creep rate. However, due to the limited experimental data available, the correlation as seen in equation 20 assumes a theoretically density UN [20]:

$$\dot{\varepsilon} = 2.054 \times 10^{-3} \sigma^{4.5} \exp\left(-\frac{39369.5}{T}\right) \tag{20}$$

where $\dot{\varepsilon}$ creep rate [1/s], σ is applied stress [MPa], and T is temperature [K]. This relation is specific to experimental testing conditions as specified above. From the limited experimental data, dislocation climb mechanism was seen to be accurate at low temperatures and equation 20 yields reasonable values down to ≈1350 K.

While the above equation is only valid for theoretical density, a porosity correction value can be used to correct for the difference in densities [20]:

$$f(p) = \frac{0.987}{(1-P)^{27.6}} \exp(-8.65P) \tag{21}$$

where P is the porosity (volume fraction) of UN. To obtain to correct creep rate, the value of equation 20 must be multiplied by equation 21.

2.1.6. Coefficient of Thermal Expansion

The coefficient of thermal expansion (CTE) describes the way in which a material expands due to heat. A linear CTE is given by the following equation [8]:

$$\frac{\Delta l}{l} = \alpha \Delta T \tag{22}$$

where Δl is the change in length, l is the original length, α is the CTE [1/K] and ΔT is the change in temperature [K]. Using equation 22, a volumetric change can be calculated by replacing length with volume which signifies the volume coefficient of thermal expansion.

As described above in equation 2, thermal expansion plays a vital role in determining the if a fuel pellet may fracture or the extend in which it will thermally expand. Reactors are subject to thermal cycles, particularly within the fuel matrix, causing thermal stresses to exist. Additionally, fuel rods are designed with minimal clearance between the fuel and the cladding material which surrounds it. Understanding fuel pellet expansion may help predict a pellet-clad mechanical interaction and the stresses it may induce on the cladding structure. In addition, understanding thermal expansion will provide insight into the thermal fatigue due to cycling.

Experimental data for UN thermal expansion with respect to temperature is shown in Figure 2.9. DeCrescente et al. [19] tested a UN sample with 94 percent of TD, Carlsen and Harms [21]

tested a sample that was 91.5 percent of TD, Taylor and McMurtry [16] tested a sample that was 89.0 percent TD and Speidel and Keller [15] tested a sample that was 97.6 percent TD. UN with a higher porosity will yield a lower thermal expansion. Hayes et al. utilized the change in lattice parameter to develop a best fit for the coefficient of thermal expansion. Hayes et al. [27] used the change in distance between lattice parameter and equation 22 above to develop a linear correlation for UN thermal expansion with respect to temperature. This is given by equation 23. This correlation is valid for temperatures from 298 K to 2523 K [27].

$$\alpha = 7.096x10^{-6} + 1.409 \times 10^{-9}T \tag{23}$$

The above correlation is plotted against available data in Figure 2.9. It was determined that a power-law fit best described the UN coefficient of thermal expansion based on the correlation development methods described in section 2.1. For this reason, the following correlation was developed valid for temperatures ranging from 298 K to 2523 K and for porosity ranging from 0% to 20% and is plotted in Figure 2.9.

$$\alpha = 2.089 \times 10^{-6} (T)^{0.209} \tag{24}$$

The standard deviation between the experimental data and the correlation line was calculated and plotted in Figure 2.9. For thermal expansion, $6.453 \times 10^{-7} \frac{1}{K}$ is equal to two standard deviations with all experimental data falling within 13% of the trend line with an average of 3%. Comparing the difference between experimental data and theoretical values from the two correlations provided above, the adjusted power-law fit reduces the spread on average by a factor of three.

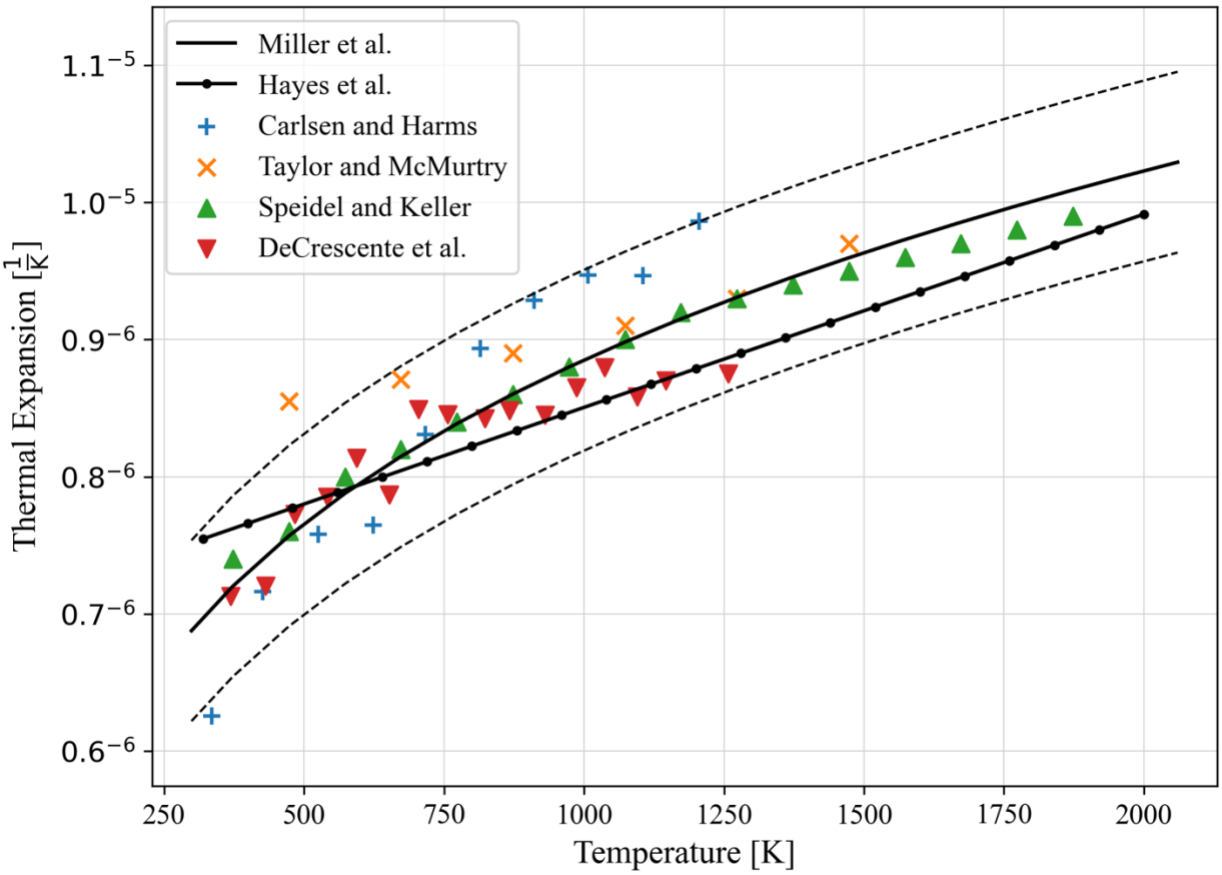

Figure 2.9: Experimental data for thermal expansion versus temperature [15, 16, 19, 21]. ± 2σ is shown in plot with experimental data within ≤ 13% of trendline.

2.1.7. Uranium and Nitrogen Self-Diffusivity

The diffusion properties in UN are less studied than the diffusion properties in other more common nuclear fuels, for example, UO_2. There are however several experimental studies of U and N diffusion in UN as well as recent data-driven approaches and cluster dynamics simulation methods that can be used to determine the diffusivity of various species in UN.

There are several experimental sources for N diffusion in UN. Holt and Almassy used alpha particle activation to measure N diffusion coefficient in UN [28]. DeCrescente et al. [19] also performed measurements of N diffusion. The DeCrescente et al. diffusion values are sometimes often noted as being too high compared to other sources due to the specific experimental technique that was used to obtain them. However, a change in temperature scales in the reported data from Celsius to Kelvin makes these values well aligned with the diffusion values measured by other sources. The rationale for this change arises from unit ambiguity in the original report of that data. Matzke [29] also reported values for N diffusivity across various temperatures. Three primary theoretical techniques can be used to predict N diffusivity: empirical models, simulations, and data-driven methods. Cooper et al. [30] developed and calibrated a cluster

dynamics model to predict the diffusivity of N in UN with excellent agreement observed between the simulated values and experimental data. It should be noted that the agreement between the simulation and experiment is in part because the cluster dynamics model is calibrated to generate the experimental data. Craven et al. [31] used the Cooper et al. [30] model coupled with a genetic optimization procedure to predict N diffusion at various thermodynamic state points. The results of this data-driven procedure are in excellent agreement with experimental results. Johnson et al. [32] developed a machine learning surrogate model to predict N diffusion. Figure 2.10 shows the experimental data for N diffusion along with a fit to the data. The fit to the Matzke [29] N diffusion data is:

$$D_{\text{Matzke}}\ [\text{m}^2/\text{s}] = 3.0 \times 10^{-8} \exp[-31680.3/T] \tag{25}$$

where T is temperature in K. In this work, the following correlation was developed valid for temperatures ranging from 1400 K to 2400 K:

$$D_N\ [\text{m}^2/\text{s}] = 1.255 \times 10^{-65}\ (T)^{15.294} \tag{26}$$

The standard deviation between the experimental data and the correlation line was calculated and plotted in Figure 2.10. For N diffusion, $1.199\times10^{-14}\ \frac{m^2}{\text{s}}$ is equal to two standard deviations with all experimental data falling within 144% of the trend line with an average of 32%.

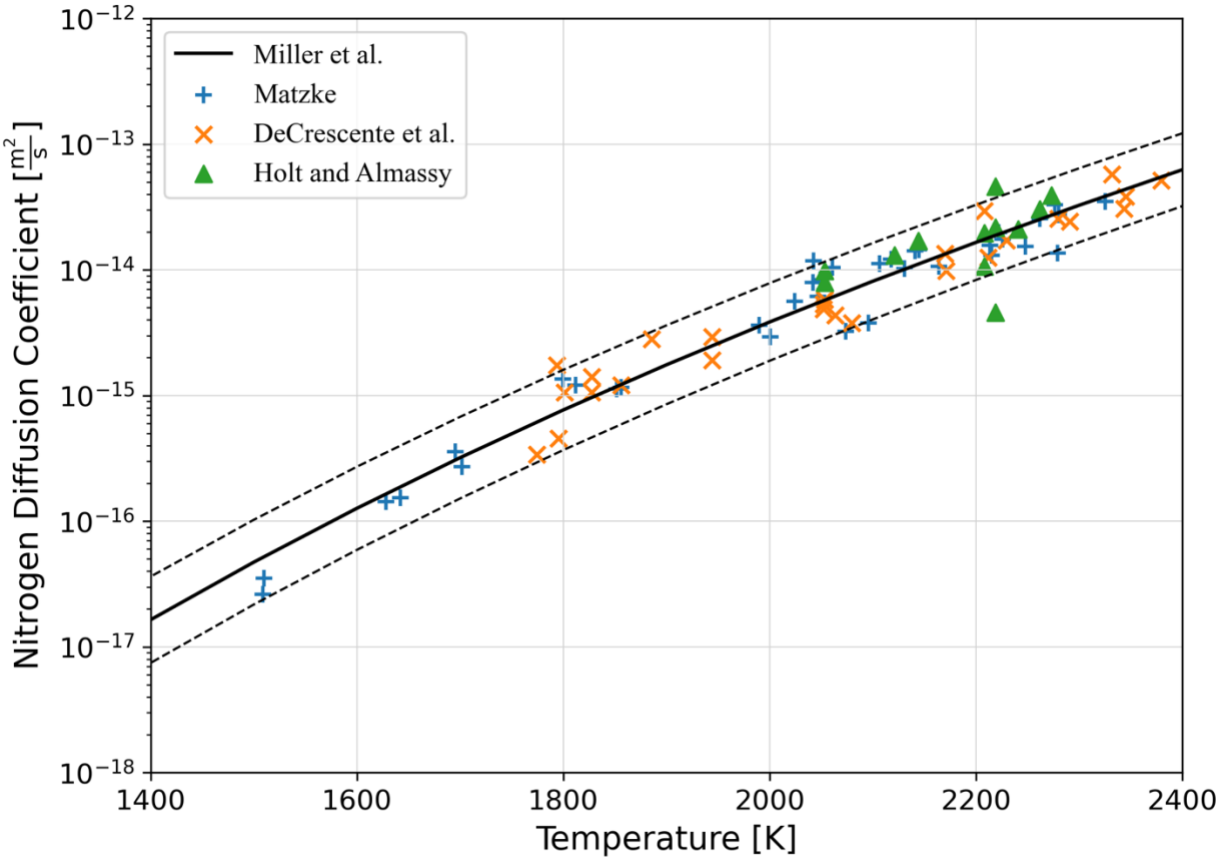

Figure 2.10. Experimental data for nitrogen self-diffusion versus temperature [19, 28, 29]. ± 2σ is shown in plot with experimental data within ≤ 32% of trendline.

There is limited data available for U diffusion in UN. Reimann et al. [33] investigated U diffusion using the alpha energy degradation method. Those results are in qualitative agreement with defect chemistry calculations. The Reimann data gives U diffusion coefficients as a function of temperature and the partial pressure of nitrogen. Matzke [34] generated U diffusion data at various temperatures at two different partial pressures. The Matzke diffusion results for are shown in Figure 2.11. Note that the Matzke results are taken at two different pressures, but here we have combined that data into one dataset. A fit to the Matzke U diffusion data taking into account only data taken at 0.1 MPa gives:

$$D_{\text{Matzke}}\ [\text{m}^2/\text{s}] = 5.4 \times 10^{-7} \exp\left[-\frac{58022.6}{T}\right] \tag{27}$$

The standard deviation between the experimental data and the correlation above was calculated and is plotted in Figure 2.11. For U diffusion, $3.726\times10^{-19}\ \frac{m^2}{s}$ is equal to two standard deviations with all experimental data falling within 49% of the trend line with an average of 29%.

Hayes et al. [35] developed a correlation for U diffusion:

$$D\ [\mathrm{m^2/s}] = 2.215 \times 10^{-11}(P_N)^{0.6414}\exp\left[-\frac{7989.3}{T}\right] \tag{28}$$

where P_N is the partial pressure of nitrogen and T is temperature in K. When applied to the Reimann et al. data, the Hayes et al. analytical model systematically underestimates the U diffusion values and generates several points with significant error [31]. Craven et al. [31] and Cooper et al. [30] respectively developed a machine learning method and a cluster dynamics method to predict U diffusivity, with strong agreement observed between the predicted values and the experimental results in both cases.

In this work, the following correlation was developed combining both pressures and is valid for temperatures ranging from 1900 K to 2200 K:

$$D_U\ [\mathrm{m^2/s}] = 1.604 \times 10^{-106}\ (T)^{26.264} \tag{29}$$

The standard deviation between the experimental data and the correlation line was calculated and plotted in Figure 2.11. For U diffusion, $2.267\times10^{-19}\ \frac{m^2}{s}$ is equal to two standard deviations with all experimental data falling within 175% of the trend line with an average of 65%.

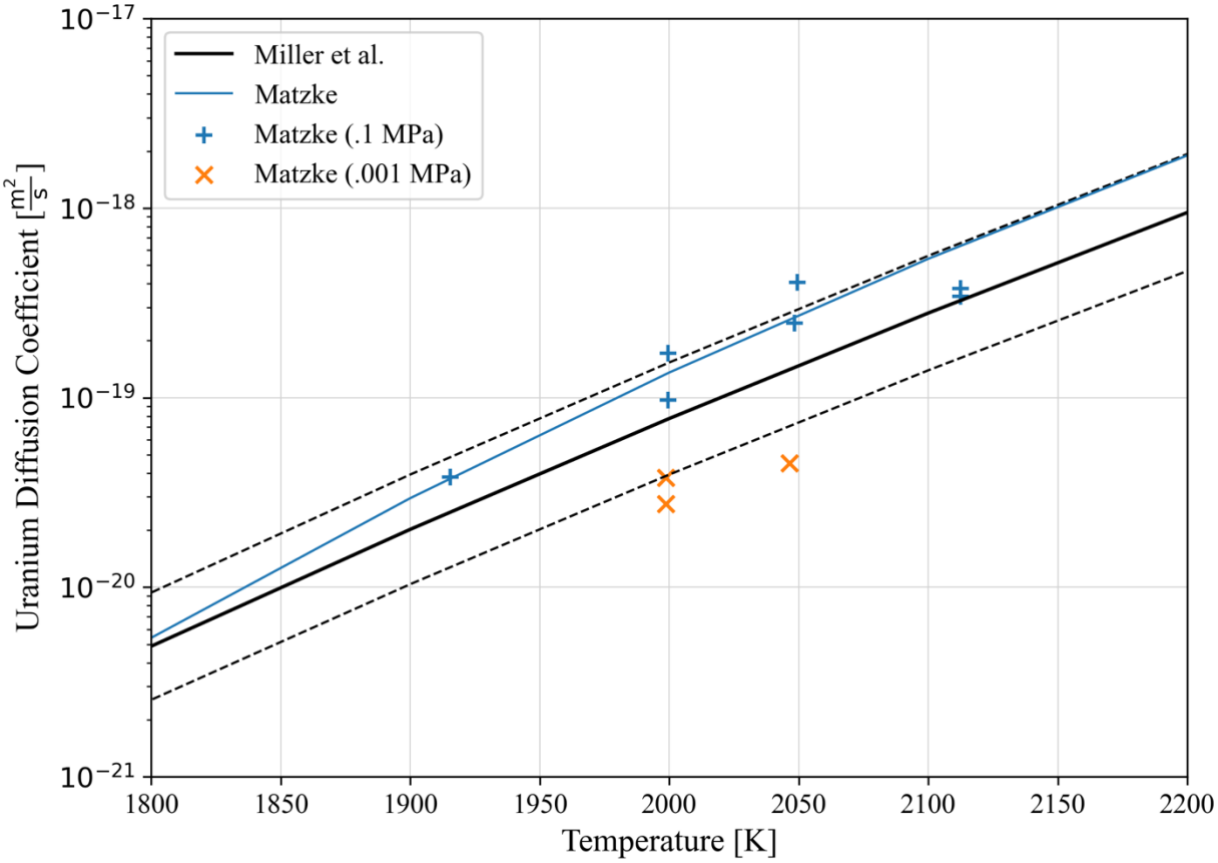

Figure 2.11. Experimental data for nitrogen self-diffusion versus temperature [34]. ± 2σ is shown in plot with experimental data within ≤ 65% of trendline.

2.2. Thermal Properties

Material selection for nuclear reactors is influenced by the thermal response to temperature changes, thermal gradients, and elevated temperatures. For example, the thermal conductivity of the nuclear fuel will impact the maximum temperature that will occur in the center of the fuel. The higher the thermal conductivity is, the easier heat will transfer through the fuel, reducing the temperature difference between the center and surface of the fuel. The following sections will detail the various thermal properties of UN.

2.2.1. Thermal Conductivity

Thermal conduction is a process in which heat is transferred across a material due to a temperature gradient. This heat will flow from a high to low gradient. The property that defines this process is known as thermal conductivity. This is illustrated by the following equation:

$$\frac{dq}{dt} = -k\,\frac{dT}{dx} \tag{30}$$

where $\frac{dq}{dt}$ is rate of heat flow per time, k is a constant of proportionality, and $\frac{dT}{dx}$ is the temperature gradient across the material. The constant of proportionality is thermal conductivity. Thermal conductivity has units of $\frac{\mathrm{W}}{\mathrm{m\,K}}$ and the minus sign indicates heat flow is high to low gradient.

Heat is transferred by two primary physical mechanisms in materials: lattice vibrations (phonons) and free electrons [7]. When both mechanisms are present, the total thermal conductivity is the combination of the two. When the thermal conductivity of the material is dominated by lattice vibrations, the thermal energy is transported across the material by the movement of phonons from a region of high temperature to low temperature [6]. This is the most common mode for ceramics. When the heat transfer is dominated by free electrons, it is controlled by electronic thermal conduction [7]. Free electrons gain kinetic energy from a source of high energy (high temperature), begin to freely move throughout the material to a lower temperature, imparting energy on atoms. The mobility of phonons is typically much lower than free electrons because they require a scattering by lattice vibrations rather than the free movement. Therefore, ceramic thermal conductivities are typically lower when compared to metals [6].

Phonon transport is heavily influenced by defects that can form under irradiation such as fission products on the lattice, point defects, and to a lesser extent, dislocations. However, experimental data does not detail the differentiation between the two modes of heat transfer creating difficulties in understanding the potential change in a material's thermal conductivity. Therefore, to better understand these thermophysical properties of a material, multiple computational methods have been developed. The following methods and codes were utilized to better understand UN and are presented below: LDA+DMFT [36], molecular dynamics (MD)[37], Quantum Espresso (QE) code [38, 39], and ab initio molecular dynamics (AIMD) [22]. **These methods agree and conclude that contrary to most ceramics, UN is dominated by free electron movement, and it is seen that thermal conductivity increases with temperature**. It was reported by Yin et al. [36], that at 1000 K phonon contribution was only 4.4 $\frac{\mathrm{W}}{\mathrm{m\,K}}$ while the free electron contribution was 12.1 $\frac{\mathrm{W}}{\mathrm{m\,K}}$. As seen in Figures 2.14 and 2.15, the total thermal conductivity of 16.5 $\frac{\mathrm{W}}{\mathrm{m\,K}}$ is lower than experimental data however compares well with the MD method of Kurosaki et al. [37]. The discrepancies were reported to be most likely due to excitation within the material that can conduct heat which are not included in the methods mentioned above [36].

Shown in Figure 2.12, thermal conductivity of UN increases with temperature. Conversely, UO_2 has a decrease in thermal conductivity with temperature common of a material dominated by the movement of phonons. The comparison of these two materials is shown in Figure 2.12.

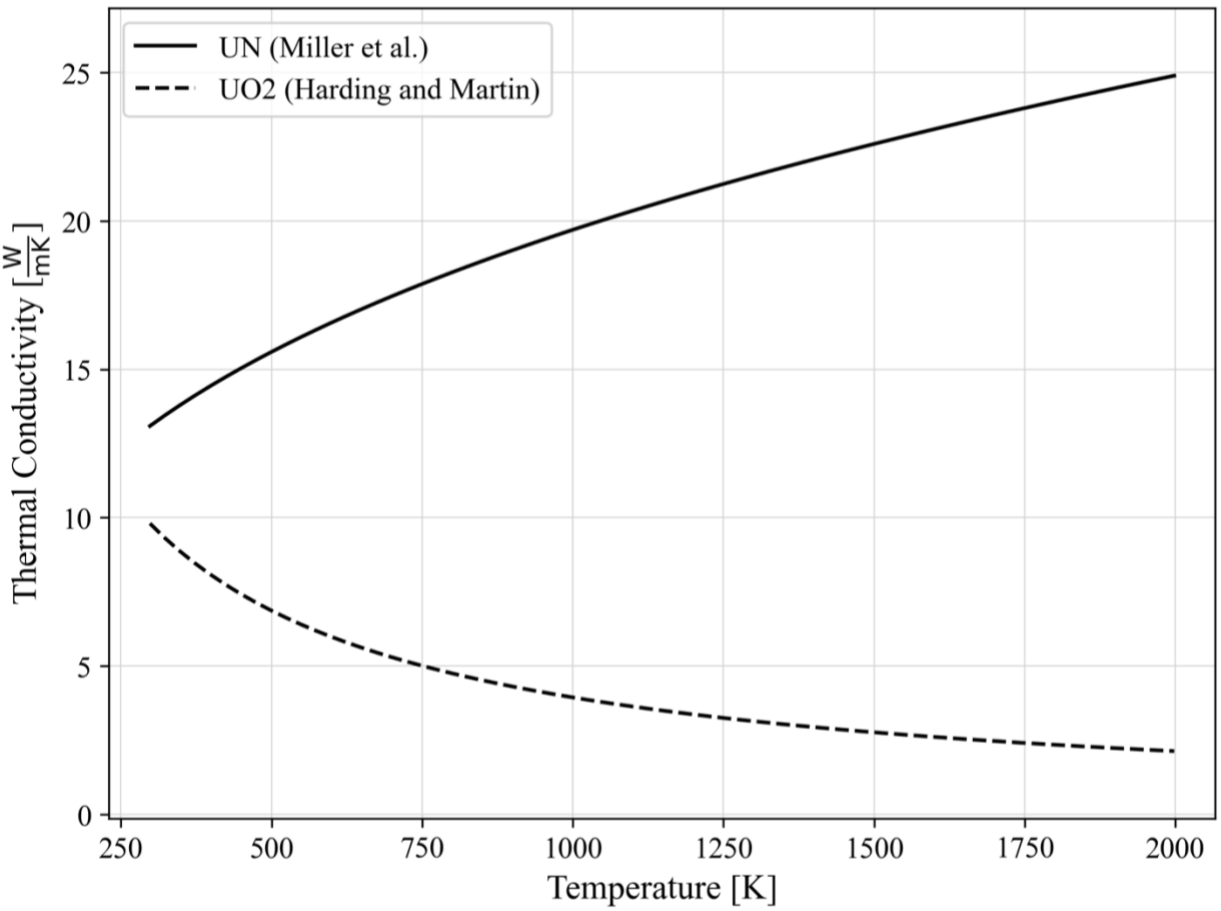

Figure 2.12: Comparison of thermal conductivity for UN and UO2 [40].

Porosity of a material can be described as the difference of a materials density compared to the theoretical density primarily due to pockets of gas within the material. Thermal conductivity of air is as low as 0.026 $\frac{W}{m\,K}$, thus the porosity of UN will significantly impact its overall thermal conductivity [6]. Kikuchi et al. [41] conducted a study to analyze the thermal conductivity of UN at densities ranging from 70.5% to 95.5%. The results are shown in Figure 2.13. From this data, it is noted that UN thermal conductivity decreases on average 12.5% for every 5% reduction in density.

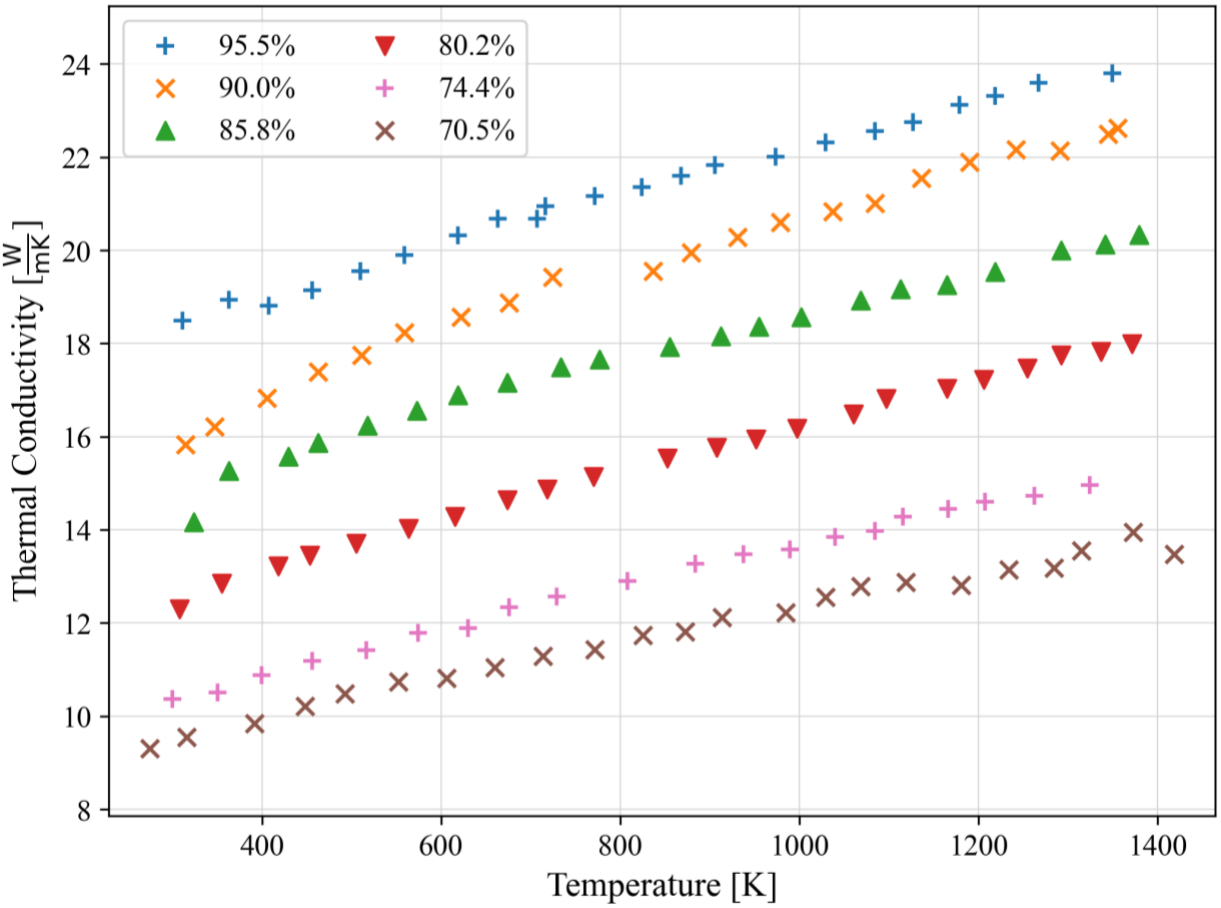

Figure 2.13: Experimental data for thermal conductivity of UN versus temperature for various porosities [41].

Experimental data for thermal conductivity was collected by seven separate investigators: Kocevski et al. [22], Takahashi et al. [42], Moore et al. [43], Kollie and Moore [44], Speidel and Keller [15], Muta et al. [14], Hayes and DeCrescente [45], Endebrock et al. [46], and Kikuchi et al. [41]. Experimental data for UN's thermal conductivity with respect to temperature is shown in Figures 2.14 and 2.15. Figure 2.14 shows data for UN sample at experimental density while Figure 2.15 shows data corrected to 100% TD utilizing the following correction factor [47]:

$$k_p = k_{100} \exp(-2.14P) \tag{31}$$

where k_p is the thermal conductivity of the sample, k_{100} is the thermal conductivity at 100% TD, and P is the volume fraction porosity.

The general shape for thermal conductivity versus temperature is consistent throughout each experimental data set. However, there is a significant deviation based on porosity. To better understand the difference, an investigation into the fabrication of each sample was conducted. Important fabrication and material composition data is provided in Tables I and II. Comparing Table II with Figure 2.14, the only clear correlation is that the oxygen concentration in the UN

lowers the thermal conductivity. Bringing attention to the 89.9% TD sample of Takahashi et al. [42], the lowest thermal conductivity is related to the highest oxygen concentration. Similarly, comparing the two samples produced by Speidel and Keller [15], the sample with the higher oxygen concentration generally yields a lower thermal conductivity.

As shown in Figure 2.14 and 2.15, three independent computational methods were utilized to determine thermal conductivity of UN. Kocevski et al. [22] utilized the AIMD method as describe earlier. The calculated data appears to be greater than the experimental data. This was suggested to be due to the electronic contribution to the total thermal conductivity. Yin et al. [36] utilized the LDA+DFMT method. The calculated thermal conductivity for 1000 K falls below experimental data. Yin et al. [36] suggests that there may be other excitations that can conduct heat throughout UN which are not accounted for in their calculations. Finally, Kurosaki et al. [37] utilize the MD method. This method appears to be in good agreement with experimental data.

There seems to be additional influences that are not immediately obvious with the supplied data. It is mentioned throughout the literature that grain size, grain boundaries, dislocations, and impurities may have an impact on the thermal conductivity. It is concluded that all thermal conductivities observe a similar upwards trend, and all depend on the porosity of the material. At this point, it is sufficient to correlate the data with a temperature and porosity dependency.

Table I: Fabrication data for UN fuel pellets used in thermal conductivity comparison.

Author	**Heat Treatment**	**Temperature [K]**	**Time [Hr]**	**Fabrication Atmosphere**
Kocevski et al. [22]	Sintered	2475	8	H_2/N_2
Takahashi et al. [42]	Arc Melted*	1873	5	Nitrogen
	Sintered*	1773 / 1973	1.5 / 4.5	Vacuum / Nitrogen
Moore et al. [43]	Sintered	2500	8.5	Nitrogen
Kollie and Moore [44]	-	-	-	-
Speidel and Keller [15]	Isostatic Hot Pressing*	1563 / 1753	3 / 3	Air / Niobium
	Isostatic Hot Pressing	1753	4	Niobium
Muta et al. [14]	Spark Plasma Sintered	1773	≈0.5	Nitrogen-Hydrogen
DeCrescente et al. [19]	Cold Pressed / Sintered	1810 / 2533	1 / 4	Vacuum / Nitrogen-
Kikuchi et al. [41]	Sintered	2073	4	Argon
Endebrock et al. [46]	Arc Melted	-	-	-

Table II: Material composition for UN fuel pellets used in thermal conductivity analysis.

Author	% TD	Oxygen (wt. %)	Nitrogen (wt. %)
Kocevski et al. [22]	95.0	< 0.02	-
Takahashi et al. [42]	100.0	0.063	5.18
	89.9	0.085	5.65
Moore et al. [43]	97.0	< 1.0	-
Kollie and Moore [44]	94.5	-	-
Speidel and Keller [15]	98.0	0.047	5.32
	97.0	0.0	5.38
Muta et al. [14]	89.9	-	-
DeCrescente et al. [19]	94.0	.07	5.32
Kikuchi et al. [41]	95.5	0.022	-
Endebrock et al. [46]	100.0	-	-

Ross et al. [48] performed a correlation study to better estimate thermal conductivity over a wider range of temperature with a porosity dependence. The resulting correlation for the thermal conductivity of UN is valid for porosity from 0% to 7% and temperatures ranging from 10 K to 1923 K.

$$k = 1.37T^{0.41}\left(\frac{1-P}{1+P}\right) \tag{32}$$

where k is thermal conductivity $\left[\frac{\mathrm{W}}{\mathrm{m\ K}}\right]$, P is the volume fraction porosity, and T is temperature [K].

With additional data becoming available, Hayes et al. [35] developed a new power-law fit form for thermal conductivity with a temperature and porosity dependence. Utilizing the porosity correction factor developed by Peddicord et al. [47], the resulting correlation for the thermal conductivity is valid for porosity from 0% to 20% and temperatures ranging from 298 K to 1923 K.

$$k = 1.864\exp(-2.14P) \times T^{0.361} \tag{33}$$

where k is the thermal conductivity $\left[\frac{\mathrm{W}}{\mathrm{m\ K}}\right]$, P is the volume fraction porosity, and T is temperature [K].

Additional data for UN thermal conductivity has become available since the correlation was performed by Hayes et al. [35]. Utilizing the same porosity correction factor, and a power-law fit, the following correlation has been constructed valid for porosities 0% to 20% and temperatures 298 K to 1923 K:

$$k = 2.123\exp(-2.14P) \times T^{0.338} \tag{34}$$

where k is thermal conductivity $\left[\frac{\mathrm{W}}{\mathrm{m\,K}}\right]$, P is volume fraction porosity, and T is temperature [K]. This correlation is seen in Figure 2.14 for a porosity of 2% and in Figure 2.15 for a porosity of 0%.

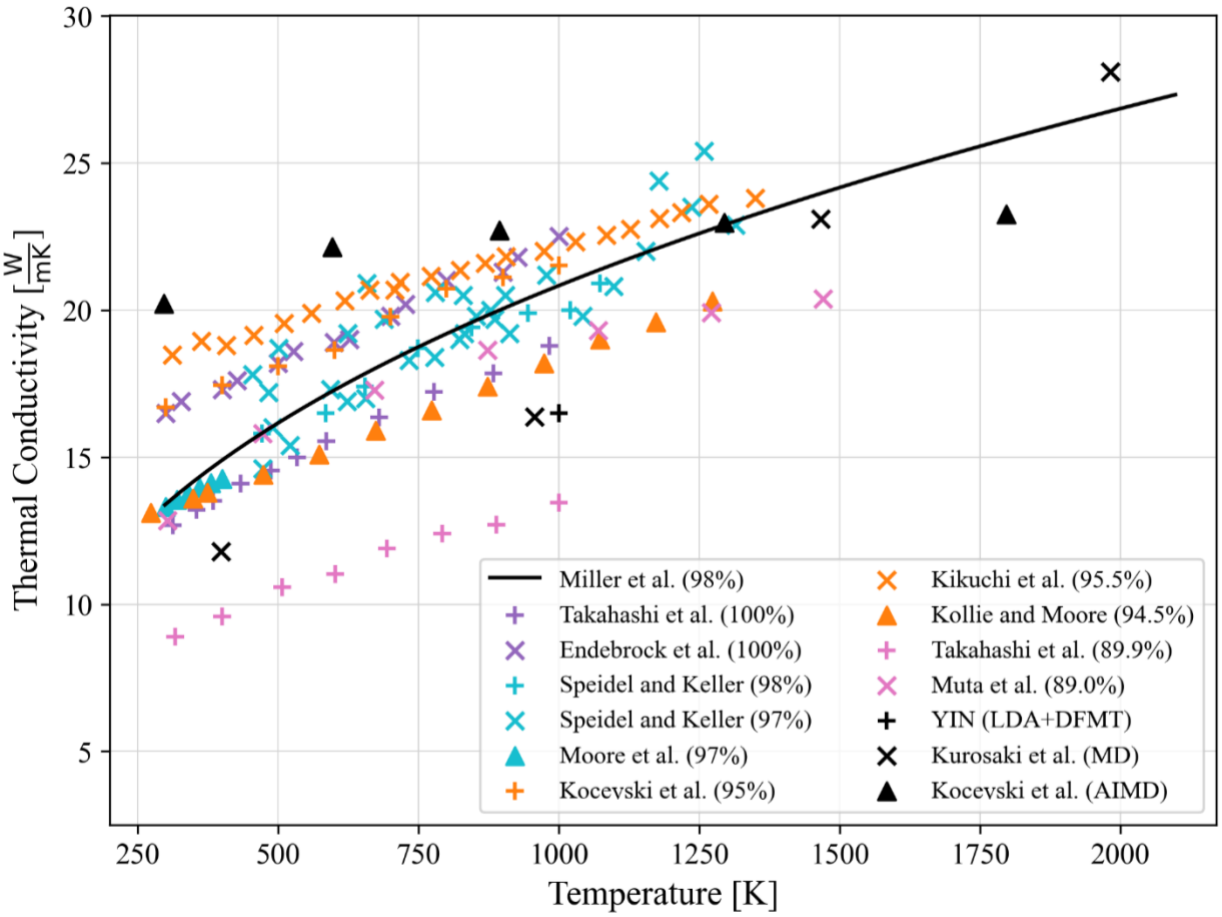

Figure 2.14: Experimental data for thermal conductivity versus temperature for UN at experimental porosities [14, 15, 22, 36, 37, 41-46].

The standard deviation between the experimental data and the correlation was calculated for a thermal conductivity corrected to 100% and is plotted in Figure 2.15. For thermal conductivity, 5.03 $\frac{\mathrm{W}}{\mathrm{m\,K}}$ is equal to two standard deviations with the experimental data falling within 39% of the trend line with an average of 11%.

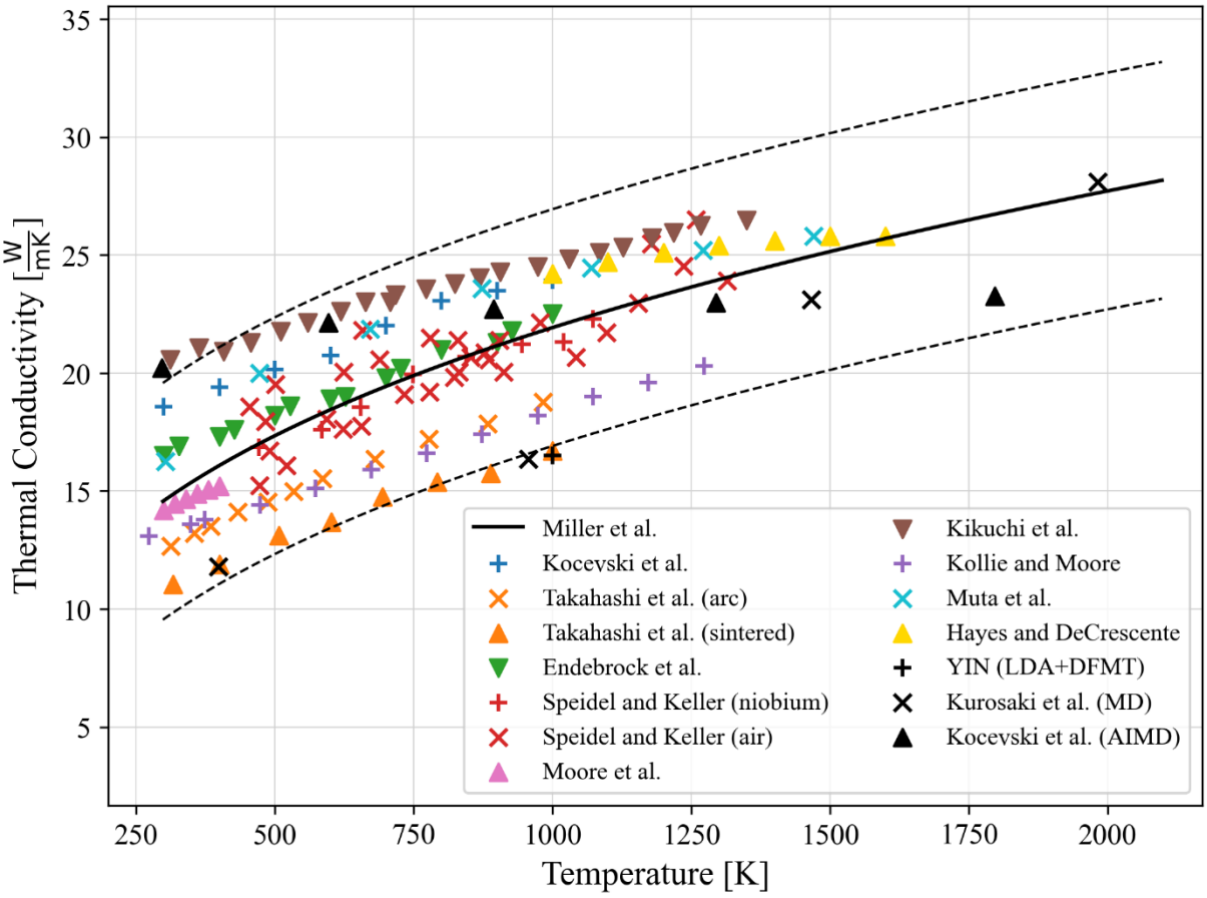

Figure 2.15: Experimental data for thermal conductivity versus temperature for UN corrected to 100% TD [14, 15, 22, 36, 37, 41-46]. ± 2σ is shown in plot with experimental data within ≤ 39 % of trendline.

2.2.2. Specific Heat Capacity

Heat capacity is the measure of amount of energy required to raise the temperature of a material by 1 K [4]. This is given by the following equation:

$$C = \frac{dQ}{dT} \tag{35}$$

where C is heat capacity $\left[\frac{\text{J}}{\text{mol K}}\right]$, dQ is energy required to produce a dT temperature change. One step further, specific heat capacity is the amount of energy required to raise one gram of material by one kelvin. Specific heat capacity is measured in units of $\left[\frac{\text{J}}{\text{g K}}\right]$. As seen in Figure 2.16, UN specific heat capacity increase with temperature. Heat capacity can be determined using two different initial conditions: constant volume and constant pressure. These two conditions can be best described by the Nernst-Einstein equation for heat capacity [6]:

$$C_P = C_V + kT \tag{36}$$

where C_p is the heat capacity for a constant pressure, C_V is the heat capacity for a constant volume, k is an empirically determined constant and T is temperature. Experimentally determining heat capacity for a fixed sample pressure is simpler and therefore heat capacity for a fixed sample volume is most often determined theoretically. Einstein determined that heat capacity will be influenced by the phonons and therefore developed the Einstein theory for heat capacity.

$$C_V = 3R\left(\frac{\theta_E}{T}\right)^2 \frac{\exp\left(\frac{\theta_E}{T}\right)}{[\exp\left(\frac{\theta_E}{T}\right) - 1]^2} \tag{37}$$

where R is universal gas constant, θ_E is Einstein temperature [K], and T is temperature of the material [K].

Experimental data for UN's specific heat with respect to temperature is shown in Figure 2.16. Experimental data for specific heat was collected by eight separate investigators: Muta et al. [14], Speidel and Keller [15], Takahashi et al. [42], Oetting and Leitnaker [49], Affortit [50], Counsell et al. [51], Westrum and Barber [52], Harrington [53], and Cordfunke and Muis [54]. The heat capacities collected during experimentation are those with a fixed pressure.

Utilizing equation 36 and 37 above, Hayes et al. [55] developed a best-fit for heat capacity for UN. To apply these equations to UN, Hayes et al. [55] performed a correlation to empirically determine, k, $3R$, and θ_E. The resulting correlation is valid for temperatures ranging from 298 K to 2900 K:

$$C_p = 51.14\left(\frac{\theta_E}{T}\right)^2 \frac{\exp\left(\frac{\theta_E}{T}\right)}{[\exp\left(\frac{\theta_E}{T}\right) - 1]^2} + 9.941x10^{-3}(T) \tag{38}$$

where C_p is heat capacity of constant volume $\left[\frac{\text{J}}{\text{mol K}}\right]$, θ_E is Einstein temperature of UN [K], and T is the temperature [K]. θ_E was empirically found to be 365.7 K. This correlation is shown in Figure 2.16 for temperatures ranging from 298 K to 2900 K.

As shown in Figure 2.16, two independent computational methods were utilized to determine heat capacity of UN. Kocevski et al. [22] utilized the AIMD method. The calculated data appears to be in good agreement with experimental data. Kurosaki et al. [37] utilize the MD method. The MD method only considers atomic motion without electronic contribution. For this reason, MD calculated heat capacities are less than experimental for the entire temperature range. Kurosaki et al. [37] suggests the difference is due to the electronic heat conduction within UN.

The standard deviation between the experimental data and the correlation line was calculated and is plotted in Figure 2.16. For heat capacity, $5.341 \frac{J}{mol\ K}$ is equal to two standard deviations with the experimental data falling within 14% of the trend line with an average of 3%.

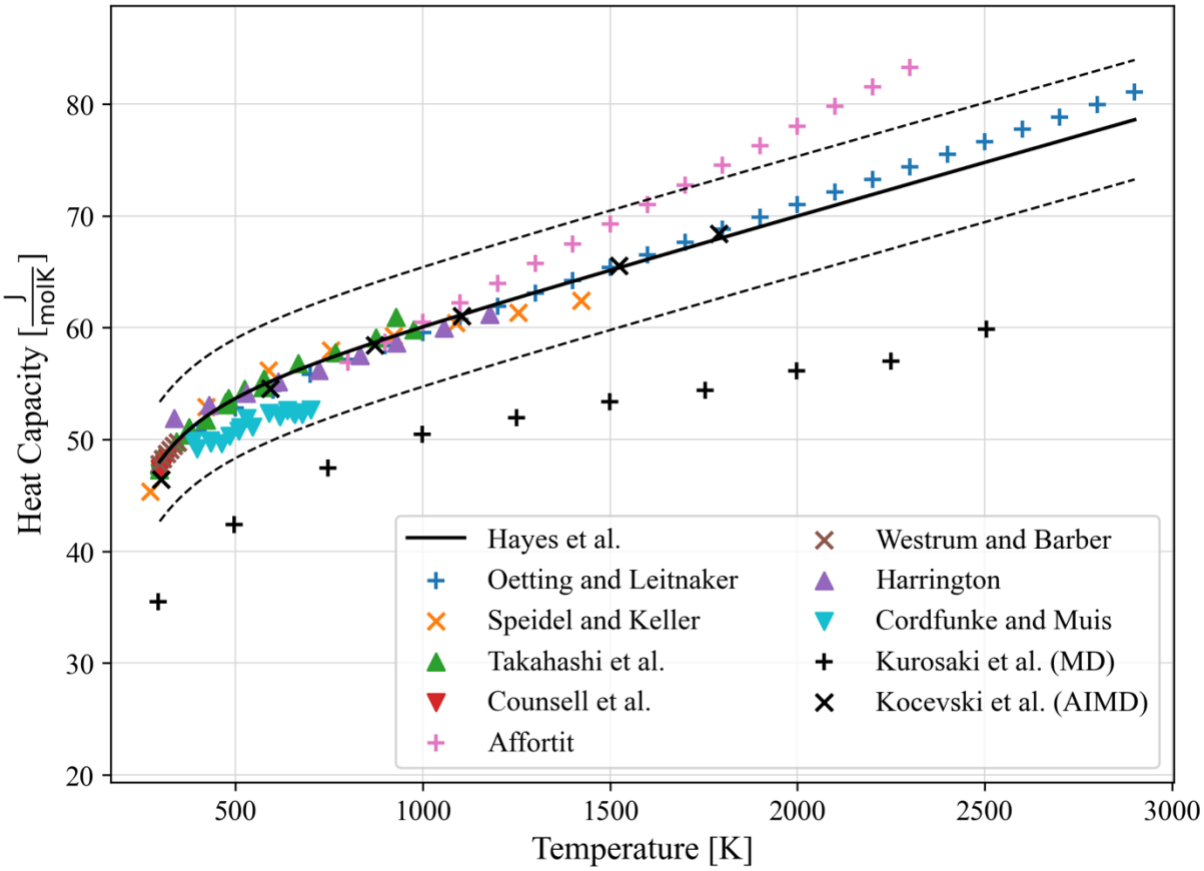

Figure 2.16: Experimental data for heat capacity versus porosity [15, 22, 37, 42, 49-54]. ± 2σ is shown in plot with experimental data within ≤ 14% of trendline.

3. Examining Fuel Under Irradiation

As a nuclear fuel is subjected to irradiation, various micro and macro structural phenomena occur within the material. Various material properties may change, the material will experience permanent dimensional changes, and may become brittle. Overall, these will have a direct impact on the fuel performance and the safe use of the nuclear material. Among the various fuel performance metrics which must be studied, fission gas release and fuel swelling are among the most important. As the nuclear fuel is subject to the fission process, certain fission gases are released, namely Xenon (Xe) and Krypton (Kr). Both gases are either retained within the fuel element or released into the surrounding volume within the cladding. The fission gases retained will begin to build up, causing an increase in fuel swelling, potentially developing a fuel to cladding interaction therefore increasing the stresses in the material. As these gases are released

into the plenum surrounding the fuel, they will impart additional stresses on the cladding, potentially causing ruptures. To ensure fuel safety requirements are met, it is imperative to understand how a nuclear fuel responds to various operating conditions (e.g. power density, temperature, time, etc.) which will allow for a proper safety and fuel performance evaluation. Throughout the following sections, these two phenomena are discussed in detail.

3.1. Fission Products

When a heavy atom, such as uranium, undergoes fission generally producing two fission fragments. The fission fragments will decay into a stable isotope, known as fission products. The fission products that are produced are split into three major categories: solid, volatile, and gaseous. Solid fission products will most often remain in the location of the fission event; however, they may migrate through the material or precipitate out due to thermal gradient of chemical composition of the material. Volatile and gaseous fission products will migrate throughout the lattice structure, depositing in various locations or release from the fuel. Both types of fission products will cause dimensional changes in the fuel, known as fuel swelling. Fission products may also cause changes in fuel properties such as thermal conductivity. Understanding fission product production and behavior is key to understanding the fuel performance of the nuclear materials.

Solid fission products accumulate within the fuel matrix at the fission event takes place. If a large temperature gradient exists within the fuel, solid fission products may move from where the fission event took place. Due to the thermal properties of UN, during normal operations of a reactor, low temperature gradients within the fuel will exist, therefore it is expected that solid fission products will remain in the location they are formed.

Gaseous fission product formation and migration within a fuel matrix is significantly more complex. These fission products will either be retained and coalesce together forming bubbles within the lattice structure. Conversely, the fission gas may release from the fuel into the surrounding plenum. Fission gases that are insoluble within the fuel and that remain a gas in their normal state have the largest and most significant contribution. For this reason, along with the production rate during the fission of uranium, xenon and krypton are the most studied and analyzed gaseous fission products. Much effort has been put forth both experimentally and analytically to understand and best describe how these two fission gases move throughout the fuel matrix.

As described by DeCrescente et al. [19] in a theoretical sense, in the first stage, submicroscopic (less than 100 Å) bubbles form by the accumulation of fission gas atoms, which then migrate to the grain boundaries under the influence of a temperature gradient. The bubbles become bound at the grain boundary due to surface forces. At this point in the process, fuel swelling tends to be low due to the surface force within the submicroscopic bubbles which can

accommodate the increase in pressure from the fission gases. As more bubbles move to the grain boundaries, they begin to coalesce and form long voids. It was observed through electron microscope studies of UN that these long voids tend to go through spheroidization [22]. It is believed this is due to the high surface force within the long void created by the accumulation of gas bubbles. The porosity begins to disconnect, and the fission gases are retained at the boundary, delaying the release of these gases. As these voids continue to grow, pressures are exerted that exceed the creep strength of UN, causing a volumetric fuel swelling. This process then causes partial interconnection of porosity which causes a release of fission gases.

Both the release and retention of fission products is important to the overall fuel performance. As fission gases are released to the plenum, volumetric swelling will be reduced however the surround gas will increase in pressure. This will impart higher stresses on the surrounding cladding, potentially causing failure. For this reason, many experiments have studied the total fission gas release from the fuel during the irradiation of UN. Figure 3.1 shows a combination of the available fission gas release data as a function of burnup. A more detailed breakdown of the data scatter is described within each program section below. In general, it is noted that fission gas release from UN is minimal below ≈3 %FIMA burnup. Observing the CANEL data scatter, the elevated fission gas release corresponds to high-power density and high temperature tests. While observing the data scatter from BR-10, the most likely cause was due to the fabrication process and the material differences.

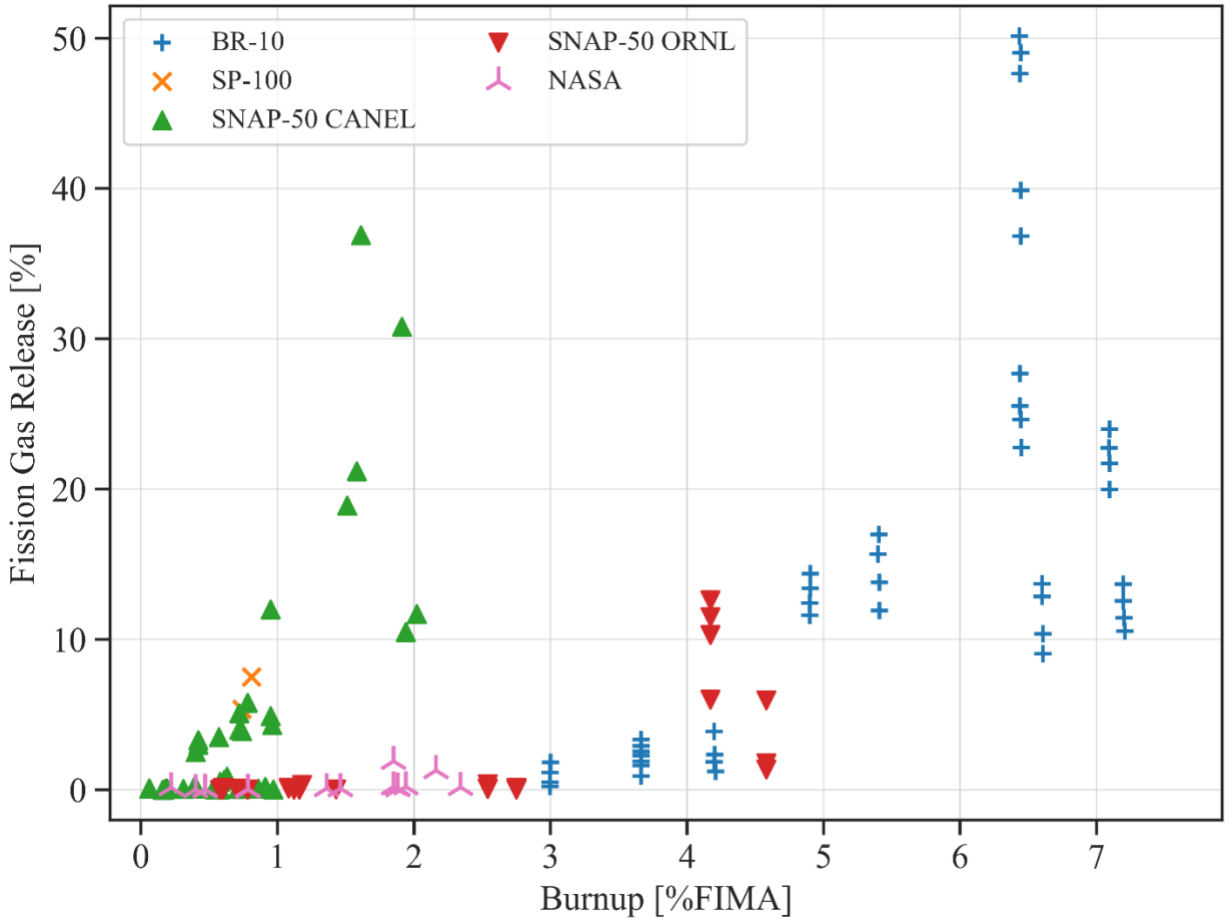

Figure 3.1: Comparison of UN fission gas release experimental data versus burnup for individual fuel pellets [19, 56-64].

3.2. Fuel Swelling

High temperature operations of nuclear fuels have created significant burnup limitations, dominated by the restriction in allowable dimensional changes. The driving factor of the dimensional changes is thought to be fuel expansion caused by a thermal gradient expanding the fission products built up within the fuel matrix, known as fuel swelling. Fuel swelling can be divided into two main mechanisms: inexorable and gaseous swelling. Inexorable swelling is due to solid fission products while gaseous swelling is due to gaseous and volatile fission products that are in gas form at a specified temperature [65].

Solid fission fragments will most often stay within the location of the fission event and not migrate throughout the fuel due to the low temperature gradient within UN. Solid fission product swelling accounts for approximately one percent of the total fuel swelling for every one percent FIMA [66]. While this inexorable swelling rate is an estimation, solid fission product swelling can be expressed by equation 39, and is linearly dependent on burnup, fission yield and the partial volume of the species [66].

$$\left(\frac{\Delta V}{V}\right)_{solid} = BU\left(\sum_{solid\ FP} Y_i \frac{v_i}{v_U} - 1\right) \tag{39}$$

where BU is burnup, Y_i is the fission yield and v_i and v_U are the partial volume of the species and uranium, respectively.

Based on the fission yield, various fission gases will be produced after the decay of their respective fission fragments. For fuel performance, the two main fission gases that dominate the fuel swelling are xenon and krypton. Significant effort has been put forward theoretically, computationally, and experimentally in attempt to understand and establish the mechanisms in which these fission gases are formed, migrate and release from the fuel matrix.

Foreman produced a mathematical expression that predicts the swelling behavior of irradiated uranium at temperatures above ≈1000 K, with the basis that the principal material properties influencing swelling are fuel matrix and cladding creep strength and the fuel matrix surface tension [67]. Foreman [68] started with the viscous creep law at constant temperature and uniaxial tensile stress:

$$\dot{\epsilon} = \frac{\sigma^n}{k} \tag{40}$$

where $\dot{\epsilon}$ is the rate of elongation, σ is the tensile stress, n and k are material constants independent of stress and time. These two constants must be determined experimentally. Once calculated, the swelling of uranium at steady state temperature as a function of irradiation time is found to be:

$$\int_0^x x^{n-1}\left(1 - x^{\frac{1}{n}}\right)^n dx = \frac{3}{2k}\left(\frac{3c}{2n}\right)^n \frac{t^{n+1}}{n+1} \tag{41}$$

where x is the fractional increase in uranium, n and k are material property constants of UN, c is a constant dependent on temperature and rate of fission product production and t is time of irradiation. This relationship was developed under the following assumptions: swelling only takes place by creep, creep strength is unchanged during irradiation, nucleation of fine and uniformly dispersed gas bubbles greater than approximately 0.5 microns diameters occur, and gases entrained in bubbles behave according to the perfect gas law [67]. While this equation provides an initial mathematical assessment of the material, many additional parameters play an important role in the total swelling of the material.

As mentioned above, fission gas formation, migration and release are a complicated process and varies significantly due to reactor conditions. In recent years, many have put significant effort into simulating these processes utilizing various computational methods. Additionally, to help aid the computational programs, many experimental evaluations for fission gas release and

fuel swelling have taken place. Nuclear fuel swelling is a complex phenomenon which theory alone cannot not solve. While the above mathematical expression provides a general understanding of the theory for fuel swelling, it is necessary to perform in pile testing to understand how the fuel will operate in realistic irradiation field.

Figure 3.2 shows the compilation of the volumetric fuel swelling experimental data with respect to uranium burnup. Additionally, Figure 3.3 shows the same data with respect to temperature and power density. Each test series is described in detail in the following sections. By observing irradiation data in both figures, various impactful fuel swelling characteristics can be investigated. The first is known as “break-away” swelling, defined as the continuous rapid increase in volume. The second is known as “saturation of swelling”, defined as a rapid rise in volume followed by no additional increase. Both characteristics have a direct impact on fuel performance and safety. Generally, a known and well defined approximately linear increase in fuel swelling is desired. Understanding break-away swelling will allow for setting operational limitations on reactor designs. Additionally, areas of specific interest exist in the high temperature - low burnup region where the swelling is significant and relatively sporadic.

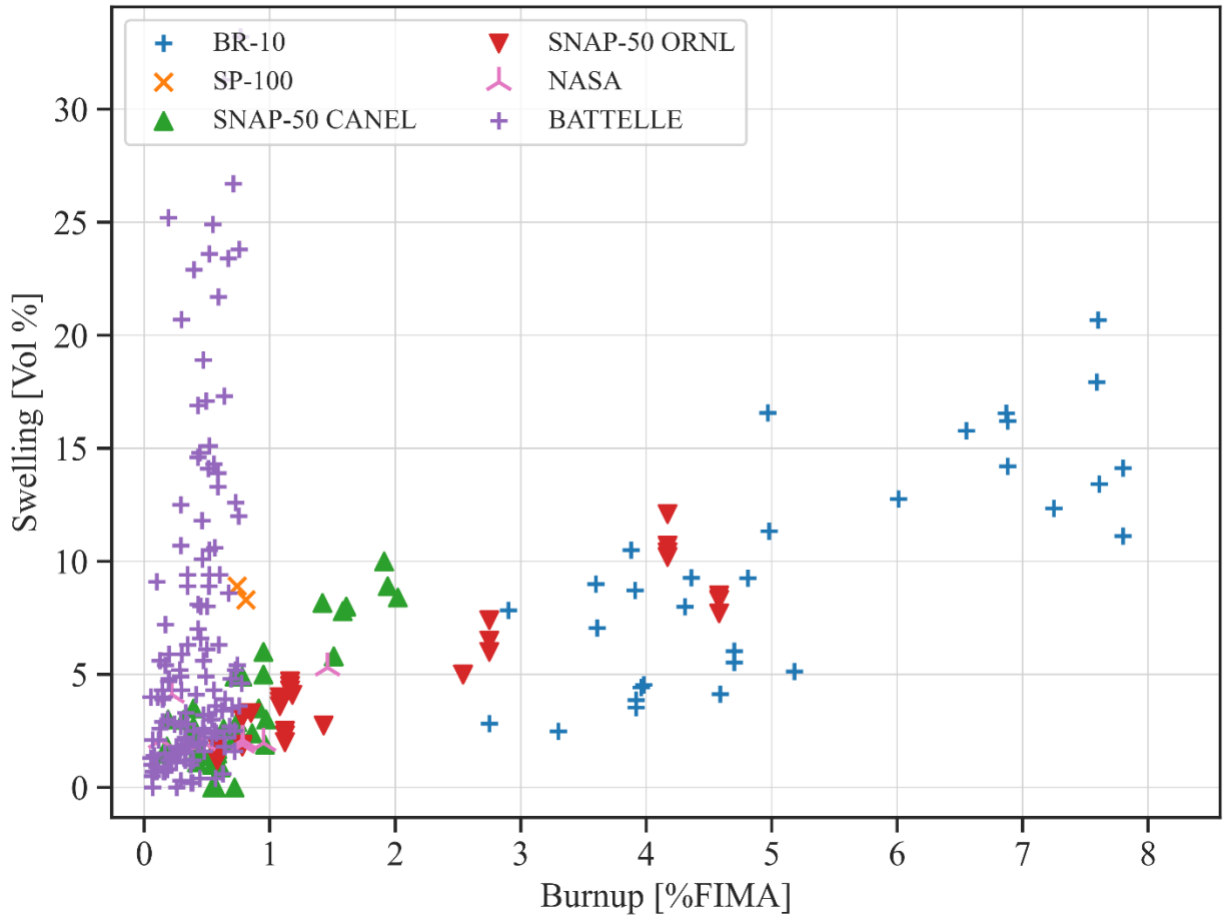

Figure 3.2: Comparison of total UN volumetric fuel swelling experimental data versus burnup for individual pellets [19, 56-64, 69-74].

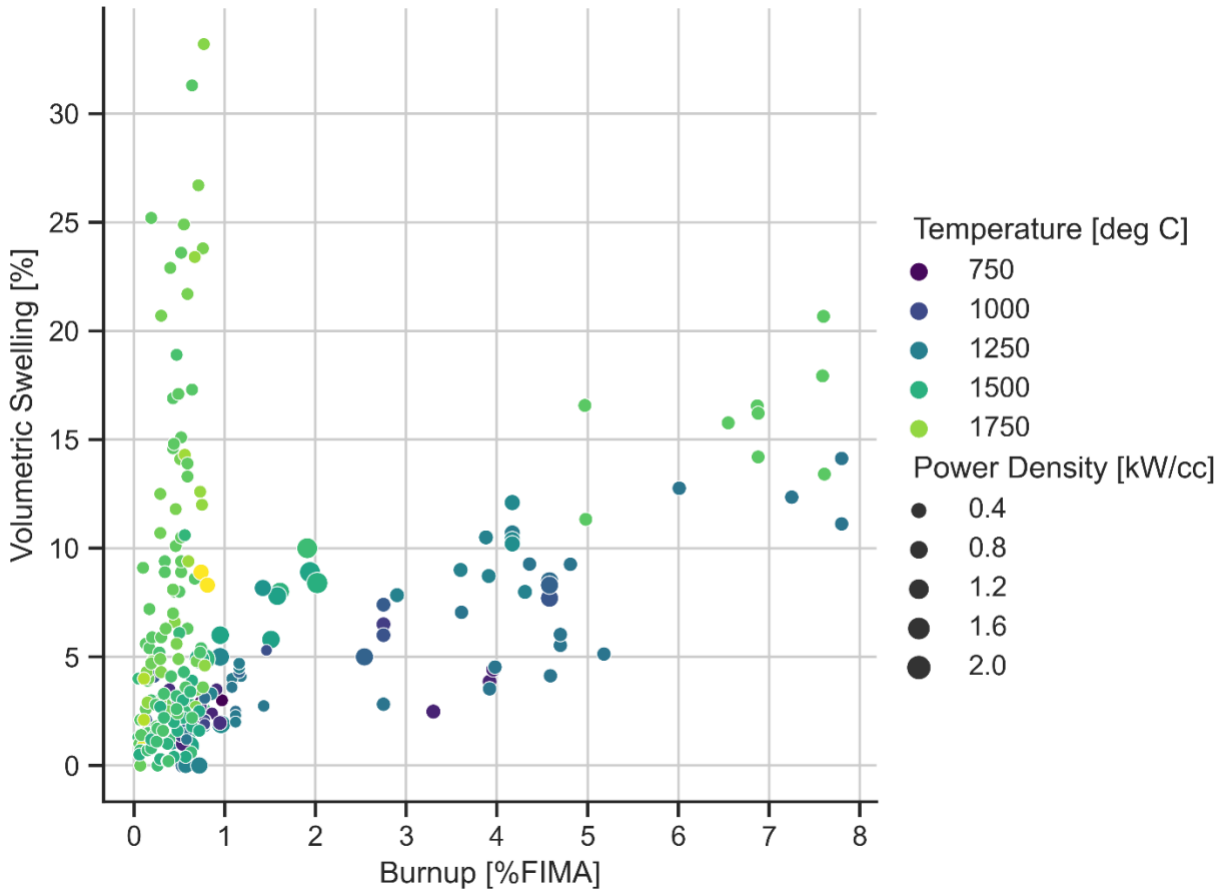

Figure 3.3: Comparison of total UN volumetric fuel swelling experimental data versus burnup with respect to temperature and power density for individual pellets [19, 56-64, 69-74].

As an initial attempt to develop a UN fuel swelling correlation, Ross et al. [75] analyzed data from the SNAP-50 program and provided a best fit utilizing key variables such as burnup, temperature and porosity. The following is the correlation:

$$\frac{\Delta V}{V}\,(\%) = 4.7 \times 10^{-11}\, T_{av}^{3.12}\, Bu^{0.83}\, \rho^{0.5} \tag{42}$$

where T_{av} is the volume average fuel temperature in K, Bu is the fuel burnup (%FIMA), and ρ is the as-fabricated fuel density (% TD). It is noted that this correlation was within ± 60% of the SNAP-50 data at burnups less than 1.12 %FIMA however it was ± 25% of the SNAP-50 burnup data at burnups more than 1.12 %FIMA. Ross et al. noted that there were many uncertainties that influenced the overall error in the correlation curve. Fuel pin dimensions were inconsistent, there was significant scatter in both fuel swelling (± 300%) and fission gas release (± 200%) for fuel pins irradiated at the same design and under similar conditions, along with variations in the reported fuel volume temperatures. As fuel temperature is a dominate parameter in the developed correlation, Ross et al. developed a consistent methodology to calculate the volume average temperature based on fuel cladding temperature, and a consistent modeling of the gap

conductance. Overall, the gap conductance was calculated based off diametral swelling, reported fission gas swelling and radial temperature distribution. While this correlation provides a generalized UN fuel swelling for high temperature applications, this is a geometric dependent method and further studies are needed to further generalize UN fuel behavior to predict more operational environments.

3.3. Summary of UN Irradiation Programs

The space race began in 1957 when Sputnik was launched, igniting the desire to enable deep space and interplanetary technology into space. This interest was accelerated through the threats of the Cold War, accelerating the overall research and design across the world. During this time, the need for a reliable and efficient means of power for spacecraft was apparent. Various concepts and designs were brought forward, most relying upon the new age technology of nuclear power. These concepts all understood the need of a nuclear fuel able to withstand the high temperature environment that may exist within a small compact microreactor. For this reason, different organizations began to fabricate and test fuels, one of particular interest was UN. From the 1960's until the early 2000's, UN irradiation testing took place providing a significant step forward in understanding the influence irradiation has on its properties and performance.

The most notable programs were: UN testing performed at the Bystry Reactor 10 (BR-10); Systems for Nuclear Auxiliary Power 50 (SNAP-50) program led by the research team at Connecticut Advanced Nuclear Engineering Laboratory (CANEL) and later Oakridge National Laboratory (ORNL); the Advanced Space Power Reactor Concept led by the research team at National Aeronautics and Space Administration (NASA) Lewis research center; and the SP-100 program led by Los Alamos National Lab (LANL). Throughout the following sections, the above programs are discussed in detail focusing on two main fuel performance properties: total volumetric fuel swelling and fission gas release with respect to the total uranium atomic burnup. Additional information such as fuel failures, temperature effects, chemical composition, and swelling correlations are added within the following sections as the information is available.

3.3.1. BR-10

Bystry Reactor-10 (BR-10) is a sodium cooled, fast test reactor which operated in Russia from 1959 to 2002. UN was experimentally tested in the fourth and fifth loadings, occurring between the years of 1983 and 2002. In these loading, fuel pins were referred to as driver subassemblies (SA). Additionally, multiple experimental subassemblies were irradiated in BR-10. A total of 1250 driver SA fuel pins (660 in loading IV and 590 in loa ding V) were irradiated at a maximum fuel temperature of 1175 K, with a density ranging from 85-94% TD [76]. Maximum fuel burnup of the first core loading was ≈8 %FIMA while the second was ≈8.8 %FIMA [76]. Table III provides a summary of BR-10 and core loadings.

Table III. BR-10 reactor and fuel pin characteristics [76].

Parameter	IV Loading	V Loading
Reactor Power	8 MW	
Linear Heat Rate	45 KW/m	
Fuel Temp	1175 K	
Cladding	Boron Micro-alloyed Austenitic Steel	
Fill Gas	Helium	
Fuel Pellet Diameter	0.74 cm	
Fuel Stack Height	40 cm	
Max Burnup	8.0 %FIMA	8.8 %FIMA
Pellet Density	12.0 g/cm^3 (83.79% TD)	13.4 g/cm^3 (93.56 %TD)

Post irradiation examination (PIE) of three experimental (UN-2, K-1 and K-3) and eight driver SAs (N-009, N-017, N-019, N-021, N-094, N-095, N-118, AB-60) took place at the Institute for Physics and Power Engineering (IPPE) hot lab. UN-2 was divided into two separate compositions, one with a helium bonded fuel and the other with a sodium bonded fuel. K-1 and K-3 are both helium bonded however the fabrication processes varied. K-1 was fabricated by hydrogenation-nitriding of a metallic uranium while K-3 and the driver SAs were produced by a carbothermic reduction of uranium dioxide [76]. Two studies were performed on the group of subassemblies: fuel swelling and fission gas release as a function of fuel burnup. A summary of these analyses is provided below, and the fuel assembly irradiation conditions are shown in Table IV.

Table IV: Conditions of Irradiation of SA with UN [58, 59, 76].

Subassembly	Time of Irradiation	Maximum Burnup [%FIMA]	Pellet Density (% TD)	Maximum Fuel Temperature [K]
UN-2	883 days (22.06.76 – 22.11.78)	4.3	91-96	1113 (sodium) 1535 (gas)
K-3	1834 days (05.11.74−13.11.79)	7.6	91.55	1910
K-1	2129 days (04.01.74−03.11.79)	7.6	89.5	
N-017	884 days (12.05.83−12.10.85)	3.43	89.4-93.6	1475
N-019	663 days (12.05.83−03.02.87)	4.8		
N-009	2291 days (24.05.83−31.08.89)	5.7		
N-118*	2363 days (12.05.83−30.10.89)	5.8		
N-095**	1778 days (10.05.83−22.03.88)	6.3		
N-021**	2282 days (12.05.83 – 10.08.89)	7.6		
N-094**	2265 days (10.05.83 – 22.07.89)	8.2		
AB-60**	3349 days (24.07.90 – 24.09.99)	8.4		

* Experimental SA
** Drive SA

Fuel swelling as a function of burnup is plotted in Figure 3.4 and shown in Table VI. For comparison, Figure 3.4 shows data for the central, upper and lower fuel pellet in a non-specific driver subassembly, as well the three experimental subassemblies. As described by Porollo et al. [58], the central driver pellet was irradiated with a fuel temperature of ≈1473 K and has a swelling rate of 1.65% per 1 %FIMA burnup. The upper and lower pellets were irradiated with an average fuel temperature of ≈1100 K and has a swelling rate of 1.35% for 1 %FIMA burnup. The gas bonded UN-2 experimental subassembly was irradiated with a fuel temperature of ≈1530 K while the sodium bonded UN-2 subassembly was irradiated with a fuel temperature of ≈1100 K. The gas bonded subassembly swelling rate is two times that of the sodium bonded UN-2 subassembly. K-1 and K-3 experimental subassemblies were irradiated with the same fuel temperature of ≈1670 K. K-1 had a swelling rate of 2% per 1 %FIMA burnup while K-3 had a swelling rate of 2.6% per 1 %FIMA despite having the same fuel temperature. It was concluded

that this was due to the differing fabrication processes [59]. UN fuel temperature directly impacts the swelling rate and total swelling of UN with respect to fuel burnup.

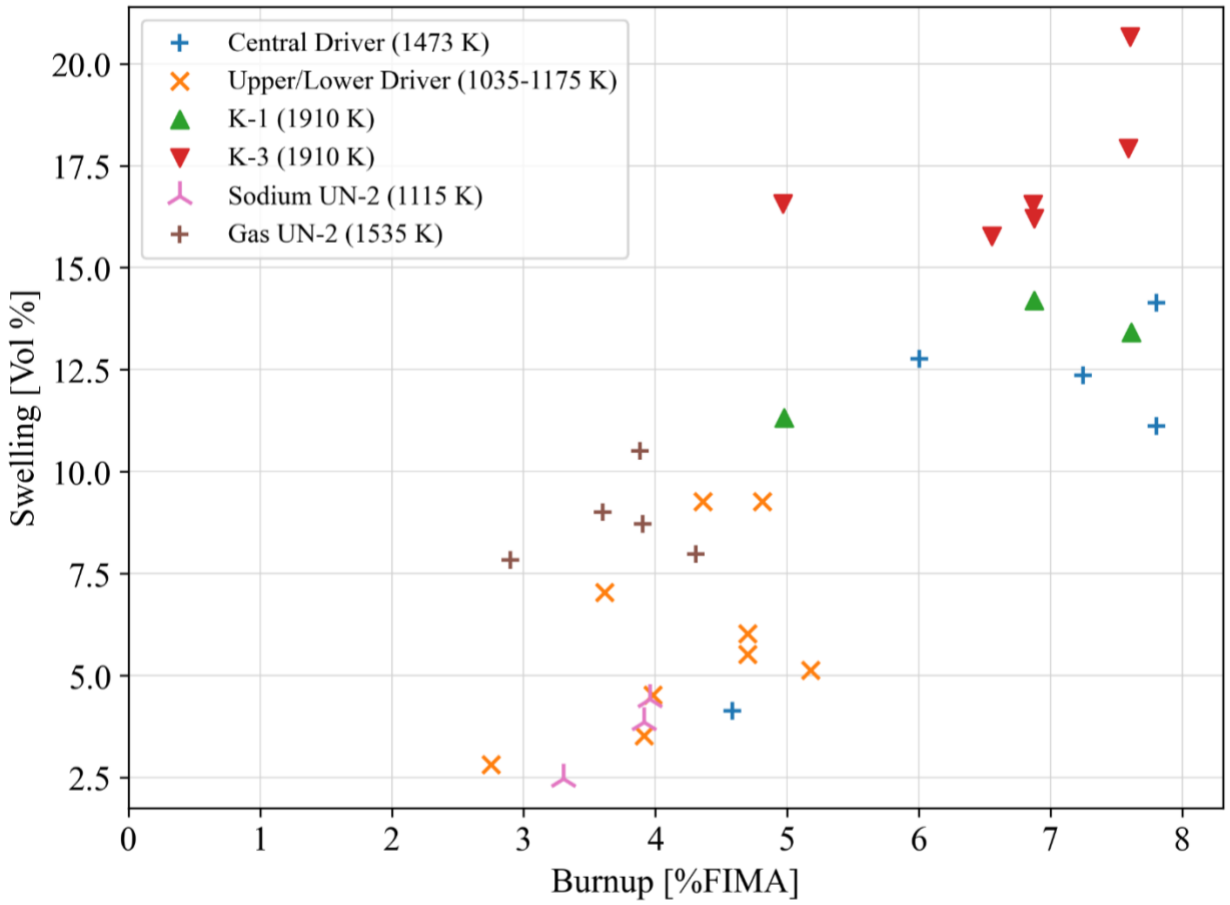

Figure 3.4: Volumetric swelling versus burnup for driver and experimental fuel assemblies [58, 59].

To confirm the temperature dependence on UN swelling rate, experimental data was collected for fuel swelling rate as a function of temperature [59]. This study provided swelling rate plotted over the range of irradiation temperatures from 993 K to 1953 K as well as a best-fit correlation. The data was converted to Kelvin and a new correlation is given as:

$$\frac{Swelling}{Burnup}\left(\frac{S}{B}\right) = 6.95 - \ 1.1x10^{-2}T + 5.25 \times 10^{-6}T^2 \tag{43}$$

where *S/B* is swelling per 1 %FIMA burnup and *T* is fuel temperature [K]. As seen in Figure 3.5, swelling rate increases as fuel temperature increases. The above correlation is plotted in Figure 3.5.

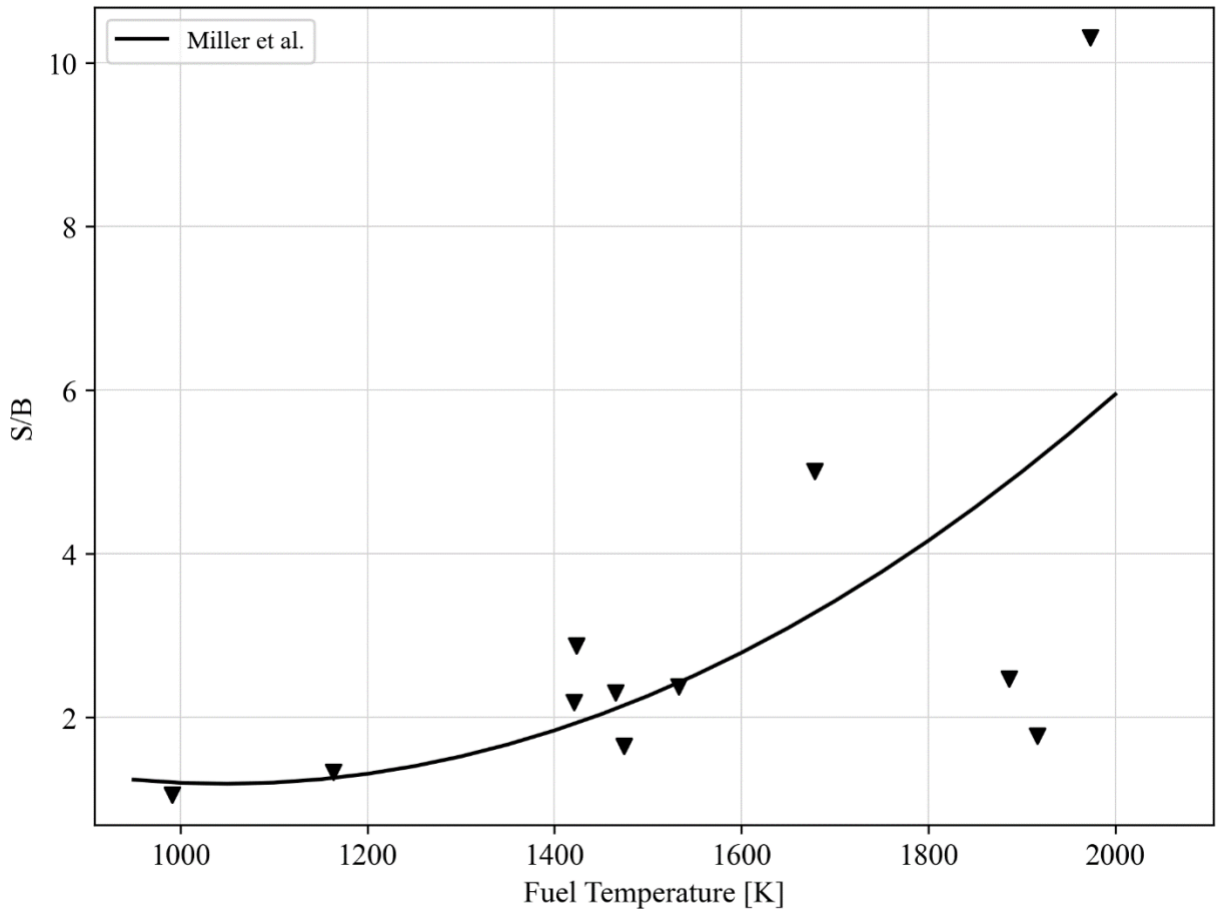

Figure 3.5: Swelling rate per 1 %FIMA burnup for various UN fuel temperatures [59].

The second study measured the change in the gas plenum volume as a function of burnup. This was performed by puncturing a hole in the cladding and measuring the pressure release with an accuracy of ± 1.5% and gas composition using radiochromotography with an accuracy of ± 8% [59]. The fission products of interest were krypton and xenon. The total fission product percentage of the gas plenum as a function of %FIMA burnup for the subassemblies is plotted in Figure 3.6 and shown in Table VII.

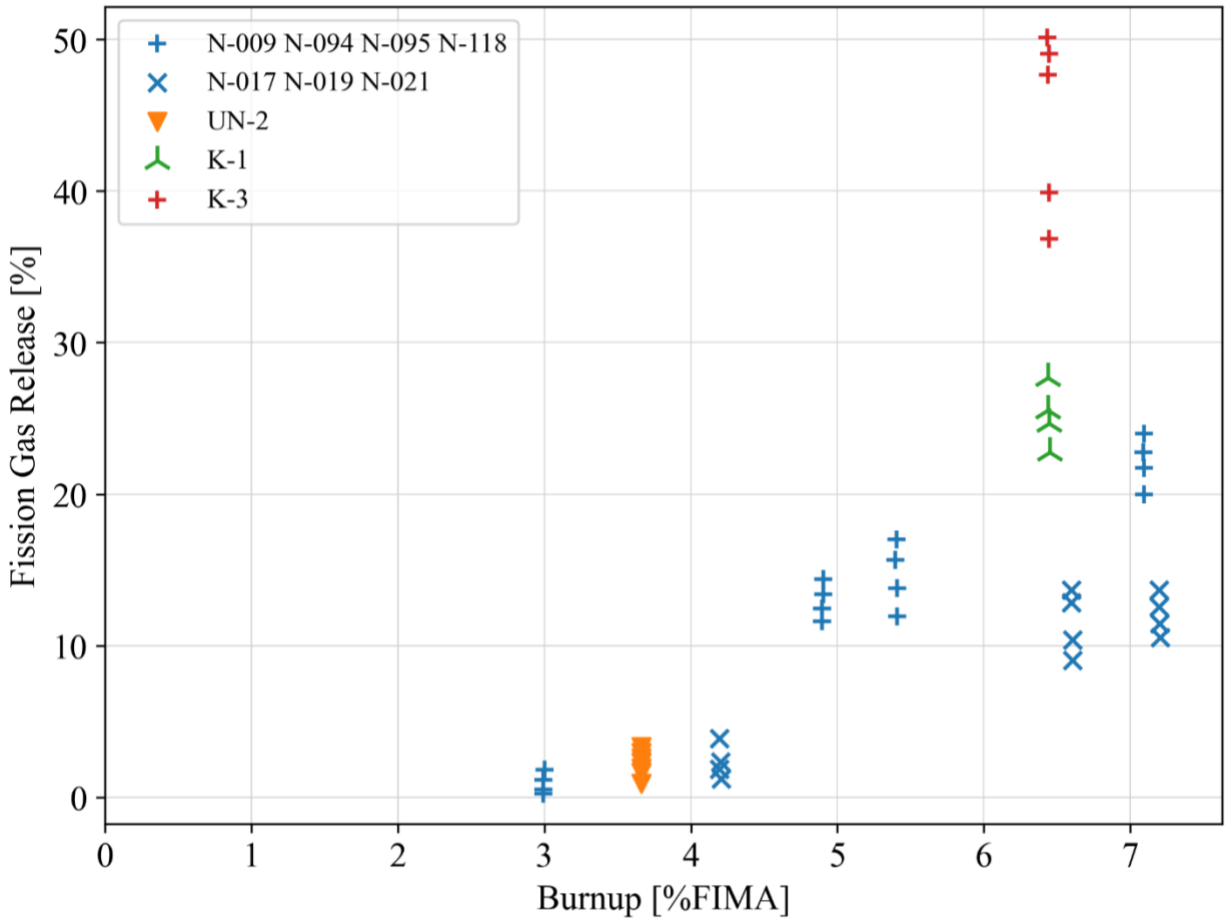

Figure 3.6: Fission gas release as a percentage of total gas plenum volume versus burnup [58, 59].

Observing Figure 3.6, it is seen that fission product release for UN in BR-10 is negligible for a burnup less than 3 %FIMA. For the driver subassemblies, there is slight variation in the total fission product as burnup increases. Every driver subassembly was irradiated in the same conditions however the fuel composition varied slightly as seen in Table V. Observing K-1 and K-3, K-3 yielded nearly twice as much fission products as K-1. K-1 and K-3 were irradiated at the same temperature therefore, it was concluded that this increase was most likely due to the fabrication process differences [54]. The final observation is that the fission product release for K-3 which was irradiated at an average fuel temperature of ≈1670 K, was approximately 2-3 times larger than the fission product release of the driver subassemblies which were irradiated at an average fuel temperature of ≈1290 K. In general, higher irradiation temperatures yields a higher release of fission products.

It is reported that two cases of fuel failures occurred in core loading IV and 24 cases occurred in core loading V [76]. In core loading IV, one failure occurred at approximately 5.4 %FIMA burnup while the second occurred at approximately 7.1 %FIMA. These were determined to be at maximum burnup for their fuel pins. In core loading V, one failure occurred at approximately 6.3

%FIMA burnup while the remaining 23 occurred at >8 %FIMA [59]. It was determined that the most probable reason for this was due to fuel-cladding mechanical interaction (FCMI) [76]. Additionally, all fuel rods tested in the BR-10 contained impurities greater than the standard allowable limit and are shown in Table V. Oxygen and carbon limits are less than 0.15 wt.% when the actual levels were between 0.2 and 0.94 wt.% for oxygen and 0.05 and 0.5 wt.% for carbon.

Table V. BR-10 fuel pin chemical composition and specifications [59].

	Specification (wt. %)	Driver SA	K-3 SA*
Uranium	≥ 93.5	93.5 – 94.3	94.4 – 94.5
Nitrogen	5.05 ± 0.5	4.5 – 5.2	4.7 – 4.8
Carbon	< 0.15	0.05 – 0.5	0.3
Oxygen	≤ 0.15	0.2 – 0.94	0.4 – 0.6
Density	≥ 11.5	12.8 – 13.4	12.1 ± .1

*Experimental SA

Overall, there is a clear correlation between fuel swelling and burnup rate which effected by the temperature at which the irradiation testing took place. Additionally, fission gas release is affected by irradiation temperature and fuel composition. Fabrication of UN and chemical composition was theorized to be a major impact on the fuel performance of UN.

Table VI. BR-10 fuel swelling data for individual fuel pellets (Burnup [%FIMA], Fuel Swelling [%]) [58, 59].

Central Driver		**Upper and Lower Driver**		**K-1**		**K-3**		**UN-2 Sodium**		**UN-2 Gas**	
Burnup	Swelling	Burnup	Swelling	Burnup	Swelling	Burnup	Swelling	Burnup	Swelling	Burnup	Swelling
4.59	4.13	2.75	2.82	4.98	11.33	4.97	16.57	3.92	3.86	4.31	7.99
6.01	12.76	3.92	3.53	6.88	14.20	6.55	15.77	3.30	2.48	3.91	8.72
7.25	12.35	3.98	4.53	7.61	13.41	6.87	16.55	3.96	4.42	3.88	10.50
7.80	11.12	4.70	5.53			6.88	16.21			3.60	9.00
7.80	14.13	4.70	6.03			7.59	17.93			2.90	7.84
		5.18	5.13			7.60	20.67				
		4.81	9.26								
		4.36	9.27								
		3.61	7.05								

Table VII. BR-10 fission gas data for individual fuel pellets (Burnup [%FIMA] Fission Gas Release [%]) [58, 59].

N-009,118,095,094		**N-017,019,021**		**K-1**		**K-3**		**UN-2**	
Burnup	Fission Gas	Burnup	Fission Gas	Burnup	Fission Gas	Burnup	Fission Gas	Burnup	Fission Gas
3.00	1.84	4.21	1.24	6.45	22.78	6.43	50.15	3.66	0.91
2.99	1.14	4.20	1.86	6.44	24.65	6.44	49.04	3.66	1.61
2.99	0.52	4.20	2.35	6.44	25.55	6.44	47.65	3.66	1.88
2.99	0.24	4.20	3.87	6.44	27.70	6.44	39.89	3.66	2.30
4.90	14.38	6.61	9.06			6.44	36.84	3.66	3.34
4.90	13.41	6.61	10.37					3.66	2.92
4.90	12.44	6.60	12.87					3.66	2.58
4.90	11.61	6.60	13.70						
5.40	17.00	7.21	10.56						
5.40	15.68	7.20	11.46						
5.41	13.81	7.19	12.57						
5.41	11.94	7.19	13.68						
7.09	24.00								
7.09	22.76								
7.09	21.72								
7.09	19.99								

3.3.2. SNAP-50

In the 1960's, a tri-agency agreement between the Atomic Energy Commission (AEC) (now known as the Department of Energy (DOE)), NASA, and Air Force was made in hopes to develop a robust power supply for future spacecraft. The joint effort decided on a reference design able to provide a total output of 300 kW electric which could be upgraded to 1000 kW electric [77]. Thus, the Systems for Nuclear Auxiliary Power (SNAP-50) was erected [78-80]. Two reference reactor designs were initially suggested, utilizing Uranium Carbide (UC) and UN inside a lithium-cooled fast reactor. The first design was set to achieve 8 MW thermal for 10,000 operational hours, while maintaining volumetric fuel swelling below 4% and fission gas release below 10%. After initial irradiation testing, it was evident that UN was superior to UN however both were not able to withstand the conditions initially assumed. Therefore, design power level and burnup limitations, namely, fuel swelling and fission gas release, were reduced [63]. The final design parameters are shown in Table VIII [64].

Table VIII. SNAP-50 Reference Design Parameters [64].

Thermal Power Level [MW]	2
Maximum Fuel Temperature [K]	1533
Maximum Fuel Pin Power Density [W/cm^3]	400
Maximum Fuel Burnup [%FIMA]	1.5
Maximum Fission-Gas Release [%]	20
Maximum Diametrical Fuel Swelling [%]	2
Maximum Volumetric Fuel Swelling [%]	8

Pratt and Whitney Aircraft was chosen as the lead industry partner for the initial SNAP-50 testing due to their recent success with testing UN under the Aircraft Nuclear Propulsion (ANP) program as well as the recent completion of the Connecticut Advanced Nuclear Engineering Laboratory (CANEL) in 1957 [19]. By 1965, a significant portion of SNAP-50 component design, materials, fuels, and subcomponent development phase had been complete at CANEL. By the end of 1965, the country's need for a program of this specificity was no longer present therefore the research conducted at CANEL was phased out. Instead, the program objectives were transferred to Lawrence Radiation Laboratory (LRL) and Oak Ridge National Laboratory (ORNL). LRL developed reference designs to tackle areas of concern that arose from the SNAP-50 testing at CANEL. ORNL assumed the irradiation testing of UN at the Materials Testing Reactor (MTR) [64]. As budgets continued to lower, NASA took over the project where they included SNAP-50 design research into their new Advanced Power Reactor (APR). APR testing program will be discussed in detail in the following section. The remainder of this section focuses on the irradiation test results of UN by CANEL and ORNL.

Two sets of irradiation testing were conducted under the SNAP-50 program: one originally taking place at CANEL [19, 63] and another at ORNL [64]. CANEL tests were broken down

into high power density (≈1 to 2 kW/cm^3) and low power density (≈0.4 to 0.8 kW/cm^3) while ORNL tests were predominantly low power density (≈0.3 to 0.7 kW/cm^3) with three tests at a higher power density (≈1.0 – 1.4 kW/cm^3). For most of the testing series (except for the 630 series), the fuel pellet capsules contained three right-circular cylinders, with a diameter of approximately 0.478 cm and varying lengths. The specimens had densities varying from 90% to 97% TD and enrichments from 10% up to 93% U-235. The fuel capsules were clad with Nb – 1%Zr or PWC-11 (Nb – 1%Zr – 0.1%C), typically containing a tungsten foil or vapor-deposited tungsten barrier and backfilled and sealed with helium. A breakdown of the various test series is detailed in Tables IX and X for CANEL and XIII for ORNL [64].

The start of the SNAP-50 UN testing began at CANEL, investigating the initial design criteria. The main fuel parameters for this reactor design were a maximum fuel centerline temperature of 1645 K, power density of 1.5 kW/cm^3, and a maximum burnup of 4.3 %FIMA [63]. This design limited the diametral swelling, volumetric swelling and fission gas release to the plenum to be less than 2%, 8% and 20% respectively. As shown in Table XI for capsule 231 (bolded and highlighted in grey), it was very quickly determined that fuel swelling and fission gas release would be exceeded within the desired lifetime of the reactor (10,000 hours). In fact, the fission gas release and fuel swelling limits were exceeded after approximately 2750 hours of operation [64]. Under this initial design, UN was critically limited. For this reason, the second iteration of the design was developed, as mentioned in Table VIII above. The power density was reduced to 0.4 kW/cm^3, maximum centerline fuel temperature was reduced to 1533 K, maximum burnup was reduced to 1.5 %FIMA, and the maximum fission product released, and volumetric swelling was increased to 20 % and 8%, respectively. The available irradiation data is shown in Tables XI and XII for high and low power density and is also graphically shown in Figures 3.7 through 3.9. Only fuel pellets with an enrichment of 10% is shown in the figures to minimize potential irradiation variations. No corrections were made to the data to compensate for material, temperature, or fission rate variations [19].

Observing Figure 3.7 through 3.9, aside from the data scatter in the high-power density results, an approximately linear increase is observed. DeCrescente et al. [19] concluded that the data scatter within each series was most likely due to the slight variations in flux and temperatures during the tests. The nominal fuel temperatures experienced during the testing at CANEL was 1375 K, 1575 K and 1775 K. As shown in Figures 3.7 and 3.9, volumetric swelling, diametral increase and fission gas release were small at temperatures less than 1575 K (low power-density). As temperatures increase, fission gas and fuel swelling begin to increase but do not become excessive and no “break-away” swelling is observed. Additionally, post irradiation examination indicated no major fuel pin or capsule failures except those in the 630 series of testing. No explanation was provided for the failures; however, it is noted that the specimen was a single fuel slug instead of three smaller pellets, two of which contained a 0.1397 cm hole at the center, and the fuel column was approximately three times in length. Additionally, it is expected

that fuel-cladding frictional forces will increase as the fuel length increases due to the increase in surface area contact.

When comparing data from the two power-density conditions, it is evident that the increase in temperature plays a direct role in fuel swelling and gas release. As the irradiation temperature increases, the total volumetric fuel swelling increases. Additionally, DeCrescente et al. [19] concluded that swelling rates are higher in the high-power density conditions due to the higher gas migration rates associated with the higher temperatures and temperature gradients. Additionally, there is an elevated gas movement due to the lower creep strength associated with the higher temperature.

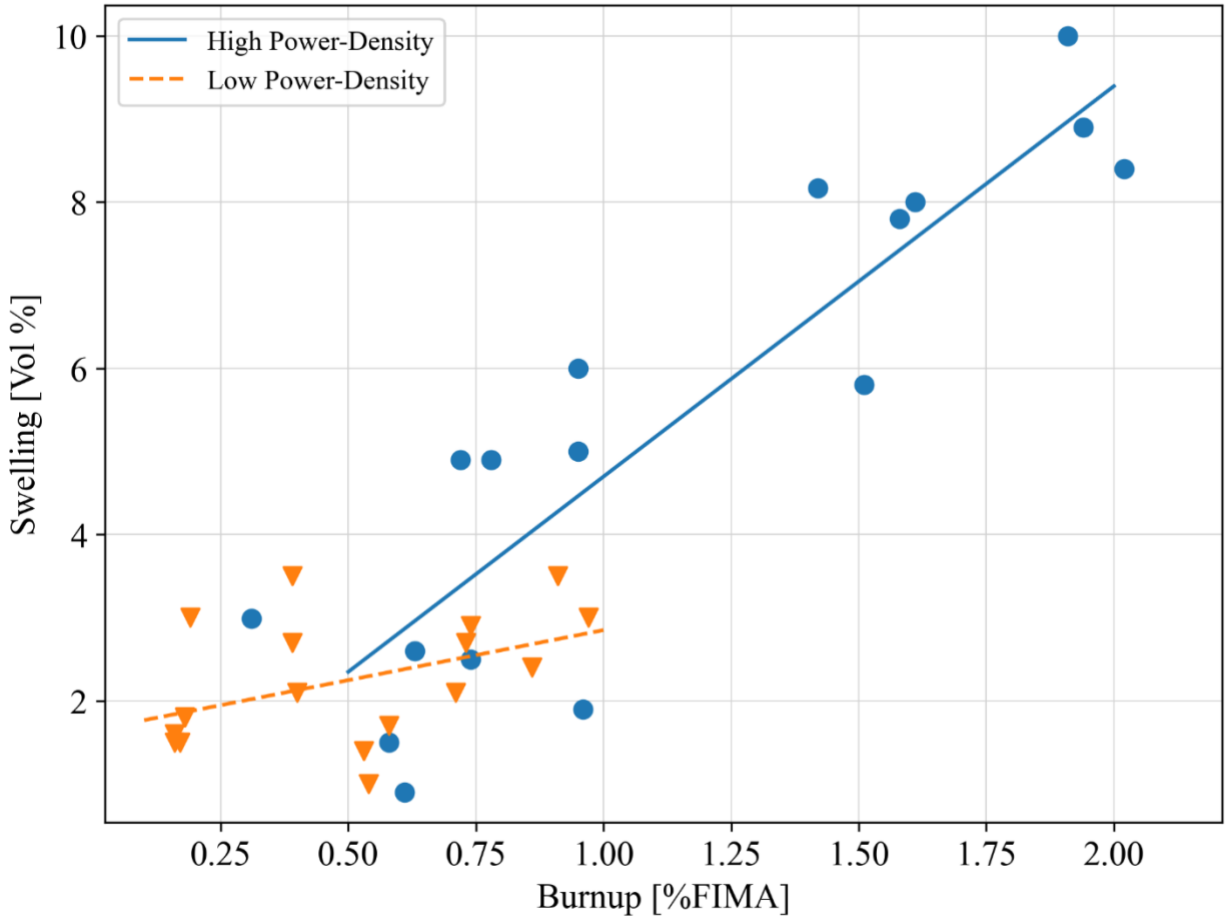

Figure 3.7: Volumetric fuel swelling versus burnup for SNAP-50 testing performed at CANEL [19, 63].

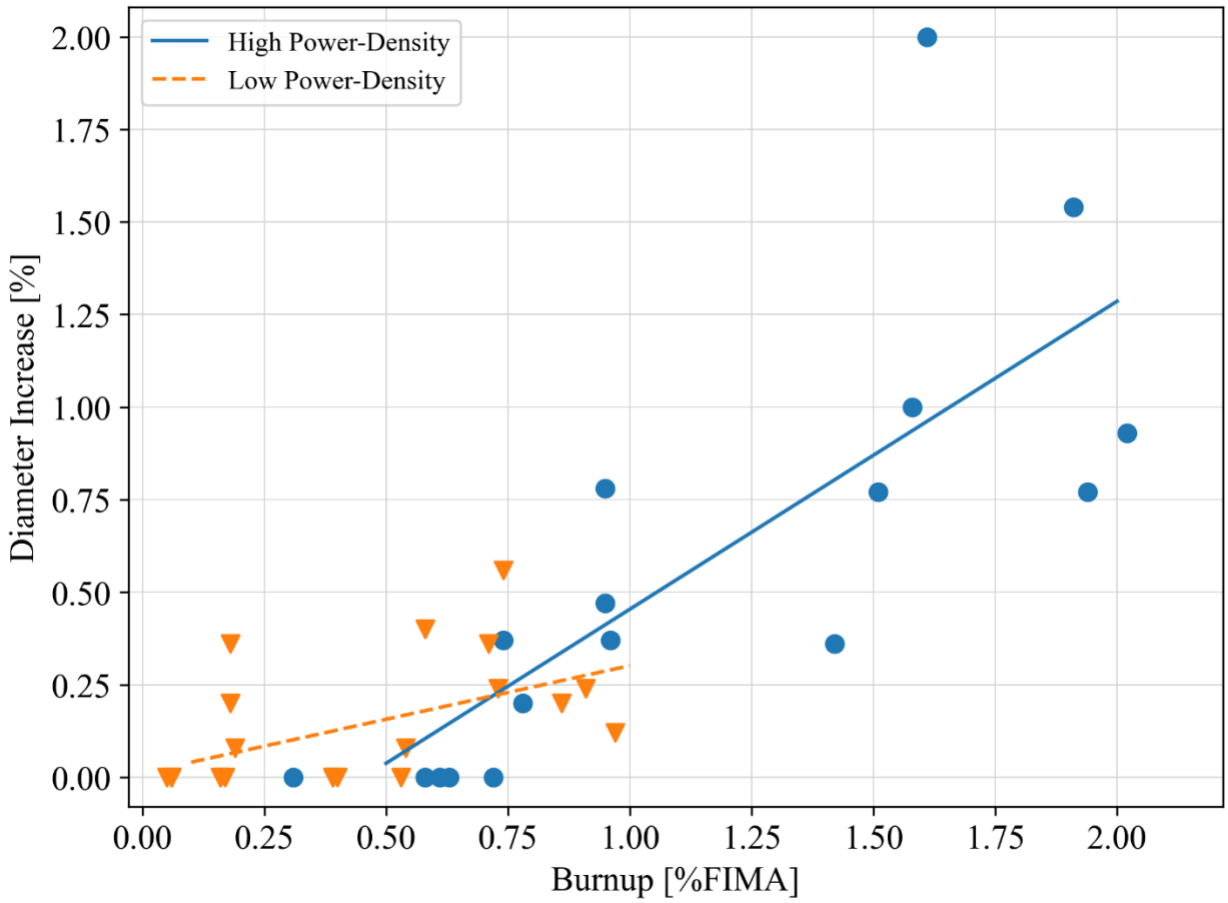

Figure 3.8: Diameter increase versus burnup for SNAP-50 testing performed at CANEL [19, 63].

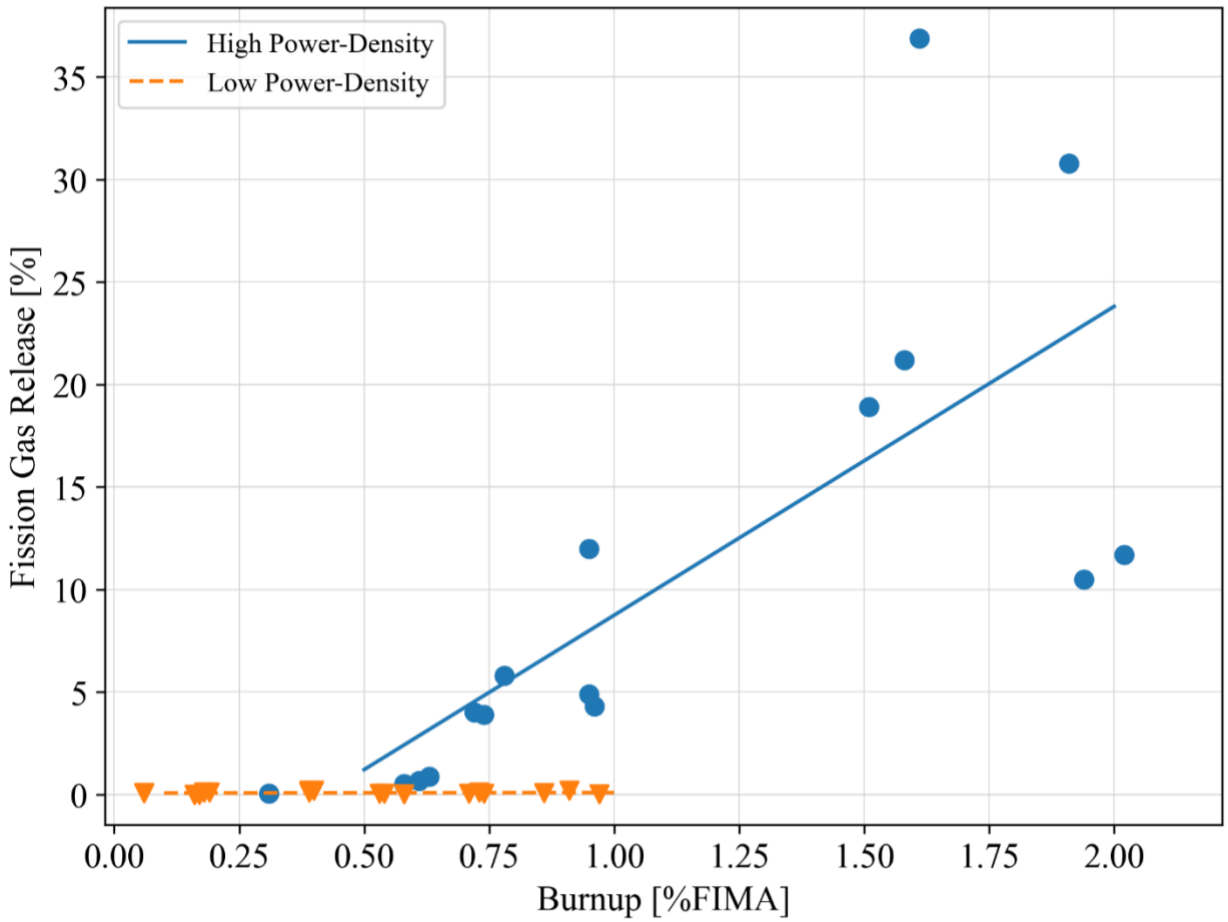

Figure 3.9: Fission gas release versus burnup for SNAP-50 testing performed at CANEL [19, 63].

After the cancelation of the CANEL irradiation testing program, operations were transferred to ORNL for testing at the Material Testing Reactor (MTR). ORNL focused on the performance of UN at irradiation temperatures ranging from 1375 K to 1575 K, a higher burnup up to 4.6 %FIMA and longer irradiation times up to 12,000 hours [64]. When testing was transferred to ORNL, six capsules were undergoing irradiation and four capsules had been removed ready for examination, while five others were constructed and ready to be placed in MTR. The capsules were of similar dimensions as those from CANEL and shown in Table XIII, however there were three types of capsules instead of two containing one, three or four fuel pins. One version contained one fuel pin with a fuel length of 8.382 cm with a total fuel pin column length of 12.04 cm. The second capsule design contained either three or four fuel pins, with each fuel length of 1.65 cm and a total fuel pin column of 4 cm. Additionally, all fuel specimens were clad with PWC-11. The ORNL testing program followed the same design conditions outlined in Table VIII above except for in four of the untested capsules. These four capsules were irradiated in similar temperature conditions however they were modified to achieve higher power densities and therefore higher burnup. Irradiation conditions and results are shown in Table XIV and in Figures 3.10 through 3.12.

Successful testing of 15 UN fuel capsules took place during the ORNL testing program. Of the 15 capsules tested, 8 achieved the desired irradiation time of 10,000 hours with one achieving 12,000 hours of operation. Capsules 652, 656, and 660 were irradiated under mixed irradiation temperature conditions and achieved a low burnup, therefore minimal examination took place. On the remaining 12 capsules, ORNL performed an extensive examination.

The first analysis was a microscopic examination by utilizing a gamma scan to determine the relative burnup of each fuel pellet. Weaver et al. [64] concluded that all fuel pellets experienced a relatively uniform burnup except for the fuel ends, where more neutrons were present. Through macroscopic examination, no fuel pin damage or failure was noted. A diametral change calculation performed concluding that all pins remained below the maximum design diametral change of 2%. Three fuel pins reached 1.9%, however the capsules all achieved approximately greater than 4 %FIMA burnup, nearly three times the reference design conditions. All other pins achieved less than 1% total change. For fuel swelling it was concluded that all the fuel pellets maintained less than the allowable limit of 8%, except for capsule 003 which achieved 8.7%. Again, this occurred with the highest burnup at the highest irradiation temperature. It was concluded through a metallographic examination, that the fuel swelling was caused by the migration of fission gas through UN, which coalesced at the grain boundaries. This conclusion agrees with that of DeCrescente et al. [19] during the post irradiation examination at CANEL.

The data in Fables 3.10 through 3.12 are split into high and low power densities to provide consistency with the CANEL data above. Capsules 003 and 665 are shown for comparison as they achieved similar burnups at varying irradiation temperatures. Capsule 003 was irradiated at temperatures approximately 200 K higher than capsule 665. Capsule 003 achieved higher volumetric swelling as well as diametral increase indicating that an increase in irradiation temperature increases both parameters.

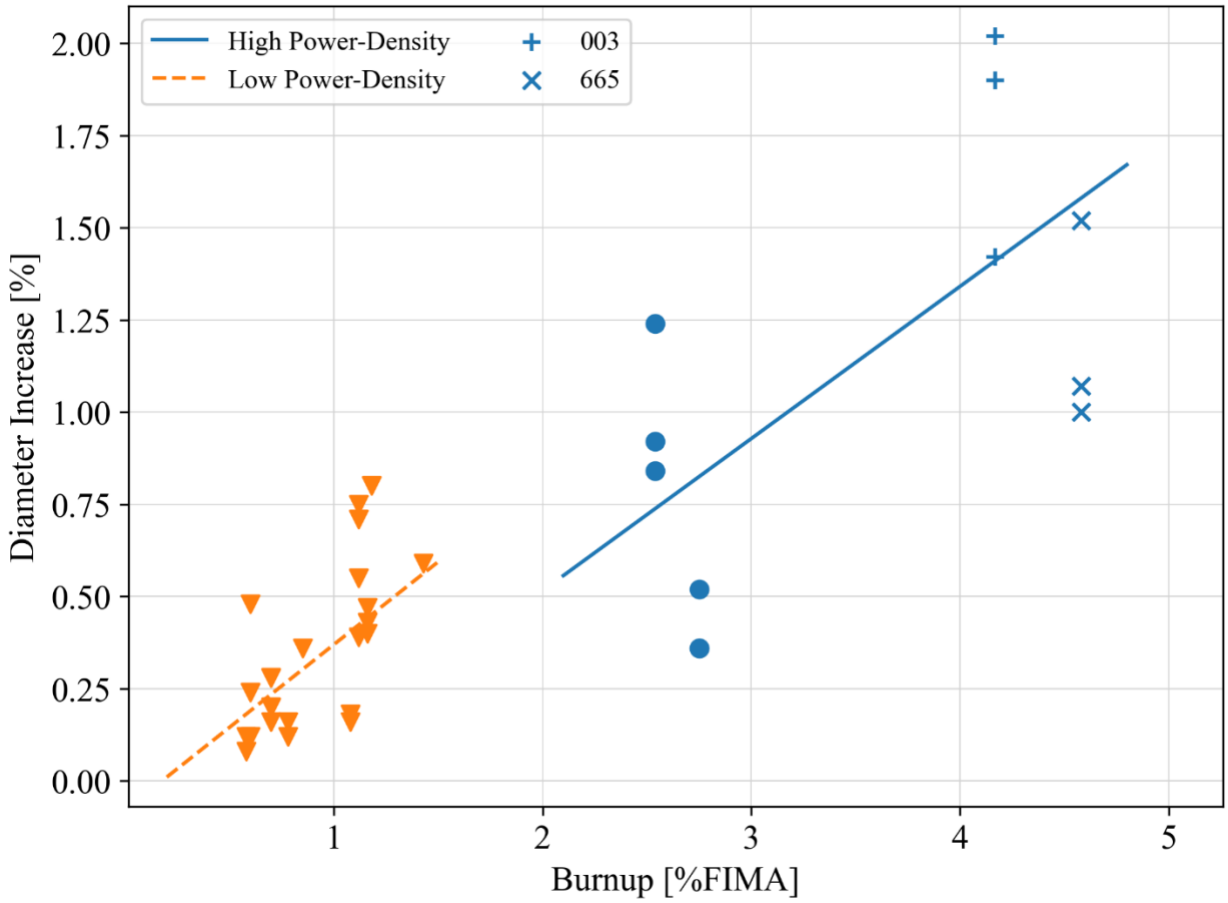

Figure 3.10: Diametral fuel swelling versus burnup for SNAP-50 testing performed at ORNL [64].

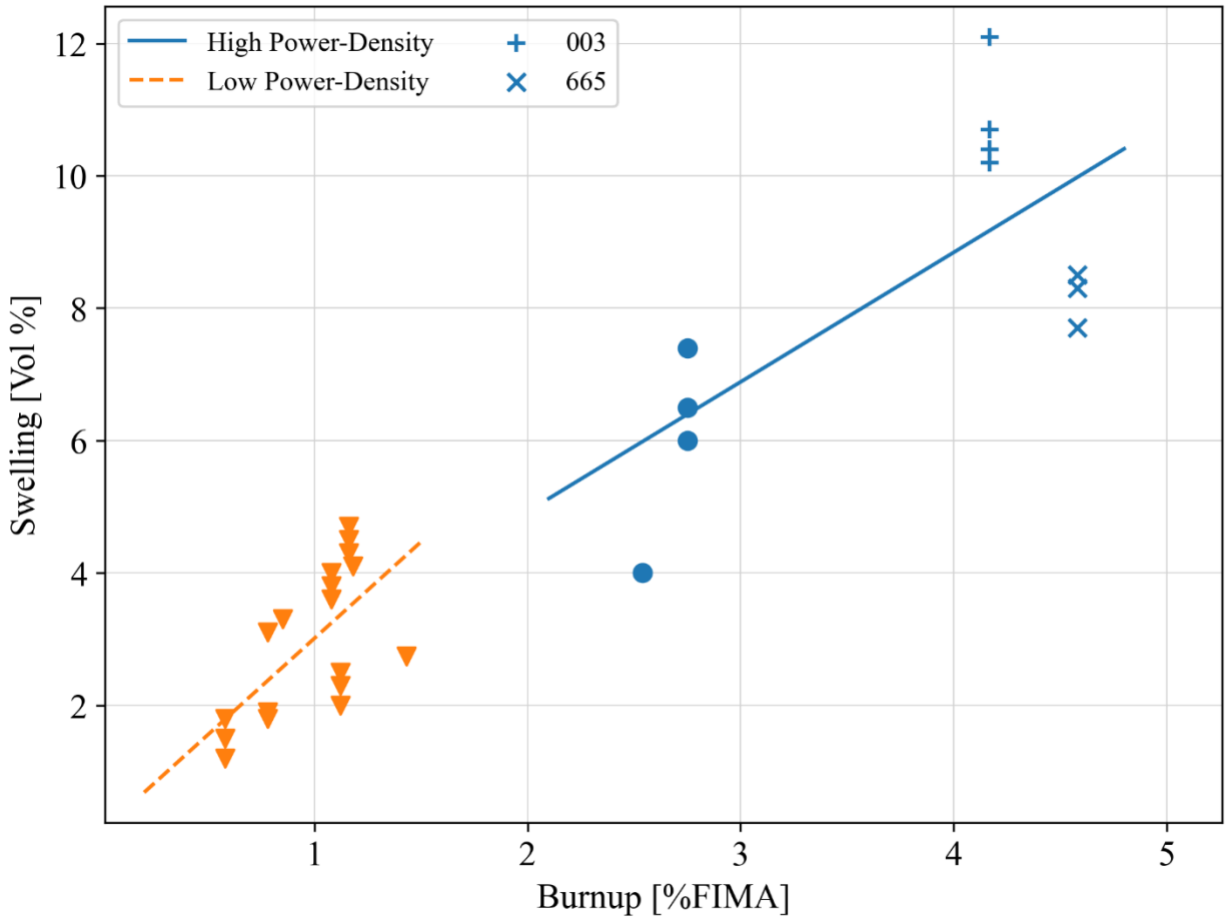

Figure 3.11: Volumetric fuel swelling versus burnup for SNAP-50 performed at ORNL [64].

The last evaluation was to determine the fission gas release in each fuel pin. Utilizing mass spectrometry and gamma counting, it was determined that all fuel pins released less than the allowable limit of 20%. It was concluded that the maximum fission gas release was approximately 12%, in capsule 003, which achieved the highest burnup at the highest irradiation temperature. Additionally, Weaver et al. [64] noted that fission gas release for the middle test pin in capsule 665 was higher due to post examination error. When puncturing the capsule, the fuel was fractured, and additional fission gas was released. Weaver et al. [64] suggested that the actual fission gas release was the same as the two other fuel pins in the capsule, approximately 2%. Comparing capsule 003 and 665, both of which operated at a higher power density and achieved a higher burnup than the reference design, it is concluded that UN should release approximately 2 to 10% of the fission gases. Additionally, as shown in Figure 3.12, when comparing the two capsules, the increase in irradiation temperature increased the overall fission gas release. This also can be seen in Figure 3.13 which shows the total fission gas release versus fuel volume increase for both ORNL and CANEL irradiation data. This shows that fission gases are less likely to escape from the fuel for lower overall fuel temperature.

In conclusion, during the SNAP-50 irradiation program, UN performed within the design criteria regardless of the burnup achieved and nearly all fuel pins tested showed no signs of failure or cladding rupture. As the irradiation temperature increases, the diametral and volumetric fuel swelling increases as does the total fission gas release. To further examine the three capsule failures at CANEL, a comparison can be done with capsules 642, 643, and 649 of ORNL, which are of the same dimensions and capsule construction. These three capsules were irradiated for more time at the same temperatures; however, the power densities were approximately half of those at CANEL. In the test capsule that did not rupture at CANEL, the volumetric swelling is nearly three times that of capsule 643 which was irradiated for a similar amount of time. Additionally, the fission gas release in both capsules was very low or undetectable. No failures occurred at ORNL, and the volumetric swelling was significantly less, therefore it is concluded that the increase in power densities caused a more rapid increase fission gas production and migration to the grain boundaries, causing an increase in volumetric swelling, ultimately causing the rupture of cladding.

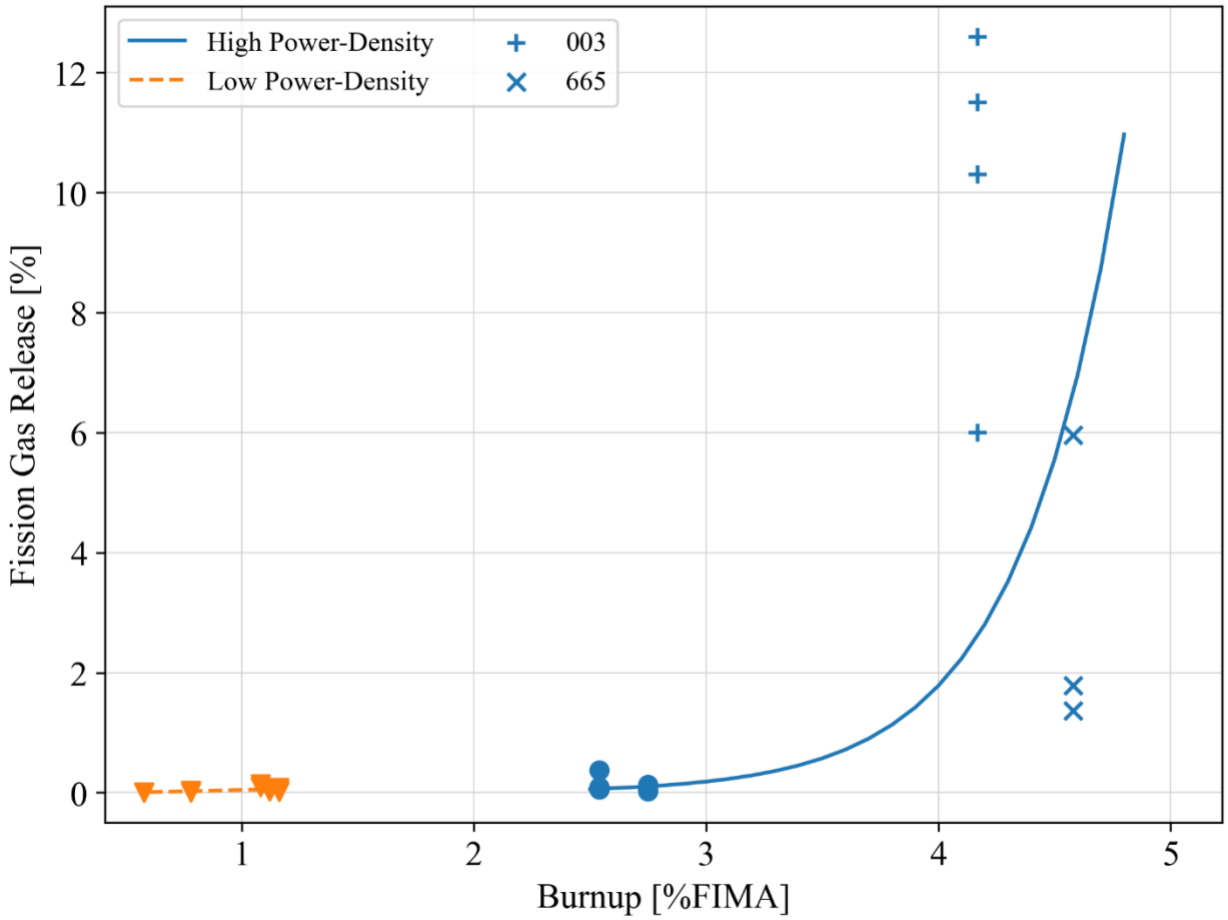

Figure 3.12: Fission gas release versus burnup for SNAP-50 performed at ORNL [64].

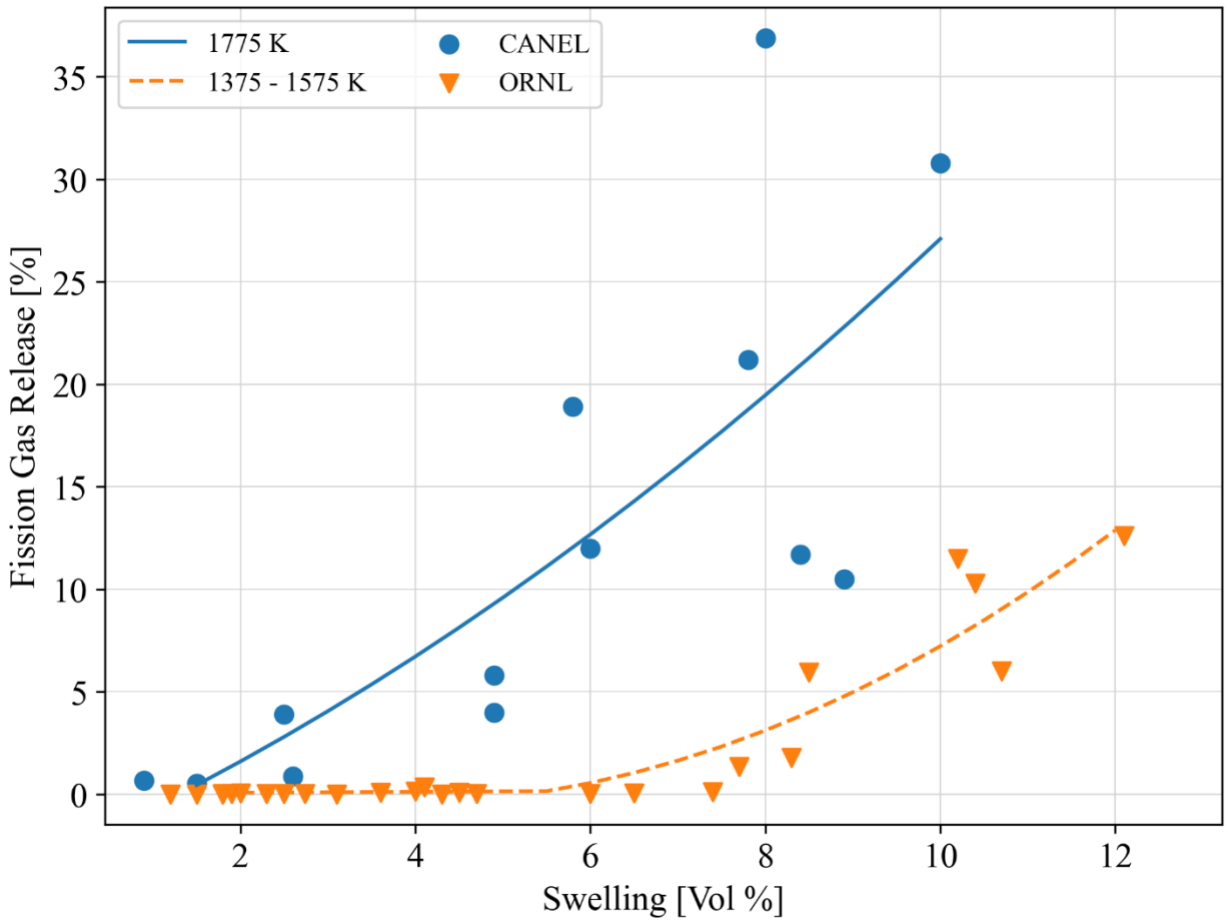

Figure 3.13: Fission gas release versus fuel swelling for CANEL and ORNL [64].

Table IX. Capsule and UN fuel data for high power density irradiation tests conducted at CANEL [19, 63].

	Capsule #	Location	Barrier	Cladding Type	Specimen Per Capsule	Capsule Length [cm]	Capsule Dia. [cm]	Cladding Thickness [cm]	Fuel Diameter [cm]	Fuel Length [cm]	Density [% TD]	Enrichment [% U-235]	Nitrogen [w/o]	Oxygen [ppm]
High Power Density	201	T	None	Nb-1Zr	3	4.016	0.7976	0.0914	0.6096	1.539	90.3	93.2	-	-
		M									90.8			
		B									90.3			
	210	T	None	Nb-1Zr	3	4.016	0.7849	0.0889	0.6020	1.651	96.1	31.5	-	1300
		M									96.1			
		B									96.2			
	220	T	None	Nb-1Zr	3	4.016	0.7823	0.0889	0.6020	1.651	94.1	12.3	-	1400
		M									94.3			
		B									94			
	230	T	1 Mil W foil	Nb-1Zr	3	4.013	0.7925	0.0889	0.6020	1.651	96.4	10.9	-	2650
		M									96			
		B									95.7			
	231	T	1 Mil W foil	Nb-1Zr	3	4.013	0.7950	0.0889	0.6020	1.651	96	11.4	-	2650
		M									96.1			
		B									96.2			
	240	T	1 Mil W foil	Nb-1Zr	3	3.990	0.7493	0.0635	0.6121	1.651	95	12.6	-	945
		M									94.9			
		B									94.4			
	241	T	1 Mil W foil	Nb-1Zr	3	3.990	0.7493	0.0635	0.6121	1.651	94.9	10.6	-	945
		M									94.7			
		B									94.3			
	630*	-	5 Mil W foil	PWC-11	1	11.760	0.6350	0.7620	0.4775	8.382	94.8	10.1	5.25	1880
	631*	-	5 Mil W foil	PWC-11	1	11.760	0.6350	0.7620	0.4775	8.382	95.3	10.1	5.36	1325
	632	-	5 Mil W foil	PWC-11	1	11.760	0.6350	0.7874	0.4699	8.306	95.7	10	5.26	1500
	633	-	5 Mil W foil	PWC-11	1	11.760	0.6350	0.7620	0.4775	8.357	95	10.1	5.35	1880
	635	-	5 Mil W foil	PWC-11	1	11.760	0.6350	0.7874	0.4699	8.382	96.2	10	5.26	1500

* Fuel pellets contain 51 mil diameter central hole

Table X. Capsule and UN fuel data for low power density irradiation tests conducted at CANEL [19, 63].

	Capsule #	Barrier	Cladding Type	Specimen Per Capsule	Capsule Length [cm]	Capsule Dia. [cm]	Cladding Thickness [cm]	Fuel Diameter [cm]	Fuel Length [cm]	Density [% TD]	Enrichment [% U-235]	Nitrogen [w/o]	Oxygen [ppm]
Low Power Density	600	3 Mil W foil	Nb-1Zr	3	3.810	0.635	0.071	0.485	1.654	97.8 96.2 95.5	10.3	5.30	2050
	601	3 Mil W foil	Nb-1Zr	3	3.810	0.635	0.071	0.488	1.651	96.7 96.2 95.6	10.3	5.30	2050
	602	3 Mil W foil	Nb-1Zr	3	3.810	0.635	0.071	0.483	1.651	95.4 95.6 94.6	10.3	5.30	2050
	603	3 Mil W foil	Nb-1Zr	3	3.810	0.635	0.071	0.488	1.654	96.2 95.8 95.5	10.3	5.90	2050
	610	5 Mil W foil	Nb-1Zr	3	3.810	0.630	0.076	0.472	1.651	96.7 95.9 96.4	10.7	5.33	2050
	613	5 Mil W foil	Nb-1Zr	3	3.810	0.640	0.079	0.472	1.651	96.4 96 95.9	10.7 10.4 10.4	5.33	2700
	640*	5 Mil W Foil	PWC - 11	1	11.760	0.635	0.076	0.478	8.382	94.3	10.06	5.33	1500
	200	None	Nb-1Zr	3	4.013	0.798	0.091	0.610	1.534	90.4 91 90.6	93	-	-

* Fuel pellets contain 51 mil diameter central hole

Table XI. UN irradiation data for high power density irradiation tests conducted at CANEL [19, 63].

	Specimen #	Location	Irradiation Time [hr] (days)	Avg. Cladding Temp. [K]	Maximum Fuel Temp. [K]	Power Density [kW/cc]	Fluence [n/s]	Burnup [%FIMA]	Fission Gas Release [%]	Maximum Dia. Swelling [%]	Fuel Swelling [%]
High Power Density	**201**	**T**	1590 (66.25)	1241	1408	0.93	9.85E+18	0.54	-	0.0	0.0
		M		1353	1533	0.97	1.03E+19	0.57	3.5	0.0	0.0
		B		1311	1533	1.23	1.30E+19	0.72	5.1	0.0	0.0
	210	**T**	1090 (45.42)	1380	1575	1.11	1.96E+19	0.42	3.0	0.0	1.6
		M		1436	1630	1.12	1.98E+19	0.42	3.3	0.0	1.1
		B		1436	1630	1.05	1.85E+19	0.40	2.5	0.0	2.0
	220	**T**	1690 (70.42)	1297	1561	1.51	1.52E+20	0.95	4.9	0.47	5.0
		M		1450	1714	1.50	1.51E+20	0.95	12.0	0.78	6.0
		B		1297	1589	1.53	1.54E+20	0.96	4.3	0.37	1.9
	230	**T**	850 (35.42)	1408	1728	1.82	9.03E+19	0.58	0.53	0.0	1.5
		M		1491	1825	1.95	9.67E+19	0.63	0.88	0.0	2.6
		B		1380	1714	1.9	9.43E+19	0.61	0.68	0.0	0.9
	231	**T**	2750 (114.59)	1353	1714	2.03	3.26E+20	1.94	**10.5**	0.77	**8.9**
		M		1491	1839	2.00	3.21E+20	1.91	**30.8**	1.54	**10.0**
		B		1394	1769	2.12	3.40E+20	2.02	**11.7**	0.93	**8.4**
	240	**T**	3000 (125)	1408	1700	1.47	2.61E+20	1.51	18.9	0.77	5.8
		M		1478	1783	1.57	2.79E+20	1.61	36.9	2.0	8.0
		B		1436	1700	1.54	2.73E+20	1.58	21.2	1.0	7.8
	241	**T**	1100 (45.83)	1436	1797	2.06	1.34E+20	0.78	5.8	0.2	4.9
		M		1491	1839	2.00	1.30E+20	0.74	3.9	0.37	2.5
		B		1422	1755	1.92	1.25E+20	0.72	4.0	0.0	4.9
	630*	-	810 (33.75)	1491	1644	1.18	5.59E+19	0.31	0.06	0	2.99
	631*	-	3360 (140)	1478	1630	1.20	2.35E+20	1.42	-	0.36	8.17
	632	-	3370 (140.17)	1478	Cladding Failure						9.4
	633	-	3360 (140)	1478	1644	1.23	Cladding Failure	1.47	Cladding Failure		12.65
	635	-	3300 (137.5)	1478	Cladding Failure						13.35

* Fuel pellets contain 51 mil diameter central hole

Table XII. UN irradiation data for low power density irradiation tests conducted at CANEL [19, 63].

	Specimen #	Location	Irradiation Time [hr] (days)	Avg Cladding Temp. [K]	Max Fuel Temp. [K]	Power Density [kW/cc]	Fluence [n/s]	Burnup [%FIMA]	Fission Gas Release [%]	Max Dia. Swelling [%]	Fuel Swelling [%]
Low Power Density	**600**	**T**	660 (27.50)	1311	1380	0.54	2.07E+19	0.19	0.1	0.08	3.0
		M		1436	1505	0.54	2.07E+19	0.18	0.1	0.20	1.8
		B		1450	1519	0.53	2.03E+19	0.18	0.1	0.36	1.8
	601	**T**	1370 (57.08)	1366	1436	0.47	3.75E+19	0.39	0.1	0.00	3.5
		M		1436	1491	0.48	3.83E+19	0.39	0.2	0.00	2.7
		B		1422	1491	0.48	3.83E+19	0.40	0.2	0.00	2.1
	602	**T**	5940 (247.50)	1214	1269	0.47	1.64E+20	0.97	0.02	0.12	3.0
		M		1366	1422	0.44	1.54E+20	0.91	0.20	0.24	3.5
		B		1339	1394	0.42	1.47E+20	0.86	0.08	0.20	2.4
	603	**T**	3310 (137.92)	1214	1297	0.64	1.24E+20	0.74	0.05	0.56	2.9
		M		1366	1450	0.64	1.24E+20	0.73	0.10	0.24	2.7
		B		1339	1422	0.62	1.20E+20	0.71	0.06	0.36	2.1
	610	**T**	380 (15.83)	1269	1353	0.62	1.37E+19	0.16	0.0	0.00	1.6
		M		1366	1450	0.62	1.37E+19	0.16	0.0	0.00	1.5
		B		1353	1436	0.65	1.44E+19	0.17	0.0	0.00	1.5
	613	**T**	1970 (82.08)	1283	1394	0.81	9.31E+19	0.54	0.04	0.08	1.0
		M		1394	1505	0.8	9.19E+19	0.53	0.06	0.00	1.4
		B		1297	1408	0.88	1.01E+20	0.58	0.03	0.40	1.7
	640*	-	2540 (105.83)	1478	1533	0.44	6.64E+19	0.42	0.04	0.00	1.2
	200	**T**	390 (16.25)	1103	1186	0.44	1.14E+18	0.06	0.08	0.00	-
		M		1214	1283	0.41	1.06E+18	0.06	0.09	0.00	-
		B		1116	1200	0.37	9.59E+17	0.05	-	0.00	-

* Fuel pellets contain 51 mil diameter central hole

Table XIII. Capsule and UN fuel data for irradiation tests conducted at ORNL [64].

Capsule #	Barrier	Cladding Type	Specimen Per Capsule	Capsule Length [cm]	Capsule Dia. [cm]	Cladding Thickness [cm]	Fuel Diameter [cm]	Fuel Length [cm]	Density [% TD]	Enrichment [% U-235]	Carbon [ppm]	Oxygen [ppm]
612	5 Mil w/ VD	PWC-11	3	4.013	0.635	0.064	0.478	1.651	90-97%	10	500	1000
642			1	12.040				8.382				
643												
649												
652			3	4.013				1.651				
656												
658												
660												
662												
664												
665												
667												
669												
002			4									
003			4									

Table XIV. UN irradiation data for irradiation tests conducted at ORNL [64].

Specimen #	Location	Irradiation Time [hr] (days)	Avg. Cladding Temp. [K]	Maximum Fuel Temp. [K]	Power Density [kW/cc]	Fluence [n/s]	Burnup [%FIMA]	Fission Gas Release [%]	Maximum Dia. Swelling [%]	Fuel Swelling [%]
612*	**T**	5205 (216.88)	1143	1338	1.41	4.11E+20	2.54	0.050	0.84	4-6*
	M		1248	1453				0.370	1.24	4-6*
	B		1188	1383				0.090	0.92	4-6*
642	-	9966 (415.25)	1453	1498	0.34	1.90E+20	1.18	0.340	0.80	4.1
643	-	4292 (178.83)	1453	1533	0.57	1.37E+20	0.85	-	0.36	3.3
649	-	10512 (438)	1433	1488	0.4	2.36E+20	1.43	0.038	0.59	2.7
652**	**T**	3180 (132.50)	1368 (1000 hr)	1458	0.64	1.14E+20	0.7	-	-	-
	M		1478 (2180 hr)	1568				0.090	0.16	-
	B							-	0.20	-
656**	**T**	3180 (132.50)	1368 (1000 hr)	1453	0.53	9.45E+19	0.6	0.030	0.24	-
	M		1478 (2180 hr)	1563				0.110	0.12	-
	B							0.130	0.48	-
658	**T**	9779 (407.46)	1388	1428	0.32	1.75E+20	1.08	-	-	3.8
	M		1458	1503				0.140	0.18	4.0
	B		1438	1483				0.090	0.16	3.6
660**	**T**	2635 (109.79)	1368 (1000 hr)	1473	0.76	1.12E+20	0.7	-	0.28	-
	M		1478 (2180 hr)	1583				0.050	0.28	-
	B							-	0.20	-
662	**T**	10270 (427.92)	1338	1388	0.37	2.13E+20	1.16	0.010	0.47	4.3
	M		1473	1523				0.080	0.43	4.5
	B		1463	1513				0.040	0.40	4.7
664	**T**	6209 (258.71)	1373	1418	0.27	9.40E+19	0.58	0.005	0.12	1.8
	M		1423	1463				0.005	-0.08	1.5
	B		1438	1478				0.005	0.08	1.2
665*	**T**	9583 (399.30)	1133	1323	1.39	7.47E+20	4.58	1.360	1.00	7.7
	M		1238	1426				5.960	1.52	8.5
	B		1178	1373				1.780	1.07	8.3
667	**T**	6209 (258.71)	1388	1438	0.36	1.25E+20	0.78	0.005	-	3.1
	M		1448	1498				0.020	0.12	1.8
	B		1453	1503				0.030	0.16	1.9
669*	**T**	10353 (431.38)	1108	1213	0.76	4.41E+20	2.75	0.050	0.52	6.5
	M		1253	1348				0.130	0.36	7.4
	B		1203	1308				0.020	0.36	6.0
002	**T**	10173 (423.88)	1398	1443	0.32	1.82E+20	1.12	0.020	0.39	2.5
	M		1458	1503				0.020	0.55	2.3
	M		1476	1518				0.060	0.71	2
	B		1438	1478				-	0.75	-
003*	**T**	11985 (499.38)	1373	1513	1.01	6.78E+20	4.17	6.000	1.42	**10.7**
	M		1433	1573				10.300	1.9	**10.4**
	M		1458	1598				11.500	2.02	**10.2**
	B		1433	1573				12.600	1.9	**12.1**

* Altered fuel capsules to achieve higher power density and higher burnup (*highlighted in grey*)

** Mixed irradiation conditions

3.3.3. Advanced Space Power Nuclear Reactor Concept (NASA)

During the 1970's, NASA Lewis Research Center began an investigation into a space power conversion system, drawing closely from a former program, SNAP-50 [81-84]. The overall design of the reference reactor remained the same while employing minor operational differences. The reactor design remained a compact, liquid-metal-cooled, fast-spectrum reactor for space power applications however the operational time was extended from 10,000 to 50,000 hours with a goal of less than 1% diametral cladding strain on the fuel pins up to approximately 4 %FIMA burnup [85]. The reference design fuel pin was 1.9 cm in diameter, 43 cm in length with a fuel length of approximately 38 cm, clad with 0.15 cm thick T-111, with a 0.013 cm thick Tungsten barrier [86].

UN was chosen as the primary fuel candidate due to the data collected during recent irradiation studies along with its high fuel density, thermal conductivity, and compatibility with a lithium coolant. Various alloys were considered for the cladding material. Due to its high-temperature creep strength, room temperature ductility, previous experience and fabricability a Tantalum alloy, T-111 (Ta – 8%W – 2%Hf) was chosen [85].

Testing began with a preliminary isothermal test which were conducted on a reference fuel pin at a temperature of ≈1315 K. The purpose of this test was to analyze the unirradiated compatibility of the fuel pin under reactor operating conditions. Post testing analysis indicated that a reaction took place at the contact between UN and its cladding T-111, confirming that a tungsten barrier was required [86].

NASA performed a series of irradiation experiments at the Plum Brook reactor facility throughout the 1970s. Available literature indicates that approximately 43 fuel rods were irradiated and analyzed. Testing began with three separate irradiation effects tests: An accelerated burnup-rate test on miniature fuel pins to obtain initial irradiation information; fuel pin design proof tests to ensure the preliminary design showed promise of meeting the diametral cladding strain goal of 1%; and determining the effects of UN fuel density on swelling and fission gas release [86]. Each of these tests and their associated post irradiation analyses are described below. Results for volumetric fuel swelling and fission gas release are shown in Figures 3.14 and 3.15, respectively. Applicable irradiation and testing information is provided in Tables XV through XXIV.

The first test was designed to collect early information on the capabilities of the refence fuel pin design. As described by Rohal et al. [87], a total of twelve UN fuel pins, split into two capsule assemblies (321 and 322) were irradiated in the Plum Brook Reactor at a goal cladding surface temperature of 1200 K. Assembly 321 was irradiated for approximately 1500 hours while assembly 322 was irradiated up to 3000 hours. Fuel pins in assembly 321 achieved a burnup ranging from 0.4 to 0.7 %FIMA while the fuel pins in assembly 322 achieved burnups ranging

from 0.5 to 1.0 %FIMA. Each fuel pin contained four UN pellets with an outside diameter of 0.381 cm, inside diameter of 0.119 cm and a length of 0.635 cm. Each pellet contained a density ranging from 95 to 97%. Each fuel pin was clad with T-111 of thickness 0.71 cm. Two groups of fuel pins, 321 and 322, contained two differences. First, the first six fuel pins (capsule 321) contained a single layer of tungsten, 0.0025 cm thick. The second group of six fuel pins (capsule 322) contained two layers of 0.0025 cm tungsten, requiring the cladding thickness to reduce to 0.066 cm. The two layers of the tungsten barrier was intended to prevent any direct fuel to cladding interaction, by overlapping the gap where the edges of the barrier came together. Additionally, during the testing of the first six fuel pins, it was determined that the cladding experienced embrittlement. It was determined that this embrittlement may have been caused by contamination from dissimilar metals during the manufacturing process. Ductility in the cladding was seen to increase during the second set of tests, indicating that careful consideration must be taken when fabricating T-111 cladding.

Visual inspection of these fuel pins indicated no issues of swelling, corrosion, or failure. Fission gas release was measured by a pressure transducer, measuring the pressure rise in a fixed plenum volume. The transducer was rated to read as low as 1% change however there was no deflection, concluding fission gas release was less than 1% in all fuel pins. Overall, the fuel pins operated as expected up to an equivalent 18,000 hours at refence design conditions. The total fission product release from UN, as determined by xenon and krypton concentrations, was approximately 0.05% up to 1 %FIMA burnup. No swelling data was recorded during this series of tests.

The next series of tests was focused on the capability of the fuel pin to stay within the reference design limit of a 1% diametral cladding strain. As described by Slaby et al. [61], a total of three UN fuel pins containing six UN fuel pellets were irradiated at a goal cladding surface temperature of 1265 K for 8070 hours. One fuel pin was tested at the reference design diameter and burnup rate while the remaining two fuel pins were tested at a reduced diameter and therefore increased burnup rate. Each fuel pin contained six fuel pellets that were 94% TD, clad with T-111 and lined with a tungsten barrier. The reference fuel pellets had an outside diameter of 1.580 cm and an inside diameter of 0.511 cm with a length of 5.72 cm. The cladding was 0.1016 cm thick with a 0.0127 cm thick barrier of tungsten. The two reduced diameter fuel pins contained fuel pellets with an outside diameter of 0.788 cm and inside diameter of 0.279 cm. The T-111 cladding was 0.0508 cm thick with a 0.0076 cm thick tungsten barrier.

Testing on the three fuel pins concluded after 8070 hours of operation at an average cladding temperature of approximately 1265 K. The average fuel centerline temperature for the reference fuel pin was 1367 K and the average centerline temperature for the two reduced fuel pins was 1257 and 1254 K. The reference fuel pin achieved a total burnup of 0.468 %FIMA while the two reduced fuel pins achieved 0.785 and 0.780 %FIMA. Both reduced fuel pins achieved a higher percent change in diameter and length as compared to the reference fuel pin while the change in

density was approximately the same. During post-irradiation inspection, it was noted that during stack disassembly, all the fuel pellets in the reference fuel pin contained cracks and all but the top fuel pellet fell apart. Therefore, the information provided is only for the top fuel pellet while the half diameter fuel pellets are an average among all six. No conclusion was drawn to indicate why this occurred specifically with the reference design fuel pellets. During dimensional measurements, it was concluded that due to the diametral gap between the fuel and cladding, no cladding contact was made and therefore the cladding experienced minimal strain.

Visual inspection from all three fuel pins indicated no external clad failures. However, after puncturing the fuel pin outer containment, fission gas was present in one half diameter fuel pin indicating a small leak. This was identified at the thermocouple well weld and not the cladding surface or end caps. Fission gas was determined by determining the amount of krypton-85 activity after the cladding puncture. It was determined that total fission gas release was less than 0.05% in all three fuel pins.

The next testing series was a continuation of the above test designed to evaluate the viability of the reference design limit of a 1% diametral cladding strain. As described by Slaby et al. [60], a total of 29 UN fuel pins each containing six cored UN fuel pellets were irradiated at a goal cladding surface temperature of 1265 K for times up to 13,000 hours. Two fuel pin testing conditions were used: a reference diameter and burnup rate and one with half the diameter and an increased burnup rate of two or four times the reference design. The reference design fuel pellets dimensions are the same as those described above. To further test the cladding restraint of the T-111 cladding, two cladding thickness were used. A T-111 cladding thickness of 0.147 cm or 0.102 cm were used for the reference diameter and 0.074 or 0.051 cm for the half diameter fuel pin. The reference diameter pins contained a tungsten liner thickness of 5-mil while the half diameter fuel pins contained a 3-mil thick tungsten liner. One full length prototype fuel pin was studied which contained one fuel pellet of length 38.1 cm, utilizing the dimension of the reference diameter fuel pin. 27 of 29 fuel pins were analyzed after irradiation. Measured burnup ranged from 0.40 up to 2.34 %FIMA.

Post irradiation examination was conducted focusing on various areas including fuel pin integrity, fission gas release, and fuel swelling. However, the program was terminated before all 29 fuel pins were able to be analyzed in all areas on interest. Only 27 of the 29 fuel pins were examined, which all 27 fuel pins were not examined for every key irradiation parameter. Only 27 of the 29 fuel pins were tested due to two failures, one due to water leakage into the capsule after approximately 10,000 hours of operations and the other had a defective end cap allowing air into the fuel pin prior to irradiation. Actual irradiation times ranged from 1150 hours up to 13000 hours, allowing the accelerated conditions to achieve an equivalent 35400 hours and approximately 2.3 %FIMA burnup. The following is a summary of the significant conclusions from testing.

First, 22 fuel pins were checked for leaks, 9 regular clad and 13 thin clad. Three of the 9 regular clad pins and 10 of the 13 thin clad contained leaks, primarily around welds or thermocouple wells. Only two fuel pins had visible cladding cracks. It is noted that the percent change in one of the fuel pins that failed, 503I, was 2.2 % at a burnup of 2.16 at.%. This was equated to a clad strain of approximately 1.36% which exceeded the design limit of 1%. This percent increase is significantly greater than any other fuel pin. In fact, no fuel pins that were irradiated at the normal time or a factor of two showed a diametral increase in cladding. This was attributed to the sufficient gap to allow fuel swelling before contact was made on the cladding. It was concluded that the cracks were due to elevated local stresses where the seam of the tungsten liner contacted the cladding. In attempt to prevent this in the future, a bonding method was developed to reduce the size of the seam limiting the localized stresses. In one fuel pin that was subject to a severe overtemperature, five of the six fuel pellets showed axial cracks however they did not break apart. All other fuel pellets did not display axial cracks. A metallographic examination was the last analysis performed on the fuel pellets. The conclusion is that there were no microstructural changes including no signs of grain growth, second phases, fission gas bubbles or void migration. From the fuel pellet analyses, it was concluded that the fuel swelling was burnup dependent and was essentially isotropic based on the diameter and length calculations. In conclusion, the variations in cladding thicknesses coupled with the accelerated testing environment created various unknown conditions which may have attributed to the increase leaks and cracks. However, overall, fuel swelling was approximately 2% up to approximately 1 %FIMA burnup with fission gas release less than approximately 0.5%.

The next test focused on comparing the performance of UN fuel pins with varying the material variables, namely UN density variations. As described by Bowles and Gulyas [56] and Thoms [62], six fuel pins containing 8 or 9 UN fuel pellets were irradiated at ORNL for up to 10,000 hours at an average surface cladding temperature of 1265 K. Two fuel pins contained cored 94% TD UN pellets while the other four fuel pins contained non-cored 85% TD UN pellets. The fuel pellets had an outer diameter of 0.78 cm, and the cored pellets had an inner diameter of 0.23 cm. All fuel pins were clad with T-111 with a 3-mil tungsten liner.

Neutron radiographs were performed on all fuel pins throughout the irradiation testing. It was determined that after approximately 9000 hours of testing, the cladding of both fuel pins containing 95% dense UN fuel pellets displayed axial cracking. At the conclusion of the test, the fuel pins containing 95% dense UN fuel pellets appeared to experience a major cladding crack. This was confirmed during the post irradiation visual inspection at ORNL. No other significant visual anomalies were noted. ORNL then performed weight and diametral measurements along with a helium leak detection. During the leak detection process, it was determined that two fuel pin experienced a slight leak, however no visual indications of cracks were noted. Based off a weight measurement alone, pins 12 and 14, which experienced cracks, increased in weight by approximately 1.5 to 3 percent. This was concluded to be due to the intrusion of the surrounding medium around the outside of the cladding.

After irradiation and an initial examination, the fuel pins were transferred back to the NASA Plum Brook Reactor Facility to undergo a more rigorous evaluation. The fuel pins were again leak checked, weighed, and dimensionally measured. NASA concluded the same results as ORNL. NASA then performed additional tests such as fuel density measurements, and fission gas measurements. These tests were only performed on two fuel pins, one from each density (fuel pins 11 and 14). Density measurements were determined by both an immersion technique along with dimensional measurements. Utilizing the immersion technique may yield values which are too high due to the liquid penetration into porous material while the dimensional measurements may yield value which are too low if cracks are present in the material. Due to the porosity of the fuel samples and the cracks present in the fuel, both methods would sufficiently bracket the actual change in density. Therefore, the data presented in Table XXX is an average between both results. It was found that the density of the 95% dense unirradiated fuel pellet decreased considerably while the density of the 85% dense unirradiated fuel remained relatively constant. It was concluded that the high-density fuel had a reduction in density due to the collection of fission gases in the closed porosity resulting in increased swelling. It was concluded that the low-density fuel was due to the interconnected porosity, allowing for more fission gas release or increased local accommodation of the fission gases. Diameter measurements were performed on all the fuel pins expect fuel pins 12 and 14, due to cracks in the cladding. It was concluded that no fuel pin exceeded the diametral strain of 1%. Based on measurements of the cracked cladding and a cladding wall profile, it was hypothesized that the cladding in fuel pin 14 most likely cracked at approximately 1.5% diametral cladding strain. No fuel pellet dimensional measurements were provided therefore there are no concrete conclusion that can be drawn for fuel swelling. A fission gas release test was performed on the low-density fuel pin however it could not be performed on the high-density fuel pin due to cladding cracks. It was determined that 4.3% fission gas release at 2.76 %FIMA burnup. This is slightly higher than previous fission gas measurements and 95% dense fuel. It was concluded that this was due to the increase fission gas release in the more porous material. In conclusion, it was found that lower density fuel imparted less stress into T-111 cladding limiting the diametral strain to less than the required 1%. Additionally, the high-density fuel experienced a higher decrease in fuel density due to the fission gas retention and therefore increased swelling.

The final test performed focused on understanding the unrestrained fuel swelling of UN and the associated fission gas release. As described by Rohal and Tambling [72], a total of 6 UN fuel pins were irradiated at the Plum Brook Reactor at a goal cladding temperature of 1100 K for approximately 4000 hours. Each fuel pin contained 4, 10% enriched UN fuel pellets with a density of 94.3% TD. The fuel pins were clad with a 0.076 cm thick 304L stainless steel and filled with helium. Stainless steel was used due to the limited restraint on the UN fuel pellets at the desired irradiation temperatures. The diameter of the fuel pins was approximately one-fourth the reference design and were irradiation at six to ten times the burnup rates. The outside diameter of the fuel pellets was 0.381 cm, the outside diameter of the stainless-steel cladding was 0.534 cm.

Minimal post irradiation examination data is available due to the program terminating before all fuel pins could be analyzed. Visual inspection indicated no failures of any fuel pin. Diametral swelling is approximately 0.5, 0.8 and 1.0 percent at 1 percent burnup for temperatures 1223 K, 1264 K and 1306 K respectively. Diametral swelling of UN increases with increasing temperature, which is in agreement all other testing series. Additionally, the diametral swelling of fuel pellet 323F number 3 is 0.6% which the length increase percent is 0.76%. This indicates that that swelling of unrestrained UN fuel pellets is approximately isotropic.

While many of the testing programs were terminated prior to a full analysis was able to be performed on the fuel pins, valuable information was collected during the testing program of UN at Plum Brook Reactor. Overall, it is concluded that UN fuel swelling, and fission gas release is low for low burnups. Fuel pellet cracking was shown to be present in most irradiation tests. Fuel pin cladding failure was an issue resulting in voided tests and unusable data.

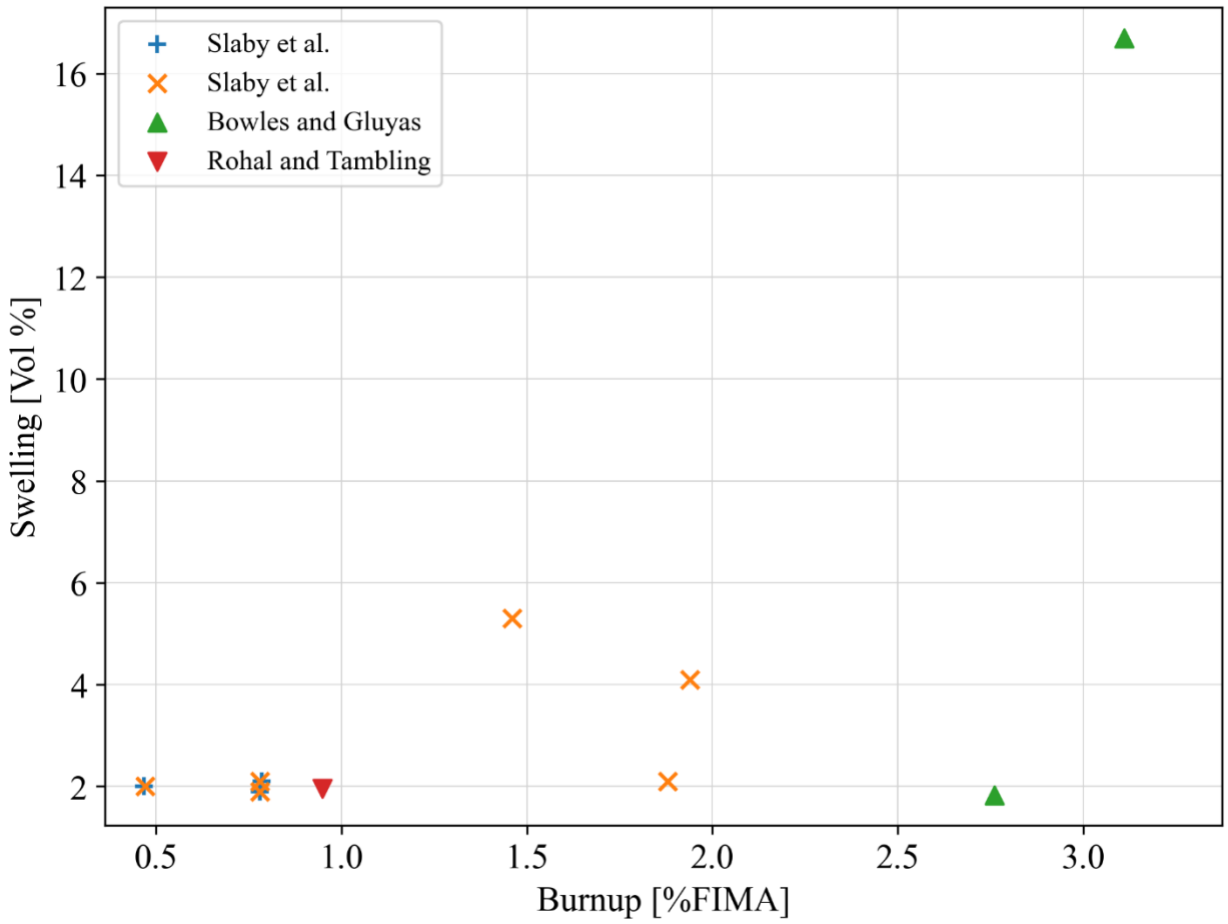

Figure 3.14: Volumetric fuel swelling versus burnup for NASA testing performed at PBRF [56, 60, 61, 72].

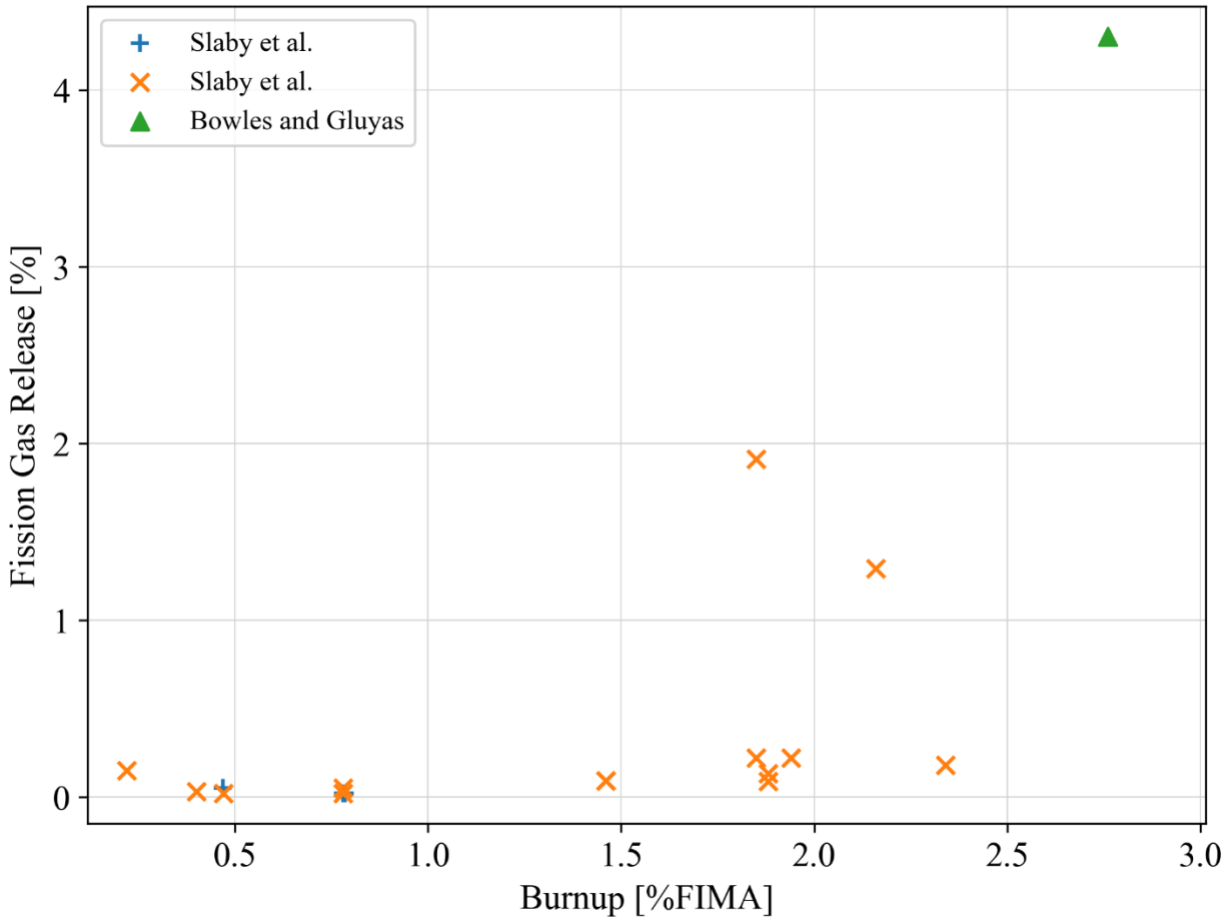

Figure 3.15: Fission gas release versus burnup for NASA testing performed at PBRF [56, 60, 61].

Table XV. Capsule and UN fuel data for irradiation tests conducted at Plum Brook [87].

Capsule #	Barrier	Cladding Type	Specimen Per Capsule	Capsule Length [cm]	Capsule Dia. [cm]	Cladding Thickness [cm]	Fuel Outside Diameter [cm]	Fuel Inside Diameter [cm]	Fuel Length [cm]	Density [% TD]	Enrichment [% U-235]	Carbon [ppm]	Oxygen [ppm]
321A	1 mil Tungsten	T-111	6	-	0.460	0.036	0.381	0.047	2.540	97.6	10	0.021 - 0.046	0.098 - 0.190
321B										96.4			
321C										96.9			
321D										94.2			
321E										95.0			
321F										95.3			
322A	2 mil Tungsten					0.033		0.047		95.2			
322B								0.000		95.0			
322C								0.047		94.3			
322D								0.000		94.9			
322E								0.047		95.9			
322F								0.000		95.0			

Table XVI. UN irradiation data for irradiation tests conducted at Plum Brook [87].

Specimen #	Irradiation Time [hr] (days)	Avg Cladding Temp. [K]	Average Fuel Temp. [K]	Power Density [kW/cc]	Fluence [n/cm^2]	Burnup [%FIMA]	Fission Gas Release [%]	Max Dia. Swelling [%]	Change in Density [%]
321A	1498 (62.42)	1119	1131	0.614	2.40E+20	0.708	<0.05	-	-
321B		1202	1224	1.002	5.40E+20	0.925			
321C		1125	1154	0.923	3.70E+20	0.925			
321D		1196	1213	0.803	2.90E+20	0.708			
321E		1220	1236	0.675	-	0.56			
321F		1150	1163	0.581	-	0.56			
322A	1369 (57.04)	1284	1298	0.740	2.50E+20	0.539			
322B	2278 (94.92)	1230	1251	0.956	5.50E+20	1.293			
322C	2888 (120)	1112	1143	0.980	-	1.498			
322D	2888 (120)	1247	1263	0.770	-	1.162			
322E	2888 (120)	1258	1272	0.580	-	0.885			
322F	1160 (48.3)	1258	1272	0.598	-	0.89			

Table XVII. Capsule and UN fuel data for irradiation tests conducted at Plum Brook [61].

Capsule #	Barrier	Cladding Type	Specimen Per Capsule	Capsule Length [cm]	Capsule Dia. [cm]	Cladding Thickness [cm]	Fuel Outside Diameter [cm]	Fuel Inside Diameter [cm]	Fuel Length [cm]	Density [% TD]	Enrichment [% U-235]	Carbon [ppm]	Oxygen [ppm]
Reference	5 mil Tungsten	T-111	6	11.430	1.900	0.147	1.580	0.510	5.720	94.0	5		
Reference					1.810	0.102							
Half	3 mil Tungsten				0.950	0.074	0.787	0.280			8		
Half					0.905	0.051							
Special	5 mil Tungsten		1						38.1		5		

Table XVIII. UN irradiation data for irradiation tests conducted at Plum Brook [61].

Specimen #	Irradiation Time [hr] (days)	Nominal Cladding Temp. [K]	Average Fuel Temp. [K]	Power Density [kW/cc]	Fluence [n/cm^2]	Burnup [%FIMA]	Fission Gas Release [%]	Max Dia. Swelling [%]	Change in Density [%]
Reference	8070 (336.25)	1263	1367	0.141	2.7E+20	0.468	0.05	-	2
Half			1254	0.288	3.1E+20	0.785	0.02	0.711	2.1
Half			1257	0.288	3.1E+20	0.78	0.02	0.55	1.9

Table XIX. Capsule and UN fuel data for irradiation tests conducted at Plum Brook [60].

Capsule #	Fuel Pin #	Barrier	Cladding Type	Specimen Per Capsule	Capsule Length [cm]	Capsule Dia. [cm]	Cladding Thickness [cm]	Fuel Outside Diameter [cm]	Fuel Inside Diameter [cm]	Fuel Length [cm]	Density [% TD]	Enrichment [% U-235]	Carbon [ppm]	Oxygen [ppm]
001	**504B**	5 mil Tungsten	T-111	6	11.430	1.810	0.102	1.580	0.510	5.720	94.0	5		
	503B	3 mil Tungsten				0.905	0.051	0.787	0.280			8		
	503C													
004	**502B**	5 mil Tungsten				1.900	0.147	1.580	0.510			5		
	501D	3 mil Tungsten				0.950	0.074	0.787	0.280			8		
	501F					0.950	0.074							
005	**502C**	5 mil Tungsten				1.900		1.580	0.510			5		
	501C	3 mil Tungsten				0.950	0.074	0.787	0.280			8		
	501E					0.950	0.074							
003	**504E**	5 mil Tungsten				1.810	0.102	1.580	0.510			5		
	503D	3 mil Tungsten				0.905	0.051	0.787	0.280			8		
	503E													
006	**504D**	5 mil Tungsten				1.810	0.102	1.580	0.510			5		
	503F	3 mil Tungsten				0.905	0.051	0.787	0.280			8		
	503H													
002	**502A**	5 mil Tungsten				1.900	0.147	1.580	0.510			5		
	501A	3 mil Tungsten				0.950	0.074	0.787	0.280			8		
	501B					0.950	0.074							
010	**503I**	3 mil Tungsten				0.905	0.051							
	503G													
011	**505E**	3 mil Tungsten												
	505F													
012	**507C**	3 mil Tungsten				0.950	0.074							
	507D					0.950	0.074							
013	**509A**	3 mil Tungsten				0.905	0.051							
	509B													
020	**510A**	5 mil Tungsten		1		1.900	0.147	1.580	0.510	38.1		5		
030	**505A**	3 mil Tungsten		6	11.43	0.905	0.051	0.787	0.280	5.72		8		
	505B													

Table XX. UN irradiation data for irradiation tests conducted at Plum Brook [60].

Capsule #	Irradiation Time [hr] (days)	Nominal Cladding Temp. [K]	Average Fuel Temp. [K]	Power Density [kW/cc]	Fluence [n/cm^2]	Burnup [%FIMA]	Fission Gas Release [%]	Max Dia. Swelling [%]	Irradiation Time [hr] (days)	Change in Density [%]
001	**504B**	8070	1263	1367	0.141	3.10E+20	0.47***	0.02	0.1	2****
	503B*			1257	0.282	3.10E+20	0.78***	0.05	0.445	2.1
	503C			1254		2.70E+20	0.78***	0.02	0.386	1.9
004	**502B**	883		1354	0.141	4.30E+20	-	-	-	-
	501D	12100		1329	0.282	4.30E+20	1.3	-	-	-
	501F*			1323		3.70E+20	1.36***	0.1	-	-
005	**502C**	19386		1362	0.141	4.00E+20	-	-	0.45	-
	501C	11623		1274	0.282	4.00E+20	1.1	-	-	-
	501E			1269			1.1	-	-	-
003	**504E**	13000		1332	0.141	3.90E+20	0.77***	-	-	-
	503D*			1313	0.282	3.90E+20	1.46***	0.09	-	-
	503E*			1297		2.90E+20	1.46***	0.09	1	5.3****
006	**504D**	6650		1343	0.141	2.40E+20	0.38	-	-	-
	503F			1281	0.282	2.40E+20	0.66	-	-	-
	503H			1225		2.10E+20	0.61	-	-	-
002	**502A***	6930		1322	0.141	2.50E+20	0.4***	0.03	-	-
	501A			1348	0.282	2.50E+20	0.76	-	-	-
	501B			1344		2.20E+20	0.75	-	-	-
010	**503I****	8750		1347	0.564	8.10E+20	2.16***	1.29	2.22	-
	503G**	8163		1323		7.60E+20	2.34***	0.18	-	-
011	**505E***	7091		1284		6.40E+20	1.85***	0.22	0.97	-
	505F*			1298		7.20E+20	1.85***	1.91	-	-
012	**507C**	7323		1342		7.00E+20	1.41	-	-	-
	507D*			1338		7.00E+20	1.94***	0.22	1	4.1****
013	**509A***	7065		1329		6.70E+20	1.88***	0.088	-	-
	509B*			1342		6.70E+20	1.88***	0.13	0.74	2.1****
020	**510A**	1990		1318	0.141	5.00E+19	0.11	-	-	-
030	**505A***	1147		1252	0.282	1.10E+20	0.22	0.15	-	-
	505B			1259		1.10E+20	0.21	-	-	-

*Fuel Pin Leak
**Cladding Crack
*** Gamma scan versus calorimetric calculation
**** Only measured one pellet due to pellet failure

Table XXI. Capsule and UN fuel data for irradiation tests conducted at ORNL [56, 62].

Capsule #	Fuel Pin #	Barrier	Cladding Type	Specimen Per Capsule	Capsule Length [cm]	Capsule Dia. [cm]	Cladding Thickness [cm]	Fuel Outside Diameter [cm]	Fuel Inside Diameter [cm]	Fuel Length [cm]	Density [% TD]	Enrichment [% U-235]	Carbon [ppm]	Oxygen [ppm]
UN-4	10	3 mil Tungsten	T-111	8	11.43	0.953	0.145	0.78	0	7.62	85.9	19.86	330	950
	11			9					0		84.4	10.96	120	1270
	12			8					0.23		94.1	10.96	280	900
UN-5	13			8					0		86.1	19.86	330	1010
	14			8					0.23		94.1	10.96	380	970
	15			9					0		84.4	10.96	170	1330

Table XXII. UN irradiation data for irradiation tests conducted at ORNL [56, 62].

Capsule #	Irradiation Time [hr] (days)	Nominal Cladding Temp. [K]	Average Fuel Temp. [K]	Power Density [kW/cc]	Fluence [n/cm^2]	Burnup [%FIMA]	Fission Gas Release [%]	Max Dia. Swelling [%]	Irradiation Time [hr] (days)	Change in Density [%]
UN-4	10*	10480	1263	Not Provided	.282 -.302	4.3E+20 - 8.6E+20	2.87	-	0.2	-
	11						2.76***	4.3	0.3	1.83
	12**						2.74	-	1.5	-
UN-5	13	10037					2.79	-	0.2	-
	14**						3.11***	-	3.7	16.7
	15*						2.72	-	0.4	-

*Fuel pin leak
**Cladding crack
***Gamma scan versus calorimetric calculation

Table XXIII. Capsule and UN fuel data for irradiation tests conducted at Plum Brook [72].

Fuel Pin #	Barrier	Cladding Type	Specimen Per Capsule	Capsule Length [cm]	Capsule Dia. [cm]	Cladding Thickness [cm]	Fuel Outside Diameter [cm]	Fuel Inside Diameter [cm]	Fuel Length [cm]	Density [% TD]	Enrichment [% U-235]	Carbon [ppm]	Oxygen [ppm]
323A	None	304L SS	4		0.533	0.076	0.381	0	2.54	94.3	10	210 - 460	980 - 1900
323B													
323C													
323D													
323E													
323F													

Table XXIV. UN irradiation data for irradiation tests conducted at Plum Brook [72].

Fuel Pin #	Irradiation Time [hr] (days)	Nominal Cladding Temp. [K]	Average Fuel Temp. [K]	Power Density [kW/cc]	Fluence [n/cm^2]	Burnup [%FIMA]	Fission Gas Release [%]	Max Dia. Swelling [%]	Volumetric Swelling [%]
323A	3797	1185	1219	0.93	3.42E+20	1.858 / 1.755*	-	2.14 / 2.53*	-
323B		1113	1155	1.178		2.155	-	-	-
323C		1262	1306	1.218		2.23	-	-	-
323D		1155	1189	0.944		1.729	-	-	-
323E		1079	1106	0.735		1.347	-	-	-
323F	2844	1142	1168	0.724	2.56E+20	0.948**	-	0.6**	1.96**

*First measurement is for pellet number 1 at a fuel temperature of 1265 K and second value is for pellet number 3 at a fuel temperature of 1306 K

**Value is for fuel pellet number 3 at a fuel temperature of 1222 K

3.3.4. SP-100

The SP-100 program began in the early 1980's as a joint effort project between the Department of Defense (DOD) Strategic Defense Initiative Office (SDIO) and U.S. National Aeronautics and Space Administration (NASA) [88-92]. The final version of the SP-100 concept was a UN fueled, lithium-cooled fast-spectrum reactor that would supply approximately 100 kW electric of power. The UN fuel pin was selected to be cladded by PWC-11 (Nb – 1%Zr – 0.1%C) with a rhenium lining. Rhenium was more chemically inert with the fuel and the associated fission products, while PWC-11 was more compatible with lithium [88].

At the time, there was limited UN development as well as UN fuel performance data. The SP-100 program was developed to address a few major issues pertaining to UN: high-temperature UN fuel swelling and fuel/cladding compatibility [93]. LANL supplied high quality UN fuel pellets which were later tested and fully qualified in the Experimental Breeder Reactor II (EBR-II) and the Fast Flux Test Facility (FFTF) reactors. EBR-II was a sodium cooled fast reactor operating at the Argonne National Laboratory (ANL) and the FFTF operated at the Hanford Site for the DOE. The SP-100 testing program developed a few breakthrough technologies: hot isostatic pressing procedure for UN fuel, characterization of the fission gas release versus burnup and material stress versus strain behavior [88].

The remaining focus of this section will be on the post-irradiation data collected on UN during the SP-100 program. A total of 86 experimental fuel pins were irradiated as part of the SP-100 program with a goal burnup of approximately 6 %FIMA. All irradiation tests were performed with a goal peak cladding temperature of 1200 or 1500 K [57]. With the design gas gap thickness and a peak cladding temperature of 1500 K, the project fuel centerline temperature was approximately 1950 K [57]. The SP-100 testing program was split into four major testing groups: SP-1/Reconstitution (R), SP-2, SP-3/R/RR and FSP-1/R/RR. These testing groups were performed in order, and all were designed with specific criteria in mind.

The following is a summary of the significant aspects of each test and is also summarized in Table XXV [91]:

SP-1: The first series of tests and was performed at EBR-II. SP-1 comprised of eight fuel rods, four contained UN while the other four contained UO_2. The four UN fuel pins were 87% TD UN with a PWC-11 cladding and a free-standing vapor deposited (CVD) tungsten liner. The UN fuel pins were irradiated for 96 effective full power days. These rods achieved a burnup up to 0.83 %FIMA. Two UN fuel pins went on to continue testing at EBR-II. This test was renamed SP-1 Reconstitution or SP-1R. In SP-1R, two additional fresh UN fuel pins were added comprised of 87% TD UN with a PWC-11 cladding and tungsten liner. These fuel pins were irradiated for 400 full power days. The original two fuel pins achieved up to 3.9 %FIMA burnup while the two new fuel pins achieved a burnup up to 3 %FIMA.

SP-2: Performed at EBR-II with four UN fuel pins and four UO_2 fuel pins. All four UN fuel pins contained 87% TD UN. Two UN fuel pins were lined with a free-standing CVD tungsten liner and clad with PWC-11 while the other two were clad with Mo-13Re. The four UN fuel pins were irradiated for 181 full power days. These fuel pins achieved a burnup up to 1.3 %FIMA.

SP-3: The first series of tests performed at EBR-II utilizing high density UN. All eight fuel pins contained 96% TD UN and cladded with PWC-11 with a free-standing CVD tungsten liner. These fuel pins were irradiated for 112 full power days. These fuel pins achieved a burnup of 0.8 %FIMA. Six of these fuel pins continued testing at EBR-II along with two fuel rods from SP-1. This test was re-named SP-3R. The eight fuel pins were irradiated for 469 full power days. Through the various tests, the two low density fuel pins were first to achieve the goal burnup of 6 at.%. The six fuel pins from SP-3 achieved a burnup up to 3.3 %FIMA. Four of the high-density fuel pins continued testing at EBR-II along with 4 fresh fuel pins. This test was named SP-3RR. The four new fuel pins were 96% TD UN. These fuel pins were clad with PWC-11 and lined with wrought rhenium. Two of these fuel pins had a bonded liner while the other two had free standing liners. These fuel pins were irradiated for 429 full power days. The original four fuel pins achieved the goal burnup up to 6 %FIMA while the four new fuel pins achieved a burnup up to 3.1 %FIMA.

FSP-1: A series of tests performed on 38 fuel pins at FTFF. These fuel pins comprised of fuel pellets with various geometries, densities, and enrichments. All fuel pins were clad with PWC-11 with free-standing CVD tungsten or rhenium liners. Two separate cladding outer diameters were used, 0.584 cm and 0.762 cm. Compared to the EBR-II tests, all 38 fuel pins were nearly twice as long. These fuel pins were irradiated for 269 full power days. Some higher enriched fuel pins achieved up to 2.3 %FIMA while some low enriched pins only achieved up to 0.5 %FIMA. 22 of the original 38 fuel pins continued testing at FTFF along with 16 fresh fuel pins. All 16 fresh fuel pins contained 96% TD UN. Fourteen of these new fuel pins were clad with Nb-1Zr and lined with either free standing or bonded wrought rhenium. Two of the new fuel pins were clad with bare rhenium. The original fuel pins achieved an accumulated burnup up to 5.6 %FIMA while the fresh fuel pins attained up to 3.1 %FIMA.

While limited data is available on the post irradiation testing of the SP-100 program, Matthews et al. provides a brief description of the testing performed on two fuel pins form the SP-1 test. Fuel pins NBU-2 and NBU-3 were operated for 96 equivalent full-power days at approximately 1 kW/cc. The fast spectrum fluence was approximately 1.2×10^{22} n/cm^2 achieving a burnup of approximately 0.8 %FIMA. The cladding temperature was approximated to be 1500 K, and a fuel centerline temperature of approximately 1950 K assuming a 0.25-mm gas gap between the fuel and cladding. Summarized testing information can be found in Tables XXVII and XXVIII below.

Post irradiation testing indicated that during testing, no fuel-clad interaction occurred. This was supported by the minimal cladding strain measured. After further investigation, the gas gap was measured to be 0.36 mm at BOL, causing approximately 100 K higher than first estimated. The elevated fuel temperature in the range causes rapid dissociation which was evident when performing a visual inspection of the fuel pellet. Coarse, irregular surfaces caused by surface vaporization was noted on the surface of the fuel pellets. This was also supported by the deposits on the tungsten liner and porous zones at the pellet interfaces.

Average dimensional change calculations for both fuel pins showed an average length increase of approximately 1.2% and an average diameter increase of approximately 3.6%. The anisotropic volumetric fuel swelling was approximately 8.6% yielding approximately 8% swelling per 1 %FIMA burnup for high temperature fast spectrum conditions. As seen in Figure 3.2, swelling data for SP-1 is significantly higher than the other swelling data. No concrete conclusion was drawn for the increase in swelling however it was noted that the SP-1 test occurred at higher operating temperatures. When comparing fission gas release, as seen in Figure 3.1, SP-1 fuel pins exhibit similar results as compared to other high temperature tests performed. For comparison, Table XXVI provides a breakdown of the differences in the fuel pins and operating conditions for the tests which SP-1 is compared to.

While specific data was not presented, various post irradiation examinations took place through the SP-100 program. As described by Makenas et al. [91], test series SP-3RR achieved unencumbered results out to approximately 6 %FIMA burnup. It was noted that for the higher density fuel, no pellet interface fusing took place including low disassociation.

Table XXV. SP-100 testing breakdown [91].

Test	Origin	Fuel Pins	TD [%]	Cladding	Liner	Irradiation Time (EFPD)	Burnup [%FIMA]
SP 1	New	4	87	PWC – 11	Free-standing CVD Tungsten	96	0.83
SP 1R	SP-1	2				496	3.9
	New	2				400	3
SP 2	New	2				181	1.3
	New	2		Mo – 13Re	None	181	1.3
SP 3	New	8	96	PWC – 11	Free-standing CVD Tungsten	112	0.8
SP 3R	SP-3	6	96			608	3.3
	SP-1/ SP-1R	2	87			965	6
SP 3RR	SP-3/ SP-3R	4	96		Free-standing CVD Tungsten	1037	6
	New	2			Bonded Wrought Rhenium	429	3.1
	New	2			Free Standing Wrought Rhenium	429	3.1
FSP 1	New	38	-	PWC – 11	Free-standing CVD Tungsten or Rhenium	-	2.3
FSP 1R	FSP 1	22	-	PWC – 11	Free Standing Wrought Rhenium	-	5.6
	New	16	-			-	3.1

Table XXVI. Comparison of key testing and fuel pin parameters [57].

	ORNL [64]	**CANEL [19]**	**SP-1**
Neutron Spectrum	Thermal	Thermal	Fast
Cladding	PWC-11	Nb-1Zr	Nb-1Zr
Liner	CVD Tungsten	CVD Tungsten	CVD Tungsten
Approximate Fuel Temp [K]	1460	1675	1950
Fuel Density [% TD]	95	93	87
Grain Size [μm]	40	-	17
Oxygen [ppm]	1000	950 – 2700	55
Carbon [ppm]	500	400	560

Table XXVII. Capsule and UN fuel data for irradiation tests conducted for the SP-1 testing program [57].

Capsule #	Barrier	Cladding Type	Specimen Per Capsule	Capsule Length [cm]	Capsule Dia. [cm]	Cladding Thickness [cm]	Fuel Diameter [cm]	Fuel Length [cm]	Density [% TD]	Enrichment [% U-235]	Carbon [ppm]	Oxygen [ppm]
NBU-2	5 mil Tungsten	PWC-11	12	16.27	0.762	0.0635	0.5842	7.62	87	-	560	55
NBU-3												
NBU-4												
NBU-5												

Table XXVIII. UN irradiation data for irradiation tests conducted SP-1 testing program [57].

Specimen #	Irradiation Time [hr] (days)	Nominal Cladding Temp. [K]	Average Fuel Temp. [K]	Power Density [kW/cc]	Fluence [n/cm^2]	Burnup [%FIMA]	Fission Gas Release [%]	Max Dia. Swelling [%]	Volumetric Swelling [%]
NBU-2	96	1500	1950	0.997	1.22E+22	0.74	5.35	3.5	8.9
NBU-3	96		1950		1.22E+22	0.81	7.5	3.7	8.3
NBU-4	96	1300	-		-	-	-	-	-
NBU-5	96		-		-	-	-	-	-

3.3.5. Battelle Research Reactor

During the late 1960's and early 1970's, Battelle Memorial Institute (BMI) conducted various tests with the goal to develop dimensionally stable fuels which may be used in high temperatures reactors. Among the various fuel types, UN was chosen as a possible fuel candidate. Testing was conducted at Battelle's research reactor (BRR), which the testing series was listed as HT-BRR. Battelle designed a high temperature capsule, able to irradiate up to six clad specimens at once up to 2250 K. During the first set of tests for UN, it was noted that when high density fuels are irradiated at temperatures near 1950 K, volume increases between 20 to 40 percent at burnups of only approximately 1 %FIMA. Once this rapid increase of volume takes place, the volume increase subsides and remains relatively constant. This phenomenon was coined "saturation of swelling". To better understand this phenomenon, additional tests were specifically designed to further investigate this phenomenon. Unless specified below, each capsule was clad in 0.0508 cm thick W – 25.5%Re with and outside diameter of 0.635 cm and contained multiple pellets or a single slug of fuel, 0.5334 cm in diameter and 2.54 cm in total length. Dimensional information for all the tests is shown in Table XXX at the end of this section.

As mentioned above, the most significant observation during the first set of tests on UN, HT-BRR-3, was saturation of swelling which is shown in Figure 3.16. As described by Hilbert et al. cited in Keller and Chubb [71], one UN fuels slug with 97 %TD was irradiated at a maximum fuel surface temperature of approximately 1950 K. It was noted that the diametral swelling became constant at approximately 10 percent and volumetric swelling became constant at approximately 20 percent. In addition to geometric measurements, metallographic composite photographs were taken. Analyzing grain boundaries and grain size, it is suggested that at least 75 percent of the porosity was interconnected. This helps provide some insight into a possible mechanism for saturation of swelling. Early in irradiation, gases quickly migrate to the grain boundary, coalescing, causing a rapid rise in specimen volume. Once the specimen reached approximately 20 percent swelling, it is thought that fission gas production and release reached an equilibrium, causing the volumetric increase to stabilize and become constant. Dimensional and irradiation data for HT-BRR-3 can be seen in Tables XXX and XXXI.

The next set of experiments defined by HT-BRR-4 was to investigate the effectiveness of various systems for promoting gas release during irradiation at high temperatures. As described by Hilbert et al. cited in Keller and Chubb [71], to analyze gas release effects, a 0.1397 cm diameter hole was placed at the center of two separate UN specimens, both consisting of 97 %TD. As shown in Figure 3.16, one sample exhibited saturation of swelling, however it occurred at a higher burnup and lower volumetric swelling, as compared to the sample in HT-BRR-3. As shown in Figure 3.16, specimen 292 is not considered typical beyond approximately 3 %FIMA burnup due to bulging and cracking of the cladding. No bulging or cracking was identified in

specimen 293. However, the initial and final centerline hole diameter was approximately equal. Since the centerline hole did not experience a significant amount of inward swelling (approximately the same as the outward increase), it is concluded that the centerline hole provides a small benefit to overall diametral swelling. Instead, it was concluded that the centerline hole allowed additional gas release from the fuel, reducing the overall swelling of the specimen. Free uranium deposits were found on the inside surface of specimen 292, indicating dissociation at high temperatures. It was determined that the localized crack in the center of the fuel caused a localized increase in temperature, above which UN begins to dissociate. Dimensional and irradiation data for HT-BRR-6 can be seen in Tables XXX and XXXI.

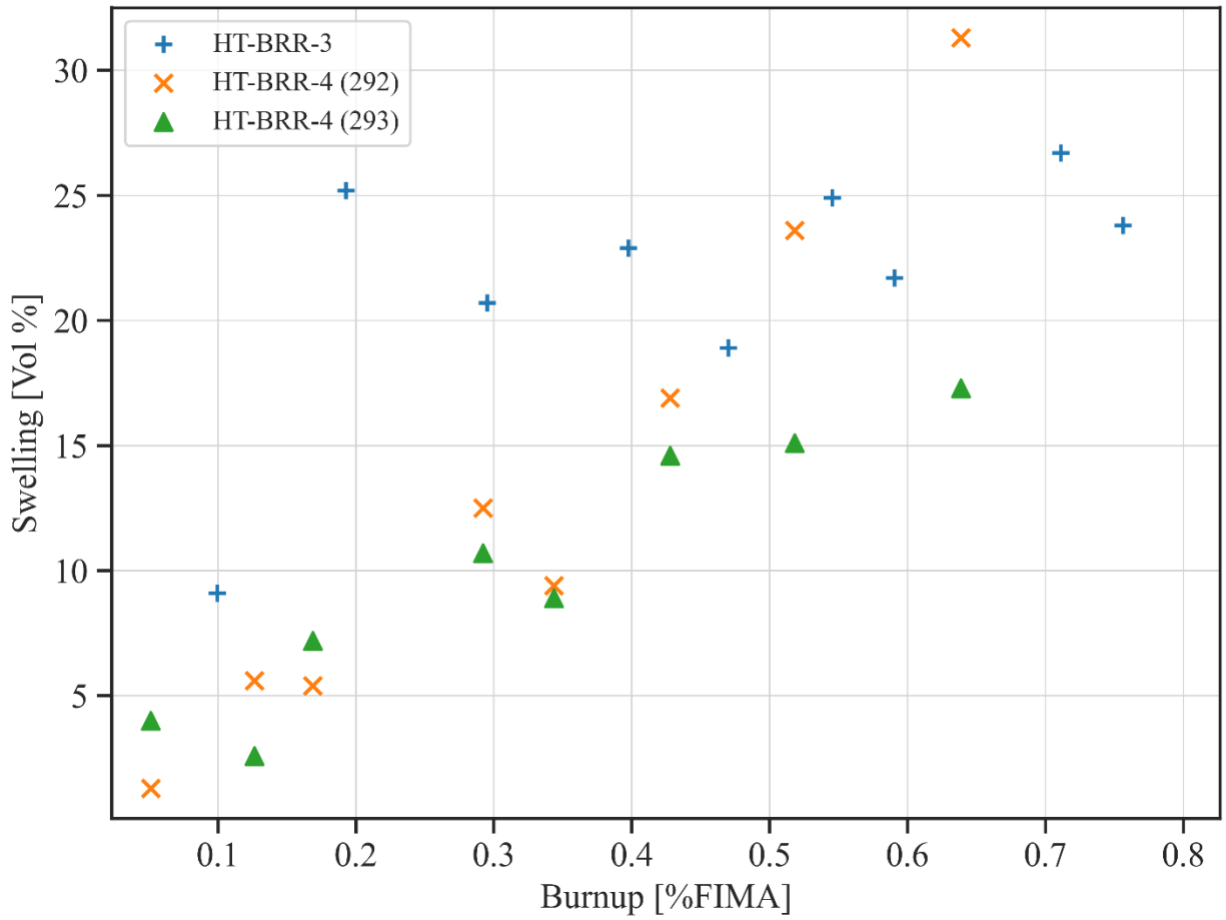

Figure 3.16. Comparison of the volumetric fuel swelling versus burnup for HT-BRR-3 and 4 [71].

The next test in the series for UN was HT-BRR-6, which focused on the effectiveness of cladding restraint on volumetric swelling during high temperature irradiation. As described by Hilbert et al. cited in Keller and Chubb [71], this was performed by varying the thickness and strength of the cladding material while maintaining the fuel specimen the same. Four capsules containing approximately 98 %TD UN with a 0.1397 cm hole were irradiated at approximately 1950 K. Two capsules were clad with twice the thickness of W-25.5% Re cladding (0.1016 cm)

and the remaining two are clad with on layer of high strength W-15% Re-20% Zr-20% carbon alloy and one layer of nominal W-25.5% Re cladding, with a total thickness of 0.1016 cm. As shown in Figure 3.17, a reduction in volumetric swelling was observed which was realized in the reduction of the centerline hole for both an increase in thickness as well as strength of the cladding. It was noted that up to 4% of the total diametral swelling was seen in the centerline hole, indicating that the increased strength of the cladding forced the swelling inward. However, it was concluded that the percent reduction of swelling may not be sufficient when compared to the potential reduction in neutron economy from the cladding. For comparison of the total volumetric swelling, specimen 293 from HT-BRR-4 and the specimens from HT-BRR-6 are shown in Figure 3.17. The first set of data for HT-BRR-6 is for the fuel pin with double the nominal cladding thickness while the second set of data is for the fuel pin with the additional layer of the stronger cladding. Dimensional and irradiation data for HT-BRR-6 can be seen in Tables XXX and XXXI.

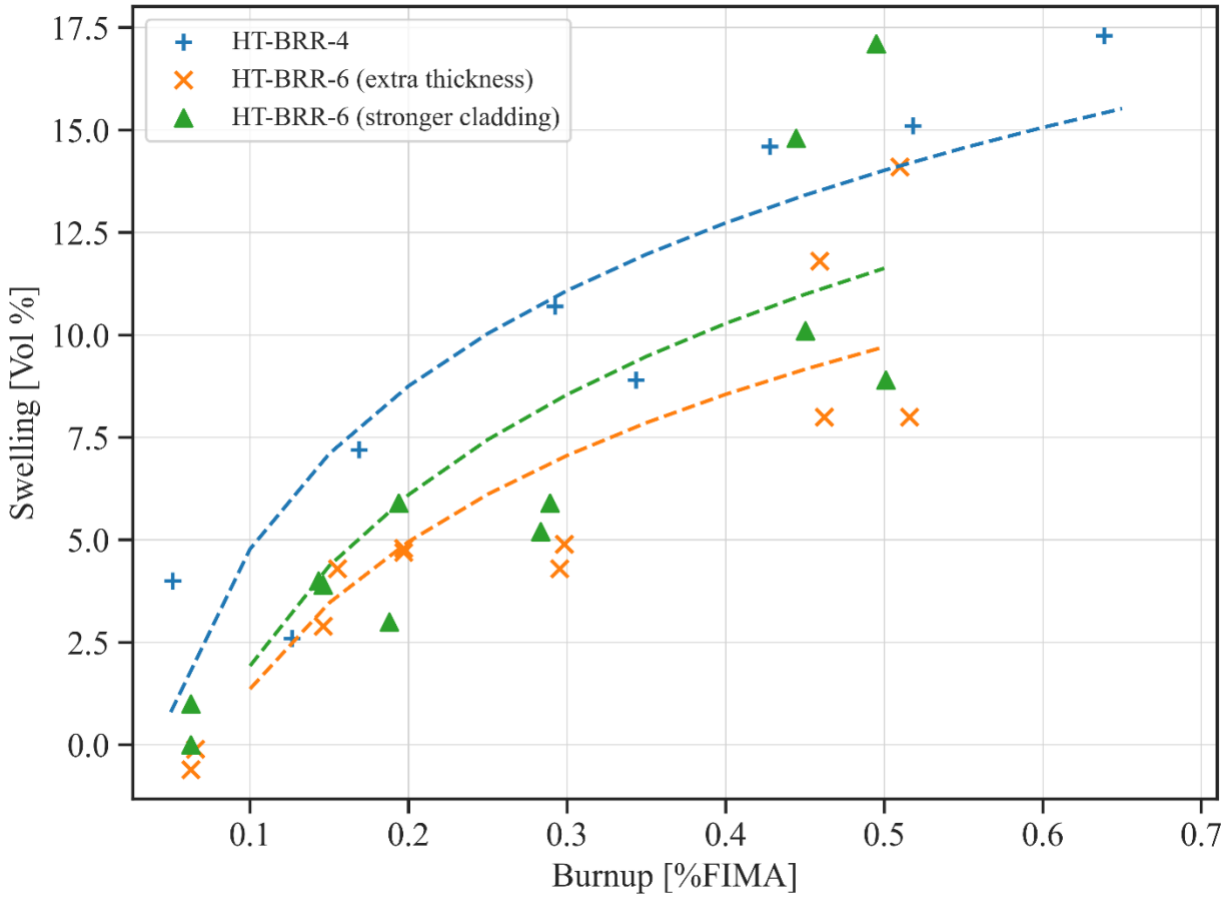

Figure 3.17. Comparison of the volumetric fuel swelling versus burnup for HT-BRR-4 and 6 [71].

The next test was HT-BRR-7, which was designed to test the impacts of a void space on dimensional changes of UN. As described by Hilbert et al. cited in Keller and Chubb [71], HT-

BRR-7 consisted of two 70 %TD UN specimens which was chosen to attempt to simulate the interconnected porosity which has been seen in the post examination of various high-density irradiated specimens. The most significant observation from this test was that the specimen was that up to approximately 0.3 %FIMA burnup, neither specimen exhibited saturation in swelling nor a significant increase in volume. Post irradiation data for the full fuel testing cycle was not available and therefore no other significant observations were noted for low density fuel. Dimensional and irradiation data for HT-BRR-7 can be seen in Tables XXX and XXXI.

The next test in the series was HT-BRR-8 which was designed to extend on the previous study by incorporating additional porosities, various fabrication mesh size and a radial gap between the cladding and fuel. As described by Hilbert et al. cited in Keller and Chubb [70], four specimens were irradiated as seen in Table XX. Two specimens were fabricated to achieve 85% TD and two were 92% TD using various meshes of UN powder. One sample from each density utilized minus 325 mesh powder while the other two samples were minus 100 combined with plus 200 mesh powder. The combination of powder was to vary the particle sizes of the UN samples. Both 92% TD specimen had an increased radial gap between the fuel and cladding which was set to 0.1524 cm. These variations in powder meshes combined with the radial gap was designed to simulate the interconnected porosity seen in the irradiated high-density samples in attempt to analyze saturation of swelling. The available data for this test series is for only one cycle therefore a trend of swelling is unavailable. However, as shown in Table XXX, the volumetric swelling was significantly higher for the higher density specimen which is contrary to the results seen in the low-density specimen in HT-BRR-6. Additionally, the swelling was significantly higher in the low-density fuel as compared to the high-density fuel. No conclusion was drawn for either case. Dimensional and irradiation data for HT-BRR-8 can be seen in Tables XXX and XXXI.

The next test of UN was HT-BRR-10, which was designed to help explain the effects of grain size, uniformly distributed porosity and temperature on swelling and gas-release behavior of UN. As described by Hilbert et al., cited in Keller [69], five UN samples were studied as shown in Table XXIX. Additionally, fission gas pressure was monitored on the 80 %TD specimen, 348. During irradiation, all specimens cladding experienced failure except for the large-grained specimen 350. It was noted that in the large grain specimen retained nearly all its fission gases and there was little growth of fission gas bubbles at the grain boundaries. This specimen was irradiated for a longer period and at a higher temperature than a fine-grained specimen, suggesting that a reduction in the grain-boundary bubble formation leads to improved dimensional stability. Additionally, this conclusion is identified when comparing the rapid volumetric increase of HT-BRR-3, where large formation of fission gases at the grain boundaries existed, to the slow increase in swelling in HT-BRR-7, where small fission gas bubbles were distributed within the grains. As observed in Figure 3.18, two samples (351 and 352) which operated at approximately 100 K higher temperatures than specimen 353, had a larger volumetric swelling, indicating that temperature has a direct impact on total swelling. There was no

substantial evidence to indicate why specimen 348, having lower density, experienced a much higher swelling compared to all other samples. The gas monitoring system on specimen 348 indicated approximately 15 percent gas release at the time of cladding failure which occurred at approximately 0.6 %FIMA. Dimensional and irradiation data for HT-BRR-10 can be seen in Tables XXX and XXXI.

Table XXIX. HT-BRR-10 fuel specimen characteristics [69].

Specimen Number	Design Fuel Surface Temperature [K]	Fuel Characteristics	U-235 Enrichment
348 (gas pressure monitor)	1950	Fine Grained – 80 %TD	20
350	1950	Cast – Large Grained	12
351	1950	Fine Grained – 99 %TD	10
352	1950	Fine Grained – 99 %TD	10
353	1500	Fine Grained – 99 %TD	10

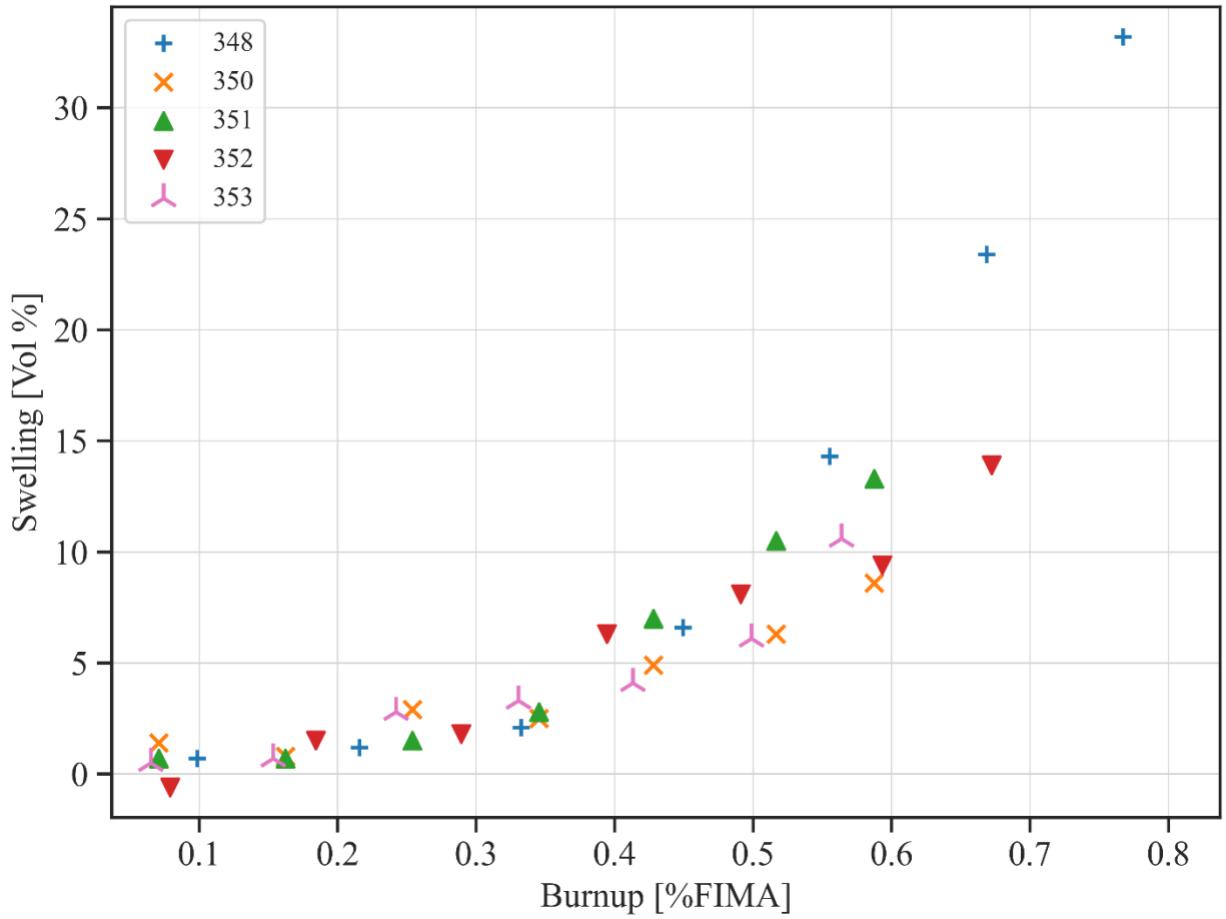

Figure 3.18. Volumetric swelling versus for test samples of the HT-BRR-10 test series [69].

The final test in this series was HT-BRR-13, which was designed to further investigate cladding restraint and fission gas release on the swelling of UN. As described by Hilbert et al.,

cited in Keller [70], capsule HT-BRR-13 contained three specimens of UN which were irradiated at approximately 1975 K. Two of the specimens were 93% TD UN, one with a nominal cladding and the other containing axial cutes every 90 degrees. The third specimen was 73% TD UN, containing a gas monitor system. The results from gas-pressure monitoring of the high porosity UN specimen indicated that negligible fission gas release existed until approximately 0.1 %FIMA burnup, which at this point of irradiation, the fission gas release increased rapidly until transducer failure. It was estimated the cumulative fission gas release was 65 percent at approximately 0.5 %FIMA. When comparing the gas release between these results and those in HT-BRR-10, it was determined that an increase in porosity will decrease the time delay before gas release occurs, increase the gas release rate after the delay and increase the total cumulative gas release. Due to the known abnormalities in the slit cladding, no dimensional measurements were taken. Dimensional and irradiation data for HT-BRR-13 can be seen in Tables XXX and XXXI.

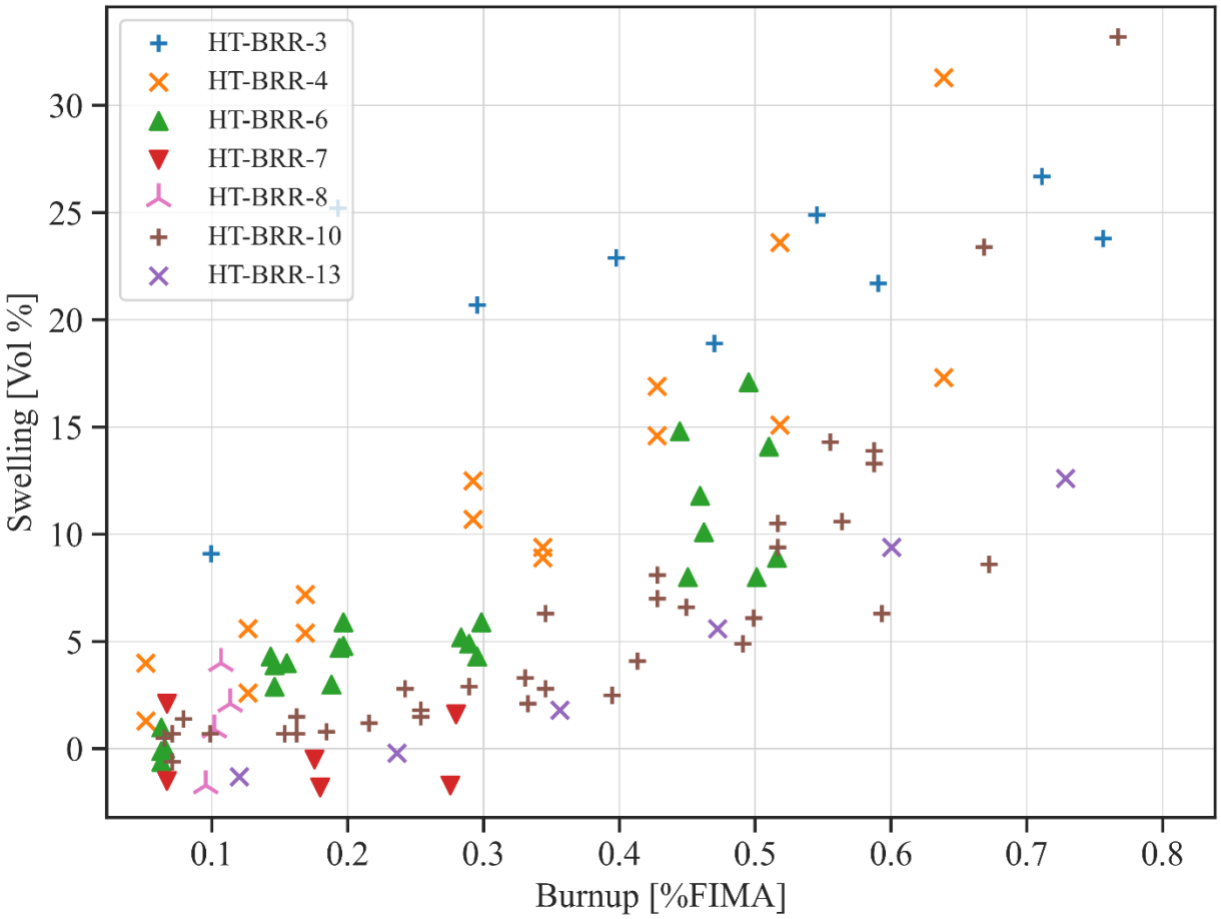

Figure 3.19. UN volumetric swelling versus burnup for all Battelle testing series [69-71].

In conclusion, two different types of swelling behavior were noted during Battelle's UN high temperature testing program. One is categorized as saturation of swelling, where the UN fuel rapidly increases in volume until the fission gas production is in equilibrium with the fission gas

release. It is suggested that this occurs when fission gases migrate and coalesce at the grain boundaries of the UN fuel, causing a high degree of interconnected porosity. The second is seen as a lower swelling rate caused by low mobility of fission gases, causing a gradual increase in volume throughout irradiation. This was also suggested to be due to fission gas accumulation at the grain boundaries, however it only included a small portion of the total fission gases in the material. Overall, it was determined that fuel swelling was minimized by reducing the overall grain boundaries within UN. Additionally, it is evident that temperature has a direct impact on the overall swelling behavior of UN as does a central hole and an increase in cladding strength.

Table XXX. Capsule and UN fuel data for irradiation tests conducted during the Battelle testing program [69-71].

Capsule #	Specimen #	Cladding Type	Capsule Dia. [cm]	Cladding Thickness [cm]	Fuel Outside Diameter [cm]	Fuel Inside Diameter [cm]	Fuel Length [cm]	Density [% TD]	Enrichment [% U-235]
HT-BRR-3	288	W-25.5% Re	0.635	0.0508	0.5334	0	2.54	97	8.5
HT-BRR-4	292	W-25.5% Re	0.635	0.0508	0.5334	0.1397	2.54	97	8.5
	293		0.635	0.0508					
HT-BRR-6	314B	W-25.5% Re	0.6858	0.1016	0.5334	0.1397	2.54	98	8.5
	316		0.6858	0.1016					
	317	W-20% Re-20% Zr-20% C w/ W-25.5% Re	0.635	0.1016					
	315B	W-20% Re-20% Zr-20% C w/ W-25.5% Re	0.635	0.1016					
HT-BRR-7	322	W-25.5% Re	0.635	0.0508	0.5334	0	2.54	70	8.5
	323		0.635	0.0508					
HT-BRR-8	330	W-25.5% Re	0.635	0.0508	0.5334	0	2.54	85	8.5
	331		0.635					85	
	336		0.7366					92	
	337		0.7366					92	
HT-BRR-10	348	W-25.5% Re	0.635	0.0508	0.5334	0	2.54	80	20
	351							99	10
	352							99	10
	350							-	12
	353							99	10
HT-BRR-13	371	W-25.5% Re	0.635	0.0508	0.5334	0	2.54	73	8.5
	382							93	
	380							93	

Table XXXI. UN irradiation data for high temperature irradiation tests conducted for the Battelle testing program [69-71].

Capsule #	Specimen #	Irradiation Time [hr] (days)	Irradiation Cycle	Max Fuel Temp. [K]	Power Density [kW/cc]	Burnup [%FIMA]	Avg. Dia. Swelling [%]	Avg. Length Swelling [%]	Volumetric Swelling [%] *
HT-BRR-3	288**	-	1	1918	0.46	0.0994117	3.7	1.7	9.1
			2	1918		0.1927984	11.2	2.8	25.2
			3	1968		0.2952225	9.2	2.3	20.7
			4	1938		0.3976467	10.1	2.7	22.9
			5	1868		0.469946	8	2.9	18.9
			6	1953		0.5452579	11	2.9	24.9
			7	1973		0.590445	9.4	2.9	21.7
			8	1978		0.710944	11.7	3.3	26.7
			9	1978		0.7561311	10.1	3.6	23.8
HT-BRR-4	292***	3200 (133.33)	1	1838	0.46	0.0512146	0.1	1.1	1.3
			2	1903		0.1265302	2.1	1.4	5.6
			3	1898		0.168707	2	1.4	5.4
			4	1968		0.2922246	4.6	3.3	12.5
			5	1898		0.3434392	3.9	1.6	9.4
			6	1898		0.4277927	6.7	3.5	16.9
			7	1913		0.5181715	9.1	5.4	23.6
			8	1898		0.6386764	13.2	4.9	31.3
	293		1	1813		0.0512146	2	0	4
			2	1933		0.1265302	1	0.6	2.6
			3	1913		0.168707	3.4	0.4	7.2
			4	1958		0.2922246	5.3	0.1	10.7
			5	1898		0.3434392	3.7	1.5	8.9
			6	1913		0.4277927	5.9	2.8	14.6
			7	1913		0.5181715	6.2	2.7	15.1
			8	1898		0.6386764	6.5	4.3	17.3

* Volumetric swelling is calculated by 2 x (Diameter Swelling) + (Length Swelling)
** Saturation of swelling
*** Cladding rupture

Table XXXI (cont.). UN irradiation data for high temperature irradiation tests conducted for the Battelle testing program [69-71].

Capsule #	Specimen #	Irradiation Time [hr] (days)	Irradiation Cycle	Max Fuel Temp. [K]	Power Density [kW/cc]	Burnup [%FIMA]	Avg. Dia. Swelling [%]	Avg. Length Swelling [%]	Volumetric Swelling [%] *
HT-BRR-6	314B	2600 (108.33)	1	1913	0.46	0.0626196	0.2	0.6	1
			2	1898		0.1461123	1.8	0.3	3.9
			3	1853		0.1878587	0.8	1.4	3
			4	1863		0.2832789	2.2	0.8	5.2
			5	1878		-	-	-	-
			6	1913		0.4443007	6.8	1.2	14.8
			7	1913		0.4949927	8	1.1	17.1
	316		1	1938		0.0656014	-0.1	0.2	0
			2	1948		0.155058	1.9	0.2	4
			3	1903		0.1968043	2.2	1.5	5.9
			4	1918		0.2981884	2.4	1.1	5.9
			5	1933		-	-	-	-
			6	1923		0.462192	4.7	0.7	10.1
			7	1918		0.5158659	3.7	1.5	8.9
	317		1	1918		0.0626196	-0.7	0.8	-0.6
			2	2018		0.1461123	1	0.9	2.9
			3	1968		0.1968043	1.6	1.6	4.8
			4	1988		0.2952065	1.6	1.1	4.3
			5	1998		-	-	-	-
			6	1978		0.4592101	5	1.8	11.8
			7	1968		0.5099021	5.7	2.7	14.1
	315B		1	1903		0.0626196	-0.2	0.3	-0.1
			2	1988		0.1431304	1.9	0.5	4.3
			3	1948		0.1938224	1.9	0.9	4.7
			4	1958		0.2892427	2.3	0.3	4.9
			5	1958		-	-	-	-
			6	1908		0.4502644	3.9	0.2	8
			7	1898		0.5009565	3.5	1	8
HT-BRR-7	322	-	1	1893	0.46	0.0667942	1	0.1	2.1
			2	1948		0.1795094	-0.9	0	-1.8
			3	1968		0.2797007	0.6	0.4	1.6
	323		1	1943		0.0667942	-0.4	-0.7	-1.5
			2	1923		0.1753348	-0.2	-0.1	-0.5
			3	1983		0.2755261	-0.8	-0.1	-1.7
HT-BRR-8	330	-	1	2078	0.46	0.106576	2	0	4
	331		1	2088		0.1134519	0.6	0.9	2.1
	336		1	2173		0.1016433	0.1	0.7	0.9
	337		1	1928		0.0952906	-0.3	-1.1	-1.7

* Volumetric swelling is calculated by 2 x (Diameter Swelling) + (Length Swelling)

Table XXXI (cont.). UN irradiation data for high temperature irradiation tests conducted for the Battelle testing program [69-71].

Capsule #	Specimen #	Irradiation Time [hr] (days)	Irradiation Cycle	Max Fuel Temp. [K]	Power Density [kW/cc]	Burnup [%FIMA]	Avg. Dia. Swelling [%]	Avg. Length Swelling [%]	Volumetric Swelling [%] *
HT-BRR-10	348**	-	1	2018	0.46	0.0986258	0.2	0.3	0.7
			2	1948		0.2155156	0.2	0.8	1.2
			3	1948		0.3324055	0.7	0.7	2.1
			4	1998		0.4492953	2.8	1	6.6
			5	2048		0.5552267	5.9	2.5	14.3
			6	2023		0.6684638	10.2	3	23.4
			7	1998		0.7670896	14.5	4.2	33.2
	351**		1	1848		0.0708423	0.3	0.1	0.7
			2	1878		0.162347	0	0.7	0.7
			3	1898		0.2538517	0.5	0.5	1.5
			4	1938		0.3453563	1.1	0.6	2.8
			5	1938		0.4280057	2.6	1.8	7
			6	1923		0.5165586	4.4	1.7	10.5
			7	1923		0.587401	5.4	2.5	13.3
	352**		1	1848		0.0708423	-0.4	0.2	-0.6
			2	1878		0.162347	0.3	0.9	1.5
			3	1898		0.2538517	0.6	0.6	1.8
			4	1938		0.3453563	2.4	1.5	6.3
			5	1938		0.4280057	3.1	1.9	8.1
			6	1923		0.5165586	3.8	1.8	9.4
			7	1923		0.587401	5.8	2.3	13.9
	350		1	1898		0.0789006	0.4	0.6	1.4
			2	1963		0.1841015	0	0.8	0.8
			3	1988		0.2893024	0.9	1.1	2.9
			4	1958		0.3945032	0.6	1.3	2.5
			5	1968		0.4909373	1.7	1.5	4.9
			6	1918		0.5932159	2.3	1.7	6.3
			7	1898		0.6721166	3.2	2.2	8.6
	353**		1	1758		0.0649388	0.1	0.3	0.5
			2	1838		0.1534917	-0.2	1.1	0.7
			3	1878		0.2420446	0.8	1.2	2.8
			4	1858		0.3305975	1	1.3	3.3
			5	1868		0.4132469	1.3	1.5	4.1
			6	1818		0.4988481	2.2	1.7	6.1
			7	1803		0.5637869	4.4	1.8	10.6

* Volumetric swelling is calculated by 2 x (Diameter Swelling) + (Length Swelling)
**Cladding rupture

Table XXXI (cont.). UN irradiation data for high temperature irradiation tests conducted for the Battelle testing program [69-71].

Capsule #	Specimen #	Irradiation Time [hr] (days)	Irradiation Cycle	Max Fuel Temp. [K]	Power Density [kW/cc]	Burnup [%FIMA]	Avg. Dia. Swelling [%]	Avg. Length Swelling [%]	Volumetric Swelling [%] *
HT-BRR-13	371	-	1	1988	0.46	0.1036926	-	-	-
			2	1998		0.2011008			
			3	1998		0.3047934			
			4	1978		0.4053438			
			5	2038		0.5153208			
			6	2028		0.6252978			
	382		1	1958		0.1200923	-0.5	-0.3	-1.3
			2	1973		0.2361815	-0.2	0.2	-0.2
			3	1988		0.3562738	0.5	0.8	1.8
			4	1948		0.4723631	2.3	1	5.6
			5	2013		0.6004615	3.8	1.8	9.4
			6	2023		0.72856	5	2.6	12.6
	380		1	1873		0.1080831	-	-	-
			2	1873		0.2121631			
			3	1848		0.3202461			
			4	1828		0.4243261			
			5	1878		0.5404154			
			6	1878		0.6565046			

* Volumetric swelling is calculated by 2 x (Diameter Swelling) + (Length Swelling)

3.3.6. Lawrence Radiation Laboratory

During the same time that Battelle was performing irradiation testing on UN, Lawrence Radiation Laboratory (LRL) began a nuclear fuel testing program for their Space Electric Power Program. It was decided at the time, for cycle thermodynamics, a high temperature fuel was required, and UN was chosen as the fuel candidate. At this temperature, LRL determined that fuel swelling was going to be a potential limiting factor, however little information and testing had been conducted. LRL developed a fuel testing program to address some of the unknowns such as bubble formation, growth, and movement. These tests consisted of UN samples of various consistencies, all of which were clad with W-25.5% Re. It was thought that tungsten would provide additional strength to withstand any additional swelling at high temperatures.

The testing series established specific testing criteria to address the above concerns. The conditions were as follows [73, 74]:

- Several microstructures were to be compared, including single crystal, large-grain high-density, small-grain high density and approximately 75% dense uranium nitride.
- Specimen surface temperature from 1575 to 2075 K.
- Radial temperature profile limited to less than 325 K.
- Up to 6% total uranium burn-up.
- Annular specimen design was to be used to permit fission gas release and inner wall (centerline) temperature measurement.
- Nitrogen cover gas to be maintained at a fixed partial pressure and temperature to keep constant uranium thermodynamic activity and to prevent UN dissociation.
- Optimum specimen design was to be free standing or clad specimens which would allow approximately 30% unrestrained radial and axial growth.
- Specimen inner to outer radius burn-up ratio to be greater than 0.8 to approximate fast reactor conditions.
- Retention of fission gas from individual sample of secondary interest.
- Eight or more individual samples per capsule.

To accomplish the desired UN testing, LRL coordinated with Battelle for the design, construction, and irradiation of the UN capsules.

As described by Albrecht et al. [73, 74], the initial testing series was designated LRL-1, which contained four different grain sized samples each with 10% enrichment, shown in Table XV.

Table XXXII. Microstructure for LRL-1 capsule specimens [73, 74].

Specimen Number	Fuel Characteristics	Density [% TD]
1-C	Fine grain (30μ)	96
2-A	Single-Crystal, high-density	100
3-B	Single-Crystal, high-density	100
4-D	Fine grain (30μ)	78
5-E	Fine grain (30μ)	78
6-G	Fine grain (30μ)	96
7-H	Coarse grain (105μ)	97
8-I	Coarse grain (105μ)	97

Two samples for each grain size formed cylindrical fuel specimens, 0.508 cm diameter and 0.254 cm diameter central hole. The single crystals were stacked in three pieces, each 0.635 cm in length with the bottom piece remaining as a solid cylinder with no central hole. All other specimens were composed of either one or two sections, making up a total of 1.905 cm in length. The capsule was irradiated at approximately 1650 K for 3558 hours.

Post irradiation visual inspection indicated cladding cracking in all fuel specimens due to diametral swelling therefore the cladding provided no observable restraining effect. After the cladding was removed, no evidence of fuel breakage, cracking or crumbling occurred. Post irradiation swelling analysis indicated that low-density, fine-grained UN had lower overall swelling as compared to high-density, fine-grained UN. This was thought to be due to the accommodation of volume increase within the voids in the fuel. When comparing the low-density specimen to the single crystal specimen, it is thought that the lack of grain boundaries in the single crystal prevents fission gases to coalesce, which decreases the overall swelling. This conclusion supports the conclusions made during the Battelle high temperature testing. Additionally, when comparing the high-density specimens, the fine grain (30μ-diameter) specimen swelled more than the coarse grain specimen (105μ-diameter). As indicated by the irradiation results, the microstructure of the UN fuel plays a direct role in the volumetric swelling and generally, the fuel with less grain boundaries provides a lower volumetric swelling. Data comparison can be seen in Figure 3.20 and the dimensional and irradiation data for HT-BRR-13 can be seen in Tables XXXIII and XXXIV.

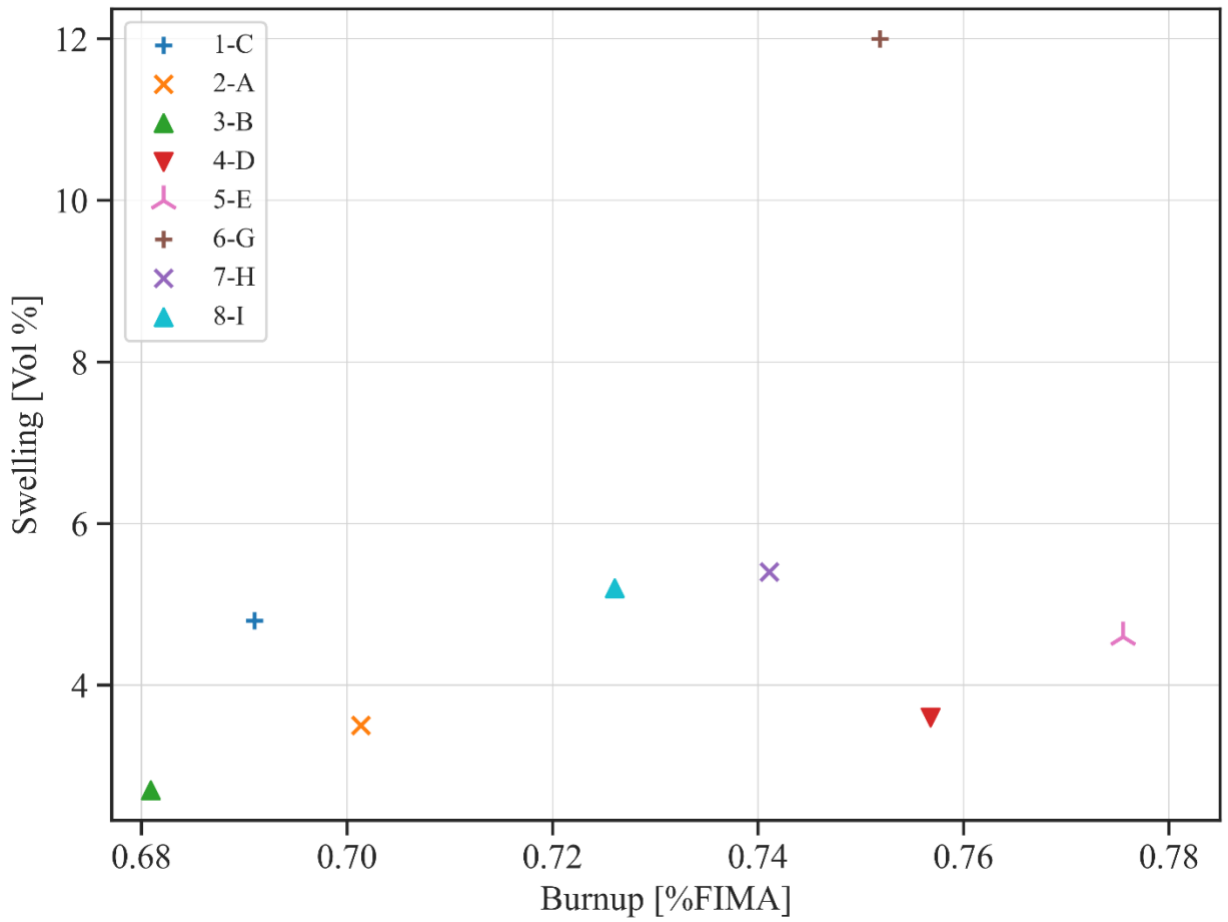

Figure 3.20. Volumetric swelling versus burnup for LRL-1 test specimens [73, 74].

The final test in the series was, LRL-2, which was designed to test volumetric swelling and fission gas release with varying grain size and porosity. Additionally, capsule LRL-2 operated with a nitrogen overpressure to determine whether increasing the stoichiometry of UN has an influence on fission gas mobility or release. All UN specimens shown in Table XXXII, were enriched to 10% U-235 and were cylindrical pellets with a 0.254 cm inner diameter, 0.508 cm outer diameter and 1.905 cm in length. Specimen O and L consisted of three pieces, while specimen P consisted of two. Two specimens had a 0.254 cm hole through two-thirds of the fuel pellet while the remaining portion was solid. All specimens were clad with the standard cladding from previous experiments. In comparison with all other UN testing in the LRL series or HT-BRR series, LRL-2 operated at a lower average irradiation temperature of approximately 1780 K as compared to temperatures exceeding 1900 K.

Table XXXIII. Microstructure for LRL-2 capsule specimens [70].

Specimen Number	Fuel Characteristics	Density [% TD]
O	Arc Melted	96, 96.5, 99
L	Arc Melted	96, 99, 97.5
J	Fine grain, high-density	98
K	Low density	75
M	Low density	75
N	Coarse grain, high density	98
P	Coarse grain, high density	98, 98

The initial inspection of all specimens indicated that all cladding was in excellent condition with no ruptures. Additionally, total diametral swelling of the cladding was less than one percent. Reviewing Figure 3.21, volumetric swelling was small in all fuel specimens. When comparing specimen N and P, which was irradiated at roughly 100 K higher temperature, the volumetric swelling was slightly higher. It was noted that the maximum fission gas release for any specimen was 5 percent, even with specimens K and M of 25% porosity, indicating that the lower temperature irradiation conditions reduced the fission gas mobility. When performing the metallographic examination, it was seen that fission-gas porosity existed at the grain boundaries of the higher density specimen in J and P. Generally, J and P experienced a larger amount of swelling which supports conclusion drawn during other irradiation testing programs. Dimensional and irradiation data for HT-BRR-13 can be seen in Tables XXXIV and XXXV.

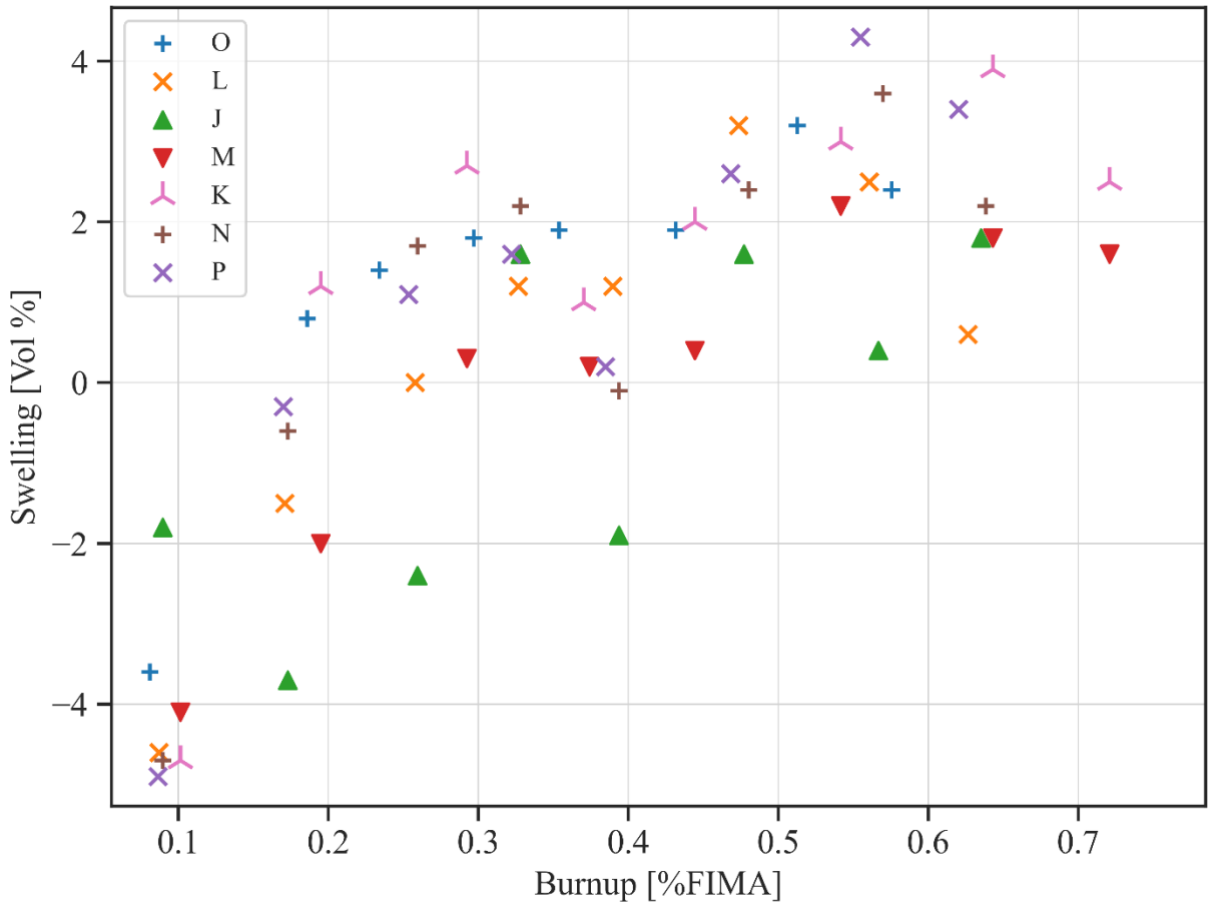

Figure 3.21. Volumetric swelling versus burnup for LRL-2 test specimens. Letters in the legend correspond to irradiation sample identification [70].

Table XXXIV. Capsule and UN fuel data for irradiation tests conducted during the LRL testing program [70].

Capsule #	Specimen #	Cladding Type	Capsule Dia. [cm]	Cladding Thickness [cm]	Fuel Outside Diameter [cm]	Fuel Inside Diameter [cm]	Fuel Length [cm]	Density [% TD]	Enrichment [% U-235]
LRL-1	1-C	W-25.5% Re	0.615	0.0508	0.508	0.254	1.905	96	9.6
	2-A							100	
	3-B							100	
	4-D							78	
	5-E							78	
	6-G							96	
	7-H							97	
	8-I							97	
LRL-2	O*	W-25.5% Re	0.615	0.0508	0.508	0.254**	1.905	96, 97.5, 99	10
	L							96, 99, 97.5	
	J*					0.254		98	
	K*							75	
	M*							75	
	N							98	
	P*							98, 98	

* 0.2286 cm diameter thermocouple at the cent of the fuel pellet

** Hole penetrates the top two fuel pellets

Table XXXV. UN irradiation data for high temperature irradiation tests conducted for the LRL testing program [70].

Capsule #	Specimen #	Cycle #	Irradiation Time [hr] (days)	Irradiation Cycle	Max Fuel Temp. [K]	Power Density [kW/cc]	Burnup [%FIMA]	Avg. Dia. Swelling [%]	Avg. Length Swelling [%]
LRL-1	1-C	-	3558 (148.25)	1590	0.46	0.69	2	0.1	4.8
	2-A			1661		0.70	0.7	1.4	3.5
	3-B			1674		0.68	0.4	1.7	2.7
	4-D			1632		0.76	0.7	0.3	3.6
	5-E			1649		0.78	0.9	0.4	4.6
	6-G			1688		0.75	3.1	0.1	12
	7-H			1642		0.74	2	0.6	5.4
	8-I			1658		0.73	1.5	1.6	5.2
LRL-2	O	1	-	1848	0.46	0.08	-2.6	1.6	-3.6
		2		1708		0.19	0	0.8	0.8
		3		1738		0.23	0.5	0.4	1.4
		4		1738		0.30	0.4	1	1.8
		5		1723		0.35	0.5	0.9	1.9
		6		1718		0.43	0	1.9	1.9
		7		1708		0.51	0.7	1.8	3.2
		8		1723		0.58	0.3	1.8	2.4
	L	1		1918		0.09	-2.6	0.6	-4.6
		2		1808		0.17	-1	0.5	-1.5
		3		1838		0.26	-0.5	1	0
		4		1838		0.33	0.2	0.8	1.2
		5		1833		0.39	0	1.2	1.2
		6		1828		0.47	0.9	1.4	3.2
		7		1818		0.56	0.6	1.3	2.5
		8		1828		0.63	0	0.6	0.6
	J	1		1888		0.09	-1.2	0.6	-1.8
		2		1748		0.17	-1.8	-0.1	-3.7
		3		1748		0.26	-0.9	-0.6	-2.4
		4		1768		0.33	0.2	1.2	1.6
		5		1753		0.39	-1.2	0.5	-1.9
		6		1748		0.48	0.2	1.2	1.6
		7		1738		0.57	-0.1	0.6	0.4
		8		1733		0.64	0.2	1.4	1.8
	M	1		1878		0.10	-2	-0.1	-4.1
		2		1768		0.19	-0.9	-0.2	-2
		3		1768		0.29	0.1	0.1	0.3
		4		1778		0.37	0.1	0	0.2
		5		1758		0.44	0.1	0.2	0.4
		6		1758		0.54	1	0.2	2.2
		7		1748		0.64	0.6	0.6	1.8
		8		1733		0.72	0.6	0.4	1.6
	K	1		1873		0.10	-2.6	0.5	-4.7
		2		1773		0.19	0.2	0.8	1.2
		3		1758		0.29	0.8	1.1	2.7
		4		1778		0.37	0	1	1
		5		1763		0.44	0.4	1.2	2
		6		1758		0.54	0.7	1.6	3
		7		1758		0.64	1.1	1.7	3.9
		8		1733		0.72	0.3	1.9	2.5
	N	1		1978		0.09	-2.4	0.1	-4.7
		2		1918		0.17	-0.4	0.2	-0.6
		3		1868		0.26	0.1	1.5	1.7
		4		1823		0.33	0.7	0.8	2.2
		5		1898		0.39	-0.3	0.5	-0.1
		6		1898		0.48	0.6	1.2	2.4
		7		1883		0.57	1	1.6	3.6
		8		1868		0.64	0.1	2	2.2
	P	1		1933		0.09	-2	-0.9	-4.9
		2		1878		0.17	-0.1	-0.1	-0.3
		3		1838		0.25	0	1.1	1.1
		4		1878		0.32	0.6	0.4	1.6
		5		1863		0.38	-0.6	1.4	0.2
		6		1848		0.47	1.1	0.4	2.6
		7		1828		0.55	1.4	1.5	4.3
		8		1803		0.62	0.8	1.8	3.4

4. Acknowledgements

This handbook was in part supported by the Laboratory Directed Research and Development program of LANL under project number 20220053DR “Accelerating Nuclear Fuel Qualification through Integrated Multiscale and Multiphysics Models”. This work was supported by the DOE through LANL. LANL is operated by Triad National Security, LLC, for the NNSA of the DOE (contract no. 89233218CNA000001). This paper is approved for unlimited release under LA-UR-XX-XXX.

References

[1] U.C. Nunez, D. Prieur, R. Bohler, D. Manara, Melting point determination of uranium nitride and uranium plutonium nitride: A laser heating study, Journal of Nuclear Materials 449(1-3) (2014) 1-8.

[2] R.S. Sen, M.A. Pope, A.M. Ougouag, K.O. Pasamehmetoglu, Assessment of possible cycle lengths for fully encapsulated microstructure fueled light water reactor concepts, Nuclear Engineering and Design 255 (2013) 310-320.

[3] C.P. Kempter, R.O. Elliott, Thermal Expansion of <UN>, <UO2>, <UO2·ThO2>, and <ThO2>, The Journal of Chemical Physics 30(6) (1959) 1524-1526.

[4] C.P. Kempter, J.C. McGuire, M.R. Nadler, Crystallographic data. 177. Uranium mononitride, Analytical Chemistry 31(1) (1959) 156-157.

[5] M. Uno, T. Nishi, M. Takano, 2.03 - Thermodynamic and Thermophysical Properties of the Actinide Nitrides, Comprehensive Nuclear Materials 2 (2012) 61-85.

[6] C.B. Carter, M.G. Norton, Ceramic Materials: Science and Engineering, Second ed., Springer2007.

[7] W.D. Callister, Fundamentals of Materials Science and Engineering, Fifth ed., John Wiley & Sons, Inc.2000.

[8] L. Van Brutzel, R. Dingreville, T. Bartel, Nuclear fuel deformation phenomena, State-of-the-art report on multi-scale modelling of nuclear fuels, 2015, pp. 59-79.

[9] R. Brennan, M. Golt, M. Ivill, Comparison of Dynamic Methods for Determining Elastic Property Measurements of Solid Materials, ARL-TR-9130, DEVCOM Army Research Lab., Aberdeen Proving Ground, MD, 2020.

[10] T. Honda, T. Kikuchi, Porosity Dependence of Elastic Modulus of Uranium Nitride, Journal of Nuclear Science and Technology 6(4) (1969) 221-222.

[11] A. Padel, C.H. deNovion, Constantes elastiques des carbures, nitrures et oxydes d'uranium et de plutonium, Journal of Nuclear Materials 33(1) (1969) 40-51.

[12] H. Whaley, W. Fulkerson, R. Potter, Elastic Moduli and Debye Temperature of Polycrystalline Uranium Nitride by Ultrasonic Velocity Measurements, Journal of Nuclear Materials 31(3) (1969) 345-350.

[13] A.R. Hall, Elastic moduli and internal friction of some uranium ceramics, Journal of nuclear materials 37(3) (1970) 314-323.

[14] H. Muta, K. Kurosaki, M. Uno, S. Yamanaka, Thermophysical properties of several nitrides prepared by spark plasma sintering, Journal of Nuclear Materials 389(1) (2009) 186-190.

[15] E.O. Speidel, D.L. Keller, Fabrication and properties of hot-pressed uranium mononitride, BMI-1633, Battelle Memorial Inst., Columbus, OH, 1963.

[16] K.M. Taylor, C.H. McMurtry, Synthesis and Fabrication of Refractory Uranium Compounds. Summary Report for May 1959 through December 1960, ORO-400, Carborundum Co. Research and Development Div., Niagara Falls, NY, 1961.

[17] M. Guinan, C.F. Cline, Elastic properties of uranium mononitride at 298 K, Journal of Nuclear Materials 43(2) (1972) 205-206.

[18] J. Adachi, K. Kurosaki, M. Uno, S. Yamanaka, M. Takano, M. Akabori, K. Minato, Mechanical properties at sub-microscale and macroscale of polycrystalline uranium mononitride, Journal of Nuclear Materials 384(1) (2009) 6-11.

[19] M.A. DeCrescente, M.S. Freed, S.D. Caplow, Uranium nitride fuel development, SNAP-50, PWAC-481, Pratt and Whitney Aircraft, Middletown, CT, Connecticut Advanced Nuclear Engineering Lab., 1965.

[20] S.L. Hayes, J.K. Thomas, K.L. Peddicord, Material property correlations for uranium mononitride: II. Mechanical properties, Journal of Nuclear Materials 171(2-3) (1990) 271-288.

[21] F.L. Carlsen, O.L. Harms, Thermal Expansion of UN, ORNL-3670, Oak Ridge National Lab., Oak Ridge, TN, 1964, pp. 143-144.

[22] V. Kocevski, D.A. Rehn, A.J. Terricabras, A. van Veelen, M.W. Cooper, S.W. Paisner, S.C. Vogel, J.T. White, D.A. Andersson, Finite Temperature Properties of Uranium Mononitride, Journal of Nuclear Materials 576(1) (2023) 154241.

[23] M.H. Fassler, F.J. Huegel, M.A. DeCrescente, Compressive Creep of UC AND UN, PWAC-482: Part I, Pratt and Whitney Aircraft, Middletown, CT, Connecticut Advanced Nuclear Engineering Lab., 1965.

[24] R. Vandervoort, W. Barmore, C. Cline, Compressive Creep of Polycrystalline Uranium Mononitride in Nitrogen, Metallurgical Society of AIME 242 (1968) 1466-1467.

[25] U. Masaaki, I. Michio, Compressive Creep of Sintered UC-UN Solid Solutions, Journal of Nuclear Materials 49(1) (1973) 91-97.

[26] H. Matzke, Science of advanced LMFBR fuels : solid state physics, chemistry, and technology of carbides, nitrides, and carbonitrides of uranium and plutonium, 1986.

[27] S.L. Hayes, J.K. Thomas, K.L. Peddicord, Material property correlations for uranium mononitride: I. Physical properties, Journal of Nuclear Materials 171(2-3) (1990) 262-270.

[28] J.B. Holt, M.Y. Almassy, Nitrogen Diffusion in Uranium Nitride as Measured by Alpha Particle Activation of 15N, Journal of the American Ceramic Society 52(12) (1969) 631-635.

[29] H.J. Matzke, Point Defects and Transport Properties in Carbides, Solid State Ionics 12 (1984) 24-45.

[30] M.W.D. Cooper, J. Rizk, C. Matthews, V. Kocevski, G.T. Craven, T. Gibson, D.A. Andersson, Simulations of self-and Xe diffusivity in uranium mononitride including chemistry and irradiation effects, Journal of Nuclear Materials 587 (2023) 154685.

[31] G.T. Craven, R. Chen, M.W.D. Cooper, C. Matthews, J. Rizk, W. Malone, L. Johnson, T. Gibson, D.A. Andersson, Data-driven methods for diffusivity prediction in nuclear fuels, Computational Materials Science 230 (2023) 112442.

[32] L. Johnson, W. Malone, J. Rizk, R. Chen, T. Gibson, M.W.D. Cooper, G.T. Craven, Machine learning method to determine concentrations of structural defects in irradiated materials, Computational Materials Science 242 (2024) 113079.

[33] D.K. Reimann, D.M. Kroeger, T.S. Lundy, Citation self-diffusion in UN(1+x), Journal of Nuclear Materials 38(2) (1971) 191-196.

[34] H. Matzke, Atomic mechanisms of mass transport in ceramic nuclear fuel materials, Journal of the Chemical Society, Faraday Transactions 86(8) (1990) 1243-1256.

[35] S.L. Hayes, J.K. Thomas, K.L. Peddicord, Material property correlations for uranium mononitride: III. Transport properties, Journal of Nuclear Materials 171(2-3) (1990) 289-299.

[36] Q. Yin, A. Kutepov, K. Haule, G. Kotliar, S.Y. Savrasov, W.E. Pickett, Electronic correlation and transport properties of nuclear fuel materials, Physical Review B 84(19) (2011) 195111.

[37] K. Kurosaki, K. Yano, K. Yamada, M. Uno, S. Yamanaka, A Molecular Dynamics Study of the Thermal Conductivity of Uranium Mononitride, Journal of Alloys and Compounds 311(2) (2000) 305-310.

[38] B. Szpunar, J.I. Ranasinghe, L. Malakkal, J.A. Szpunar, First principles investigation of thermal transport of uranium mononitride, Journal of Physics and Chemistry of Solids 146 (2020) 109636.

[39] B. Szpunar, J.A. Szpunar, Thermal conductivity of uranium nitride and carbide, International Journal of Nuclear Energy 2014 (2014).

[40] J.H. Harding, D.G. Martin, A recommendation for the thermal conductivity of UO2, Journal of Nuclear Materials 166(3) (1989) 223-226.

[41] T. Kikuchi, T. Takahashi, S. Nasu, Porosity dependence of thermal conductivity of uranium mononitride, Journal of Nuclear Materials 45(4) (1973) 284-292.

[42] Y. Takahashi, M. Murabayashi, Y. Akimoto, T. Mukaibo, Uranium mononitride: heat capacity and thermal conductivity from 298 to 1000 K, Journal of Nuclear Materials 38(3) (1971) 303-308.

[43] J.P. Moore, W. Fulkerson, D.L. McElroy, Thermal Conductivity, Electrical Resistivity, and Seebeck Coefficient of Uranium Mononitride, Journal of the American Ceramic Society 53(2) (1970) 76-82.

[44] T.G. Kollie, J.P. Moore, Electrical Resistivity and Thermal Conductivity of Uranium Mononitride, ORNL-3670, Oak Ridge National Lab., Oak Ridge, TN, pp. 142-143.

[45] B.A. Hayes, M.A. DeCrescente, Thermal Conductivity and Electrical Resistivity of Uranium Mononitride, PWAC-481, Pratt and Whitney Aircraft, Middletown, CT, Connecticut Advanced Nuclear Engineering Lab., 1965.

[46] R.W. Endebrock, E. Foster Jr, D.L. Keller, Preparation and Properties of Cast UN, BMI-1690, Battelle Memorial Inst., Columbus, OH, 1964.

[47] K.L. Peddicord, M.E. Cunningham, A. Tripathi, Porosity correction to thermal conductivity based on analytical temperature solutions, Transactions of the American Nuclear Society, 1978, pp. 548-549.

[48] S.B. Ross, M.S. El-Genk, R.B. Matthews, Thermal conductivity correlation for uranium nitride fuel between 10 and 1923 K, Journal of Nuclear Materials 151(3) (1988) 318-326.

[49] F.L. Oetting, J.M. Leitnaker, The chemical thermodynamic properties of nuclear materials I. Uranium mononitride, The Journal of Chemical Thermodynamics 4(2) (1972) 199-211.

[50] C. Affortit, Chaleur specifique de UC et UN, Journal of Nuclear Materials 34(1) (1970) 105-107.

[51] J.F. Counsell, R.M. Dell, J.F. Martin, Thermodynamic properties of uranium compounds. Part 2.—Low-temperature heat capacity and entropy of three uranium nitrides, Transactions of the Faraday Society 62 (1966) 1736-1747.

[52] E.F. Westrum Jr., C.M. Barber, Uranium mononitride: Heat capacity and thermodynamic properties from 5 to 350 K, The Journal of Chemical Physics 45(2) (1966) 635-639.

[53] L.C. Harrington, Heat Capacity and Enthalpy of Uranium Mononitride from 0 to 1200C (32 to 2200F), CNLM-4461, Pratt and Whitney Aircraft, Middletown, CT, Connecticut Advanced Nuclear Engineering Lab., 1963.

[54] E.H.P. Cordfunke, R.P. Muis, The heat capacity of uranium mononitride, Journal of Nuclear Materials 42(2) (1972) 233-234.

[55] S.L. Hayes, J.K. Thomas, K.L. Peddicord, Material property correlations for uranium mononitride: IV. Thermodynamic properties, Journal of Nuclear Materials 171(2-3) (1990) 300-318.

[56] K.J. Bowles, R.E. Gluyas, Evaluation of refractory-metal-clad uranium nitride and uranium dioxide fuel pins after irradiation for times up to 10 450 hours at 990 C, NASA-TN-D-7891, NASA Lewis Research Center, Cleveland, OH, 1975.

[57] R. Matthews, K. Chidester, C. Hoth, R. Mason, R. Petty, Fabrication and Testing of Uranium Nitride Fuel for Space Power Reactors, Journal of Nuclear Materials 151(3) (1988) 334-344.

[58] S.I. Porollo, S.N. Ivanov, Corrosion Damage and Mechanical Properties of BR-10 Reactor Fuel-Rod Cladding with Mononitride Uranium Fuel, Atomic Energy 125 (2019) 185-193.

[59] S.I. Porollo, S.N. Ivanov, E.E. Marinenko, L.M. Zabudko, Analysis of experimental data on gas release and swelling of UN fuel irradiated in BR-10 reactor, International Conference on Fast Reactors and Related Fuel Cycles: Next Generation Nuclear Systems for Sustainable Development (FR17) Programme and Papers, International Atomic Energy Agency (IAEA) 2017.

[60] J.G. Slaby, B.L. Siegel, Examination of T-111 clad uranium nitride fuel pins irradiated up to 13,000 hours at a clad temperature of 990 C, NASA-TM-X-2950, NASA Lewis Research Center Cleveland, OH, 1973.

[61] J.G. Slaby, B.L. Siegel, L. Gedeon, R.J. Galbo, Irradiation of three t-111 clad uranium nitride fuel pins for 8070 hours at 990 C (1815 F), NASA-TM-X-2878, NASA Lewis Research Center Cleveland, OH, 1973.

[62] K.R. Thoms, Design, fabrication, and operation of capsules for the irradiation testing of candidate advanced space reactor fuel pins, ORNL-TM-4825, Oak Ridge National Lab., Oak Ridge, TN, 1975.

[63] S.C. Weaver, J.L. Scott, Comparison of reactor fuels for high temperature applications, ORNL-TM-1360, Oak Ridge National Lab., Oak Ridge, TN, 1965.

[64] S.C. Weaver, J.L. Scott, R.L. Senn, B.H. Montgomery, Effects of irradiation on uranium nitride under space-reactor conditions, ORNL-4461, Oak Ridge National Lab., Oak Ridge, TN, 1969.

[65] G. Rossiter, Understanding and modelling fuel behaviour under irradiation, in: W.P. Limited (Ed.), Nuclear Fuel Cycle Science and Engineering, Woodhead Publishing Limited2012, pp. 396-426.

[66] P. Van Uffelen, M. Suzuki, 3.19: Oxide Fuel Performance Modeling and Simulations, Comprehensive Nuclear Materials 3 (2012) 535-577.

[67] F.J. Huegel, Swelling of Irradiated UC AND UN, PWAC-482: Part II, Pratt and Whitney Aircraft, Middletown, CT, Connecticut Advanced Nuclear Engineering Lab., 1965.

[68] A.J.E. Foreman, Calculations on the Rate of Swelling of Gas Bubbles in Uranium, AERE-T/M-134, Atomic Energy Research Establishment, Harwell, Berks, England, 1956.

[69] D.L. Keller, Progress on LMFBR Cladding, Structural, and Component Materials Studies during July 1970 through June 1971.Annual Report, Task 32. Final Report, Task 14., BMI-1914, Battelle Memorial Inst., Columbus, OH, 1971.

[70] D.L. Keller, Progress on Development of Fuels and Technology for Advanced Reactors During October-December 1970. Progress Report, BMI-1898, Battelle Memorial Inst., Columbus, OH, 1971.

[71] D.L. Keller, W. Chubb, Developments in the Technology of Nuclear Fuels During August 1967 through July 1968. Annual Report, BMI-1848, Battelle Memorial Inst., Columbus, OH, 1968.

[72] R.G. Rohal, T.N. Tambling, Unrestrained swelling of uranium-nitride fuel irradiated at temperatures ranging from 1100 to 1400 K (1980 to 2520 R), NASA-TM-X-2907, NASA Lewis Research Center Cleveland, OH, 1973.

[73] E.D. Albrecht, A.J. Rothman, J.D. Lee, J.M. Johnson, W.N. Hayes Jr., High-Temperature Irradiation and Post-Irradiation Analysis of Uranium Nitride Fuel, California Univ., Livermore, CA, Lawrence Radiation Lab., 1969.

[74] E.D. Albrecht, A.J. Rothman, J.D. Lee, J.M. Johnson, W.N. Hayes Jr., Irradiation studies of uranium nitride, California Univ., Livermore, CA. Lawrence Radiation Lab., 1969.

[75] S.B. Ross, M.S. El-Genk, R.B. Matthews, Uranium nitride fuel swelling correlation, Journal of Nuclear Materials 170(2) (1990) 169-177.

[76] L. Zabudko, V. Poplavsky, Investigations of Nitride Fuels for Fast Reactors in Russia, Symposium on Nitride Fuel Cycle Technology, Japan Atomic Energy Research Inst., Tokai, Japan, 2004, pp. 1-14.

[77] S.S. Voss, SNAP (Space Nuclear Auxiliary Power) Reactor Overview, AFWL-TN-84-14, Air Force Weapons Lab, Kirtland AFB, NM, 1984.

[78] H. Banach, H. Richings, Status of the SNAP-50 reactor fuels parametric studies. Part I, PWAC-431, Pratt and Whitney Aircraft, Middletown, CT, Connecticut Advanced Nuclear Engineering Lab., 1964.

[79] W. Doll, SNAP-50/SPUR program annual technical report, 1964, CNLM-6086, Pratt and Whitney Aircraft, Middletown, CT, Connecticut Advanced Nuclear Engineering Lab., 1964.

[80] L. Raring, Fuels and materials highlights: SNAP-50 and advanced programs, CNLM-6155, Pratt and Whitney Aircraft, Middletown, CT, Connecticut Advanced Nuclear Engineering Lab., 1965.

[81] W. Heneveld, R. Paschall, T. Springer, V. Swanson, A. Thiele, R. Tuttle, Experimental physics characteristics of a heavy-metal-reflected fast-spectrum critical assembly, NASA-CR-72820, Atomics International Div. North American Rockwell Corp., Canoga Park, CA, 1971.

[82] M.H. Krasner, H.W. Davison, A.J. Diaguila, Conceptual design of a compact fast reactor for space power, NASA TM X-67859, NASA Lewis Research Center Cleveland, OH, 1971.

[83] W. Mayo, P.G. Klann, C.L. Whitmarsh Jr., Nuclear design and experiments for a space power reactor, NASA TM X-67857, NASA Lewis Research Center Cleveland, OH, 1971.

[84] R.R. Metroka, Fabrication of uranium mononitride compacts, NASA TN D-5876, NASA Lewis Research Center Cleveland, OH, 1970.

[85] R.E. Gluyas, G.K. Watson, Materials technology for an advanced space power nuclear reactor concept: Program summary, NASA-TN-D-7909, NASA Lewis Research Center, Cleveland, OH, 1975.

[86] R.E. Gluyas, A.F. Lietzke, Materials technology program for a compact fast reactor for space power, NASA-TM-X-67869, NASA Lewis Research Center, Cleveland, OH, 1971.

[87] R.G. Rohal, T.N. Tambling, R.L. Smith, Testing of uranium nitride fuel in T-111 cladding at 1200 K cladding temperature, NASA-TM-X-2732, NASA Lewis Research Center Cleveland, OH, 1973.

[88] D.S. Dutt, C.M. Cox, R.A. Karnesky, M.K. Millhollen, Performance testing of refractory alloy-clad fuel elements for space reactors, Hanford Engineering Development Lab., Richland, WA, 1985.

[89] S.F. Demuth, SP100 space reactor design, Progress in Nuclear Energy 42(3) (2003) 323-359.

[90] W.F. Lyon III, Thermal analysis of the FSP-1 fuel pin irradiation test, AIP Conference Proceedings, American Institute of Physics, 1991, pp. 892-901.

[91] B.J. Makenas, D.M. Paxton, S. Vaidyanathan, M. Marietta, C.W. Hoth, SP-100 Fuel Pin Performance: Results from Irradiation Testing, AIP Conference Proceedings, American Institute of Physics, 1994, pp. 403-412.

[92] B.J. Makenas, J.W. Hales, A.L. Ward, Fuels irradiation testing for the SP-100 program, AIP Conference Proceedings, American Institute of Physics, 1991, pp. 886-891.

[93] R.A. Karnesky, R.E. Mason, Postirradiation examination results from SP-1, HEDL-SA-3391, Hanford Engineering Development Lab., Richland, WA, 1986.